7

Integrated Vehicle Dynamics Control: Centralized Control Architecture

7.1 Principles of Integrated Vehicle Dynamics Control

Current and future motor vehicles are incorporating increasingly sophisticated chassis control systems to improve vehicle handling, stability, and comfort. These chassis control systems include vehicle stability control (VSC), active suspension system (ASS), electrical power steering (EPS), and active four-wheel steering control (4WS), etc. These control systems are generally designed by different suppliers with different technologies and components to accomplish certain control objectives or functionalities. Especially when equipped into vehicles, control systems often operate independently and thus result in a parallel vehicle control architecture. In such a parallel vehicle control architecture, inevitably there occur interaction and performance conflict among the control systems occur ineviably because the vehicle motions in the vertical, lateral, and longitudinal directions are coupled together in nature. To address the problem, an approach of using an integrated vehicle control system was proposed around the 1990s[1]. An integrated vehicle control system is an advanced system that coordinates all the chassis control systems and components to improve the overall vehicle performance including handling stability, ride comfort, and safety, through creating synergies in the use of sensor information, hardware, and control strategies of different control systems[1,2]. As a result, the application of integrated vehicle control systems brings a number of advantages, including: (1) coordinating the interactions among the different subsystems; (2) further exploiting the potentials of each subsystem through integrating the function of the different subsystems with different work domains; (3) reducing the number of sensors and actuators by sharing and integrating the related ones. As shown in Figure 7.1, a better pareto-optimal solution of the vehicle overall performance is achieved through creating synergies amongst the different subsystems.
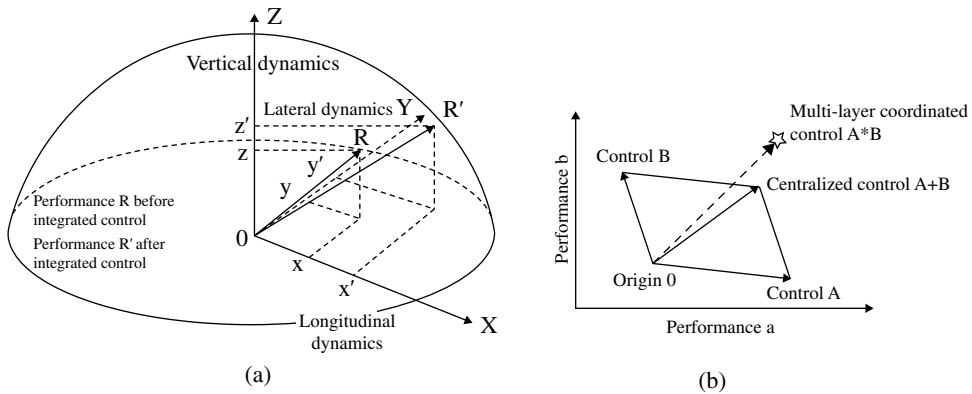
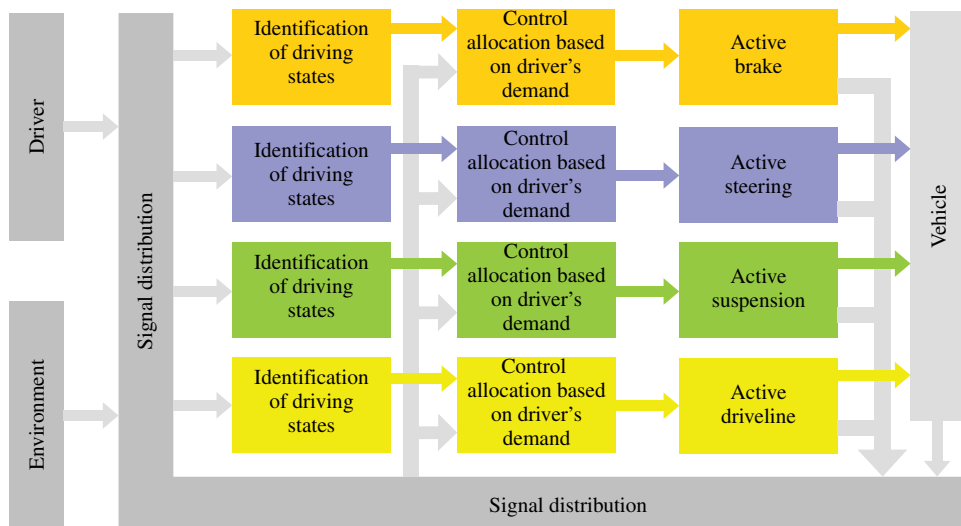**Figure 7.1**   Principle of an integrated vehicle control system.

Figure 7.2   Decentralized (or Parallel) architecture.

A number of control techniques have been designed to achieve the goal of functional integration of the chassis control systems. These control techniques can be classified into three categories according to the extent of function integration of the subsystems, as suggested by Gordon et al.[2] and Yu et al.[3]: (1) decentralized or parallel control; (2) centralized control; and (3) multilayer control. In the decentralized control architecture shown in Figure 7.2, the subsystems of the vehicle are relatively independent and communicate with each other through the onboard network (CAN or LIN) to achieve their local control targets conveniently and flexibly. However, due to the lack of a global control target for the decentralized control architecture, the control architecture can only serve as a combined control structure of the vehicle subsystems at most. Compared to the parallel structure with
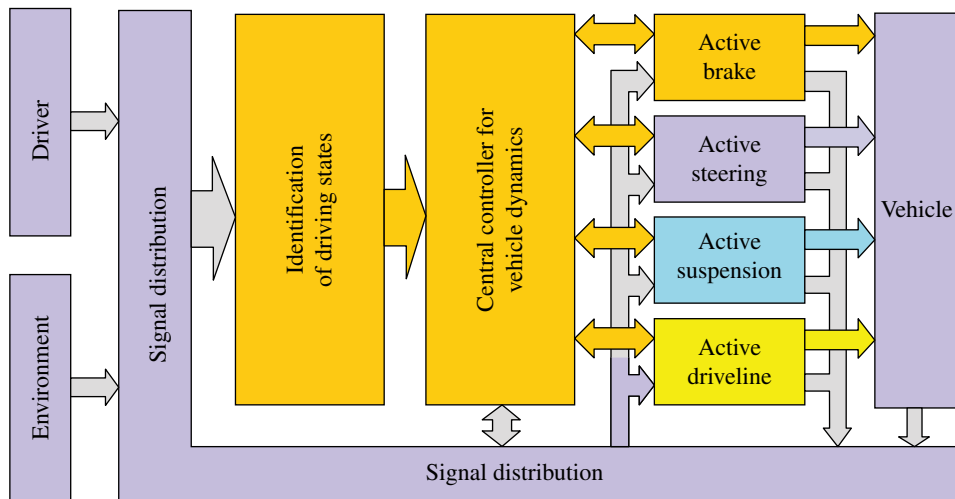
Figure 7.3   Centralized architecture.

standalone subsystems, the decentralized control architecture is superior through taking advantage of integrating and sharing the information of sensors and actuators.

Most of the control techniques used in the previous studies in recent years fall into the second category. Examples include nonlinear predictive control[4], random sub-optimal control[5], robust $H_∘$ [6], sliding mode[7], and artificial neural networks[8]. In the centralized architecture shown in Figure 7.3, a single central controller collects all the vehicle operation information, including information from the sensors and the state estimators, and then generates control commands to the subsystem actuators by applying a global multi-objective optimization algorithm. Therefore, both the advantages and disadvantages are obvious. The centralized architecture has the advantages of controlling and observing all the subsystems in an integrated manner. However, the disadvantages cannot be ignored: the curse of dimensionality caused by the increasing number of subsystems results in tremendous design difficulties. Moreover, the failure of the centralized controller inevitably leads to a total failure of the whole chassis control system. Finally, when the centralized architecture needs to include more required subsystems, the entire centralized architecture has to be redesigned since the architecture lacks flexibility.

In contrast, multilayer control has not yet been applied extensively to integrated vehicle control. It is indicated by a relatively small volume of research publications [2,9–14]. The multilayer control architecture shown in Figure 7.4 consists of two layers. The upper layer controller monitors the driver's intentions and the current vehicle state. Based on these input signals, the upper layer controller is designed to coordinate the interactions amongst all the subsystem controllers in order to achieve the desired vehicle state. Thereafter, the control commands are generated by the upper layer controller and distributed to the corresponding individual lower layer controllers. Finally, the individual lower layer controllers execute respectively their local control objectives to control the vehicle dynamics.
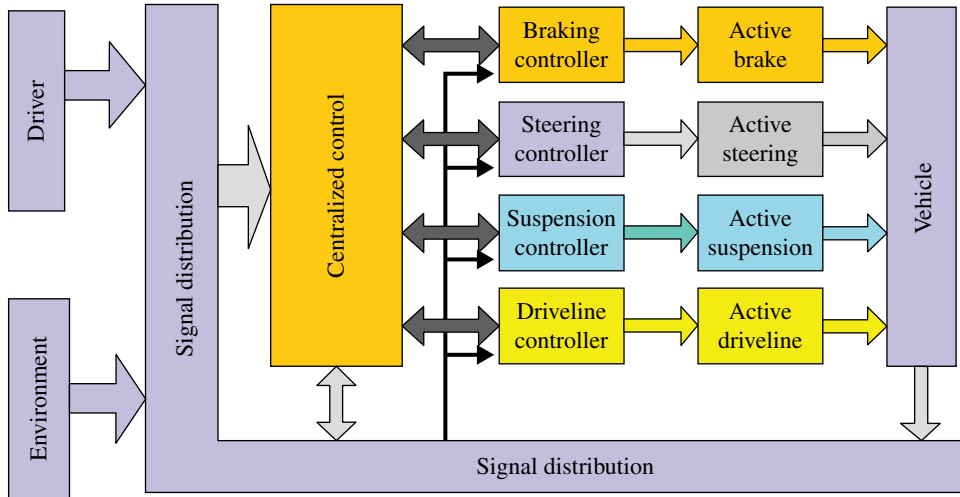
Figure 7.4 Multilayer control architecture.

In this chapter, the applications of the centralized control architecture are introduced by using various control methods to fulfill the integrated control goal for different subsystems.

7.2   Integrated Control of Vehicle Stability Control Systems (VSC)

A vehicle stability control system (VSC) is an integrated control system through the function integration of the anti-lock brake system (ABS) and traction control system (TCS) with the active yaw moment control system (AYC). VSC maintains the lateral stability of the vehicle by controlling the longitudinal forces between the tyres and road. As discussed in Section 3.5, the widely-used direct yaw moment control (DYC) method was briefly introduced to achieve the aims of the VSC. To fully explore the work principles of VSC, a control strategy for the sideslip angle of the vehicle center of gravity (CG) is proposed by using dynamic limits of the road surfaces in order to examine the effects on the sideslip angle for different road surfaces. Furthermore, a method for estimating the road adhesion coefficient is proposed by applying both the extended Kalman filter and neural network since estimation of the road adhesion coefficient is an important topic in the area of VSC and is also the basis of designing the control strategy of a VSC[15].

7.2.1   Sideslip Angle Control

As mentioned in Section 3.5 above, the two crucial states to determine the vehicle stability include the yaw rate and sideslip angle. The yaw rate measures the vehicle angular velocity around its vertical inertia axis, and the sideslip angle reflects the deviation

of the vehicle on its current driving direction. Therefore, both states must be taken as control targets when designing the VSC.

Moreover, the effects of the sideslip angle resulting from different road surfaces must be taken into consideration. There are two main reasons. First, the stability limit that the vehicle is able to achieve is different for different road surfaces. For example, the stability limit for the road surface with a higher adhesion coefficient is larger than that with a lower adhesion coefficient. Second, the control of the sideslip angle is fulfilled through adjusting the longitudinal forces between the tyres and the road, and the longitudinal forces are directly related to the adhesion coefficient. Therefore, the control strategy for the sideslip angle is proposed by using dynamic limits of road surfaces in order to examine the effects on the sideslip angle for different road surfaces.

7.2.1.1   Development of the Sideslip Angle Control Strategy

7.2.1.1.1   *Dynamic Characteristics of the Sideslip Angle*
We first investigate the dynamic characteristics of the sideslip angle through performing a simulation study of a 7-DOF vehicle dynamic model. The vehicle is assumed to drive on a road with the adhesion coefficient of 0.3, and the double lane change maneuver is performed. The relationship between the sideslip angle and the sideslip angular velocity is shown in Figure 7.5. In the figure, when the absolute value of the sideslip angle is less than 0.02 rad, the vehicle stays stable; when it is larger than 0.02 rad, the absolute value of the rate of the sideslip angle increases drastically. This phenomenon shows that the vehicle tends to become unstable. Since vehicle stability is directly related to the sideslip motion of the vehicle, this motion must be bounded in order to keep the vehicle stable. Thus, the aim of the sideslip angle controller is to bind the sideslip angle within a suitable region in
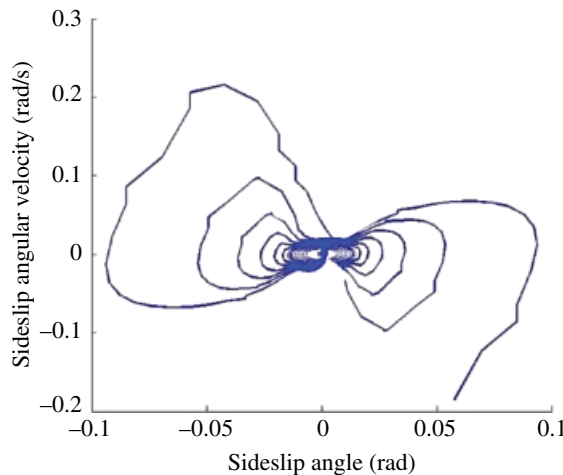

Figure 7.5   Simulation results for the relationship between the sideslip angle and sideslip angular velocity.
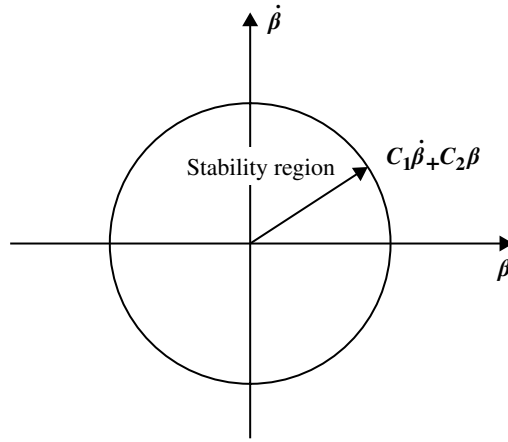
Figure 7.6   Stability region in the phase plane of the sideslip motion.
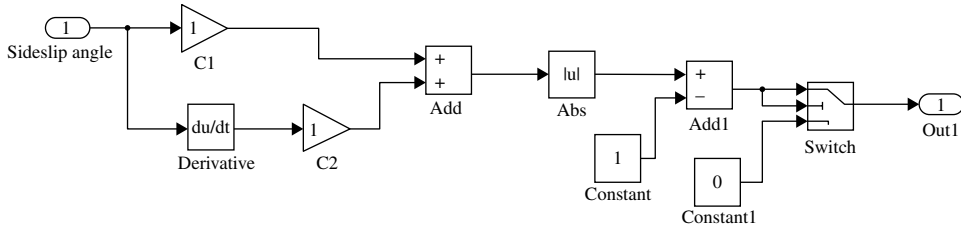

Figure 7.7   Block diagram of the proposed sideslip angle controller.

which the vehicle stays stable. As shown in Figure 7.6, the suitable stability region is defined in the phase plane of the sideslip motion:

$$\left| C_1 \dot{\beta} + C_2 \beta \right| < 1 \tag{7.1}$$

The suitable stability region is achieved by selecting suitable values of the parameters C_1 and C_2. Thus, the sideslip angle controller is proposed in Figure 7.7.

To demonstrate the effectiveness of the proposed sideslip angle controller, simulation investigations are performed for different driving conditions. First, the driving condition is set as follows: the vehicle is assumed to drive at a constant speed of 120 km/h on a road with a high adhesion coefficient of 0.9, and a double lane change maneuver is performed. As shown in Figures 7.8 and 7.9, the simulation results demonstrate that the sideslip angle is bounded at a relatively small value, and the sideslip motion is stable. In addition, the other driving condition is also performed: in this case, the vehicle speed is set to 60 km/h on a road with a low adhesion coefficient of 0.4, and the double lane change maneuver is also performed. As shown in Figures 7.10 and 7.11, the simulation results demonstrate that the VSC is able to restrain the sideslip at a relatively small value, and hence the sideslip motion stays stable.
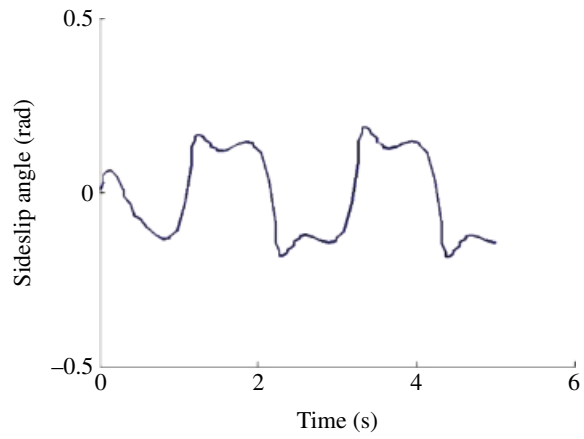
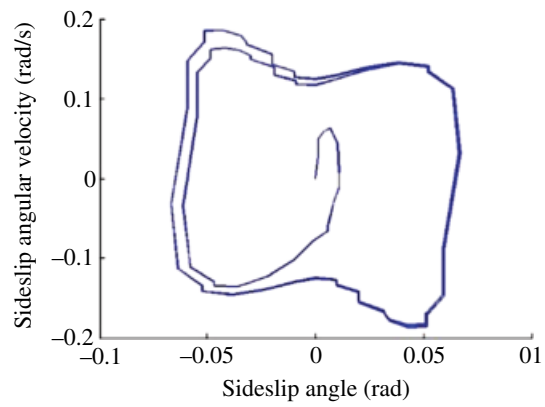**Figure 7.8**   Response of the sideslip angle.

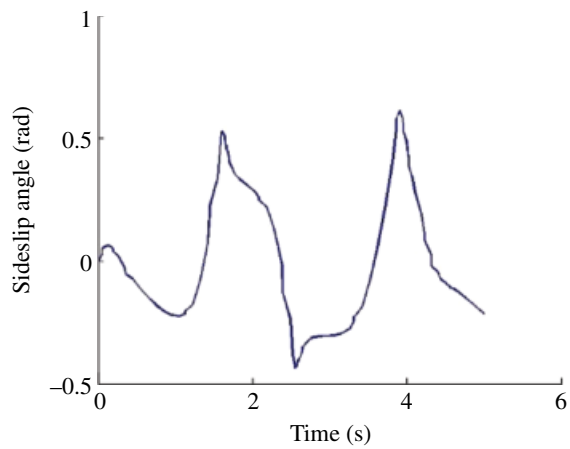**Figure 7.9**   Phase plane of the sideslip motion.

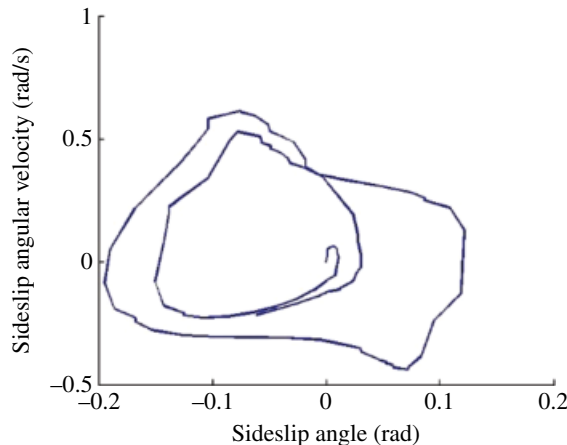**Figure 7.10**   Response of the sideslip angle.

Figure 7.11   Phase plane of the sideslip motion.

However, as shown in Figure 7.10, the peak value of the sideslip angle is quite large and the phenomenon contradicts reality since the vehicle cannot stay stable with such a large sideslip angle. The simulation results show that it is inappropriate to define directly the handling limit as the control objectives since the lateral tyre force has already been close or even beyond the saturation point when the vehicle approaches the handling limit.

Therefore, an effective control method must determine the control objectives to generate the corrective yaw moment to pull the vehicle back to the stable region before it approaches the handling limit. The definitions of the reference region and the control region for designing the sideslip angle controller are illustrated in Figure 7.12. There are two boundaries, the inner boundary and outer boundary, which define the reference region and the control region, respectively. When the vehicle state lies inside the reference region, the vehicle is considered to be stable and no control action is required. When the vehicle state reaches the control region, which is bounded by the inner boundary and the outer boundary, the VSC is actuated and thus the corrective yaw moment is generated by the sideslip angle controller to pull the vehicle back into the reference region.

As discussed earlier in Section 7.2.1, the effects of the sideslip angle resulting from different road surfaces must be taken into consideration. Thus the determination of the above-mentioned two boundaries must also consider the effects of the road adhesion coefficients. As shown in Figure 7.13, the outer boundary is defined as a specific value of the sideslip angle when the lateral tyre force reaches the saturation point, while the inner boundary is defined as a specific value of the sideslip angle when the lateral tyre force reaches the linear limit.

7.2.1.1.2   *Outer Boundary of the Sideslip Angle*
To determine the outer boundary of the sideslip angle, a dynamic boundary is constructed by considering the effects of the road adhesion coefficients. The lateral acceleration of the C.G. is given as:

$$a_y = v_x \dot{r} + \dot{v}_y \tag{7.2}$$

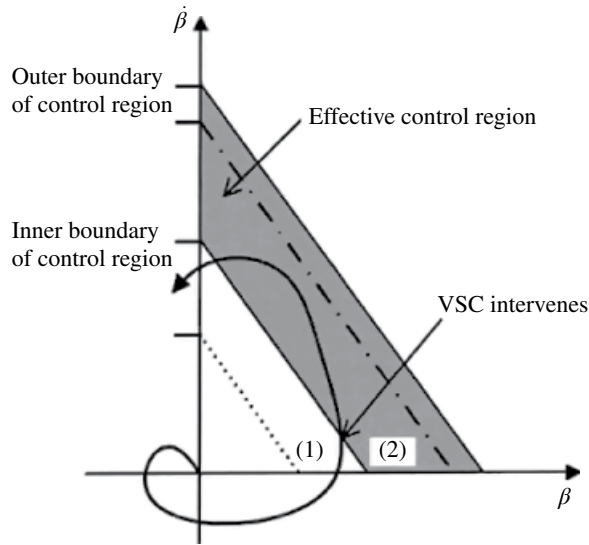**Figure 7.12**   Definition of the reference region and control region.
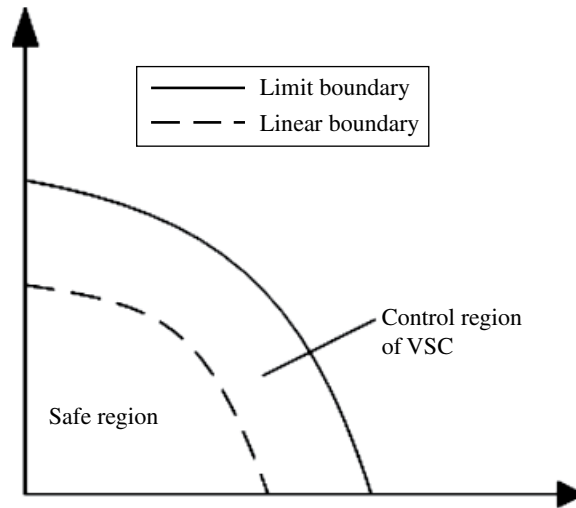

Figure 7.13   Definition of the two boundaries for designing the sideslip angle controller.

Considering the sideslip angle as relatively small, we have $v_y = v_x \tan \beta$. Therefore, the above equation can be rewritten as:

$$a_y = v_x \dot{r} + \dot{v}_x \tan \beta + \frac{v_x \dot{\beta}}{\sqrt{1 + \tan^2 \beta}} \qquad (7.3)$$

Since $a_y \leq \mu g$, and the latter two terms in equation (7.3) are relatively small compared to the first term, the upper limit of the yaw rate r is selected as:

$$r_{max} = 0.85 \mu g / v_x \qquad (7.4)$$

Accordingly, the upper limit of the sideslip angle is chosen as:

$$\beta_{max} = \arctan\left(0.02 \mu g\right) \qquad (7.5)$$

According to the above equation, when the road adhesion coefficient $\mu = 0.9$, the sideslip angle equals to 0.17 rad; when $\mu = 0.3$, the value is 0.08 rad. The above equation can be adjusted according to different vehicle physical parameters.

7.2.1.1.3   Inner Boundary of the Sideslip Angle
When the vehicle state lies inside the linear region, the yaw rate r is derived from the 2-DOF linear vehicle dynamic model:

$$r = \frac{v_x / L}{1 + K v_x^2} \delta_f \qquad (7.6)$$

where $K = \dfrac{m}{L^2}\left(\dfrac{a}{k_r} - \dfrac{b}{k_f}\right)$. When $K = 0$, the above equation is given as follows:

$$r = v_x \delta_f / L \qquad (7.7)$$

The above equation shows that the steady state gain of the yaw rate is linear with the steering angle of the front wheel when the vehicle lies inside the linear region. Therefore, it is possible to determine whether the vehicle lies inside the linear region by examining whether the above linear relationship exists. A simulation study is performed to demonstrate the relationship of the two variables. As shown in Figures 7.14 and 7.15, the simulation results illustrate that the yaw rate r is linear with the steering angle of the front wheel δ_f when δ_f is smaller than 0.05 rad. However, with the increase on the steering angle δ_f, the relationship tends to be nonlinear.

As a matter of fact, only an approximately linear relationship exists for the yaw rate r and the steering angle of the front wheel δ_f since most vehicles have understeer characteristics. The relationships for the cases of understeer and neutral steer are illustrated in Figure 7.16. Therefore, a weighting function is constructed as follows to compensate for the nonlinear relationship

$$k = \begin{cases} 1 & v_x < 9m/s \\ c \cdot e^{v_x/7} & v_x \geq 9m/s \end{cases} \qquad (7.8)$$

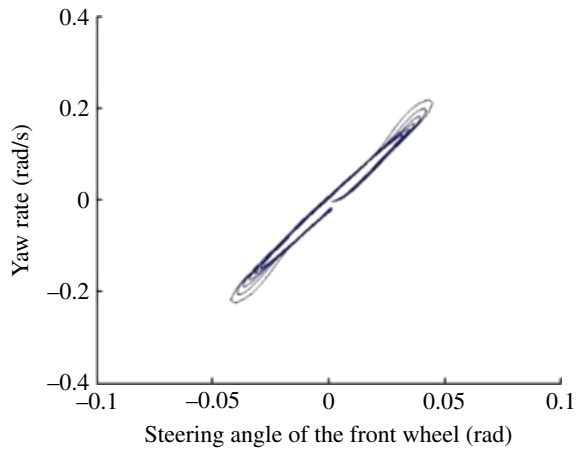The weighting function is illustrated in Figure 7.17.

Figure 7.14 Relationship between the steady state gain of the yaw rate and the steering angle of the front wheel.
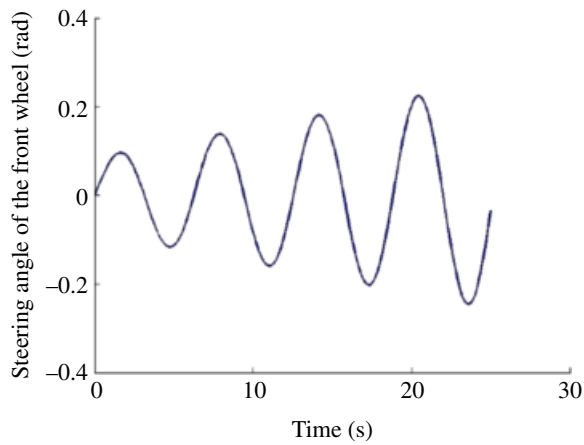

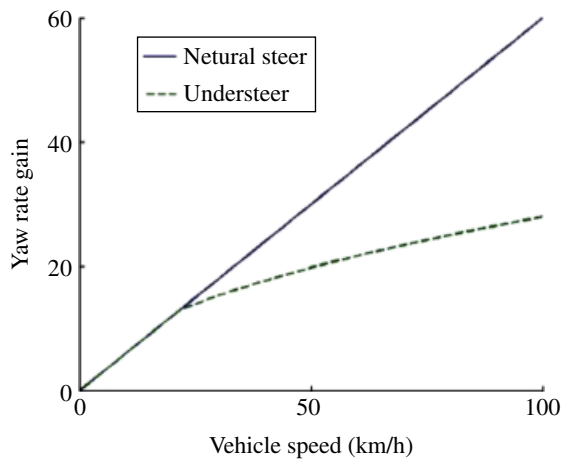**Figure 7.15** Steering angle of the front wheel.

Figure 7.16 Relationships between r and δ_f for the cases of understeer and neutral steer.
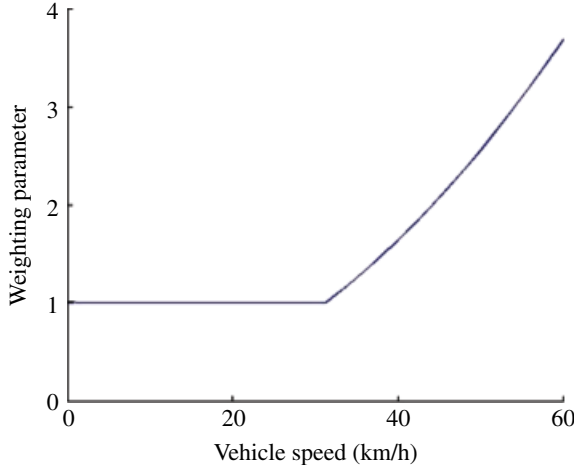
Figure 7.17   Weighting parameter for the yaw rate.

7.2.1.2   Sideslip Angle Controller Design

The nonlinear sliding mode control method is applied to the design of the sideslip angle controller since the controller is actuated mainly in the nonlinear region[16]. The state space equation of the 2-DOF vehicle dynamic model is derived as follows, with the assumptions of a constant forward speed and a small sideslip angle:

$$\dot{x} = Ax + Bu + E\delta_f \tag{7.9}$$

where

$$A = \begin{pmatrix} -\left(k_f + k_r\right)/mv_x^2 & \left(k_f l_f + k_r l_r\right)/mv_x^2 - 1 \\ \left(k_r l_r - k_f l_f\right)/I_z v_x & -\left(k_f l_f^2 + k_r l_r^2\right)/I_z v_x \end{pmatrix}, \; E = \begin{bmatrix} k_f/mv_x & k_f l_f/I_z \end{bmatrix}^T, \; x = \begin{bmatrix} \beta & r \end{bmatrix}^T,$$

$$u = \begin{bmatrix} \Delta M \end{bmatrix}, B = \begin{bmatrix} 0 & 1 \end{bmatrix}^T.$$

A system with the same order is selected as the ideal model:

$$\begin{cases} \dot{x}_m = A_m x_m + B_m r_m \\ y = C_m x_m \end{cases} \tag{7.10}$$

where ΔM is the corrective yaw moment generated by the controller; $x_m \in R^n$ is the state of the ideal model; $r_m \in R^n$ is the input for the bounded model; $y_m \in R^n$ is the output of the model; (A, B) and (A_m, B_m) is controllable, respectively; and (A_m, C_m) is observable. Let the sliding hyper plane be:

$$\sigma = Sx_m \tag{7.11}$$

Decomposing the input matrix B as:

$$B = \begin{bmatrix} B_1 \\ B_2 \end{bmatrix} \tag{7.12}$$

and det $B_2 \uparrow 0$, we obtain:

$$x_m = Tx \tag{7.13}$$

where $T = \begin{bmatrix} I_{n-m} & -B_1 B_2^{-1} \\ 0 & I_m \end{bmatrix}$, and det $T \uparrow 0$. Thus,

$$x = T^{-1} \begin{bmatrix} x_{m1} \\ x_{m2} \end{bmatrix} \tag{7.14}$$

where $x_{m1} \in R^{n-m}$ and $x_{m2} \in R^m$. Substituting equation (7.13) into equations (7.10) and (7.11), we have:

$$\begin{cases} \dot{x} = T^{-1}ATx + T^{-1}Bu \\ \sigma = STx \end{cases} \tag{7.15}$$

where,

$$T^{-1}AT = \begin{bmatrix} A_{11} & A_{12} \\ A_{21} & A_{22} \end{bmatrix}, T^{-1}B = \begin{bmatrix} 0 \\ B_2 \end{bmatrix}, ST = \begin{bmatrix} S_1 & S_2 \end{bmatrix}$$

The expression for the canonical system is derived as:

$$\begin{cases} \dot{x}_1 = A_{11}x_1 + A_{12}x_2 \\ \dot{x}_2 = A_{21}x_1 + A_{22}x_2 + B_2u \\ \sigma = S_1x_1 + S_2x_2 \end{cases} \tag{7.16}$$

Through the following transformation of coordinates:

$$\begin{bmatrix} x_1 \\ x_2 \end{bmatrix} = \begin{bmatrix} x_1 \\ \sigma \end{bmatrix}$$

i.e.

$$\begin{cases} x_1 = x_1 \\ x_2 = S_2^{-1}\sigma - S_2^{-1}S_1x \end{cases} \tag{7.17}$$

Equation (7.16) becomes:

$$\begin{cases} \dot{x}_1 = \left(A_{11} - A_{12} S_2^{-1} S_1 \right) x_1 A_{12} S_2^{-1} \sigma \\ \dot{\sigma} = \left[\left(S_1 A_{11} + S_2 A_{21} \right) - \left(S_1 A_{12} + S_2 A_{22} \right) S_2^{-1} S_1 \right] x_1 \\ \qquad + \left(S_1 A_{12} + S_2 A_{22} \right) S_2^{-1} \sigma + S_2 B_2 u \end{cases} \qquad (7.18)$$

When the system reaches the switch plane, we obtain:

$$\begin{cases} \sigma = S_1 x_1 + S_2 x_2 = 0 \\ \dot{\sigma} = S_1 \dot{x}_1 + S_2 \dot{x}_2 = 0 \end{cases} \qquad (7.19)$$

Substituting equation (7.19) into equation (7.18),

$$\dot{x}_1 = \left(A_{11} - A_{12} K \right) x_1 \qquad (7.20)$$

where $K = S_2^{-1} S_1$, and K can be determined by pole assignment. And hence, the hyper plane matrix of the system is expressed as:

$$S = \begin{bmatrix} S_1 & S_2 \end{bmatrix} = \begin{bmatrix} S_2 K & S_2 \end{bmatrix} = S_2 \begin{bmatrix} K & I_m \end{bmatrix} \qquad (7.21)$$

Assuming $C_m = C$, the state error and its derivative are defined as:

$$e = x_m - x \qquad (7.22)$$

$$\dot{e} = A_m e + \left(A_m - A \right) x + B_m r_m - B u \qquad (7.23)$$

The sliding mode function for the error space is defined as:

$$\sigma_e = S e \qquad (7.24)$$

Its derivative is given as:

$$\dot{\sigma}_e = S \dot{e} = S \left[A_m e + \left(A_m - A \right) x + B_m r_m - B u \right] \qquad (7.25)$$

When the matrices S and B are invertible, the equivalent control law is given as:

$$u_{eq} = \left(SB \right)^{-1} S \left[A_m e + \left(A_m - A \right) x + B_m r_m \right] \qquad (7.26)$$

Substituting equation (7.26) into equation (7.23),

$$\dot{e} = \left[I - B \left(SB \right)^{-1} \right] \left[A_m e + \left(A_m - A \right) x + B_m r_m \right] \qquad (7.27)$$

Let $A_m - A = B K_1$, $B_m = B K_2$, and $E \delta = B K_3$. The above system error equation (7.27) can be rewritten as:

$$\dot{e} = \left[I - B \left(SB \right)^{-1} S \right] A_m e \qquad (7.28)$$

And the error equation (7.23) can be expressed as:

$$\dot{e} = A_m e + B\left(K_1 x + K_2 r_m - u - K_3\right) \tag{7.29}$$

Defining the following transformation for the error e,

$$e' = Te \tag{7.30}$$

Let $e = x_m$ and $\sigma_e = \sigma$. Combining equation (7.29) and equation (7.30), the switch hyper plane of the error is given as:

$$\dot{e}' = \left(A'_{m11} - A'_{m12} S_2^{-1} S_1\right) e' \tag{7.31}$$

Defining the control input for the system as

$$u = \Delta M = Kx \tag{7.32}$$

To make the system converge on to the sliding surface, the following condition must be satisfied:

$$\sigma\dot{\sigma} = SxS\left(A - BK\right) = SxSB\left[\left(SB\right)^{-1} SA - K\right] x = SxSB\left(\alpha - K\right)x < 0 \tag{7.33}$$

where $\alpha = (SB)^{-1} SA = [\alpha_1, \alpha_2, \ldots, \alpha_n]$, only considering the continuous term of ΔM, we have:

$$\begin{cases} \Delta M = Kx, K = [k_1, k_2, \ldots, k_n] \\ k_i = \alpha_i + \mu_i \sigma SB x_i \quad \mu_i > 0 \quad (i = 1, 2, \ldots, n) \end{cases} \tag{7.34}$$

Substituting the above equation into equation (7.33), the constraint condition is derived as follows:

$$\sigma\dot{\sigma} = \sigma SB\left(\alpha - K\right)x = -\sum_{i=1}^{n} \mu_i \left[\sigma_i\left(x\right)\right]^2 < 0 \tag{7.35}$$

7.2.1.3 Simulation Study

To demonstrate the effectiveness of the proposed sideslip angle controller, simulation investigations are performed for different driving conditions. First, the driving condition is set as follows: the vehicle is assumed to drive at a constant speed of 60km/h and 120km/h, respectively. The road adhesion coefficient is selected as 0.4 and 0.9, respectively. The double lane change maneuver is performed. For comparison, the commonly-used controller with a static boundary is also applied. The simulation results for the adhesion coefficient of 0.9 and 0.4 are illustrated in Figures 7.18–7.20, and Figures 7.21–7.23, respectively. As shown in Table 7.1, a quantitative analysis of the simulation results is also performed to better demonstrate the simulation results.

It can be observed from the simulation results that the proposed sideslip angle controller is able to bound the sideslip angle at a relatively small value, and hence the lateral stability
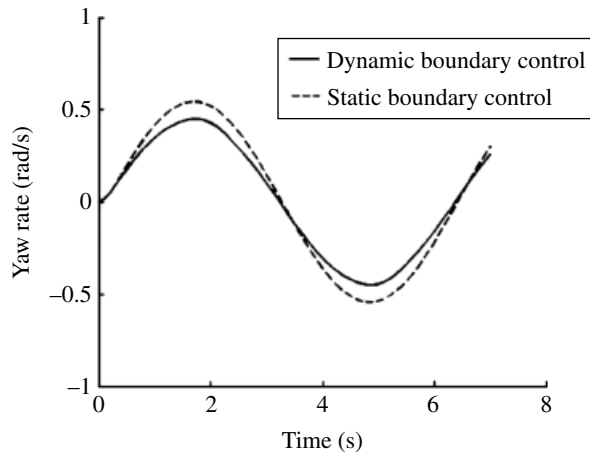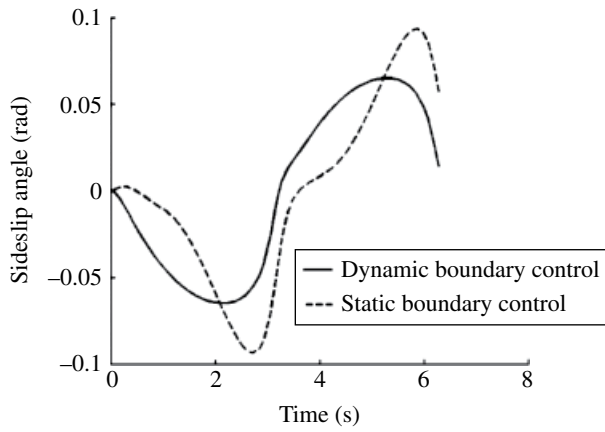
Figure 7.18 Yaw rate.
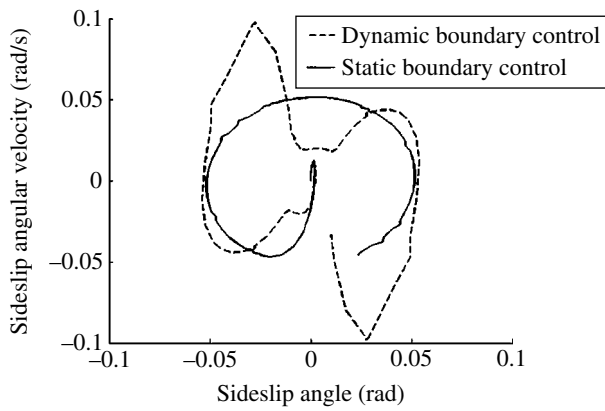

Figure 7.19 Sideslip angle.

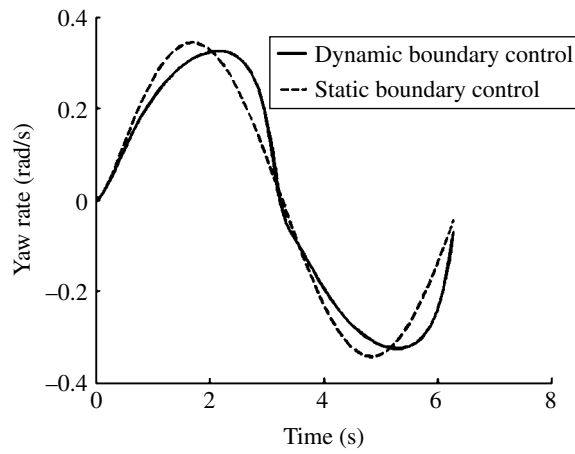**Figure 7.20** Phase plane of the sideslip motion.
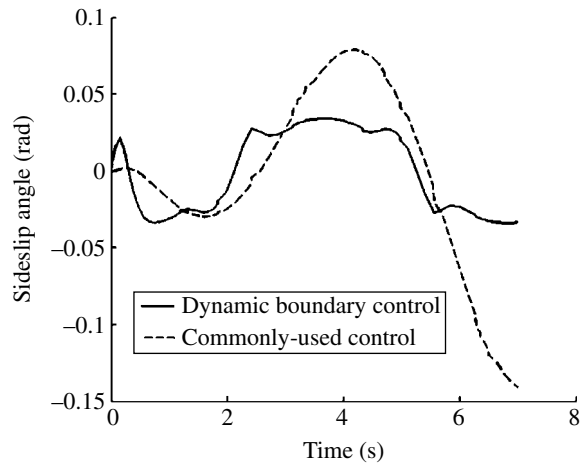
Figure 7.21 Yaw rate.
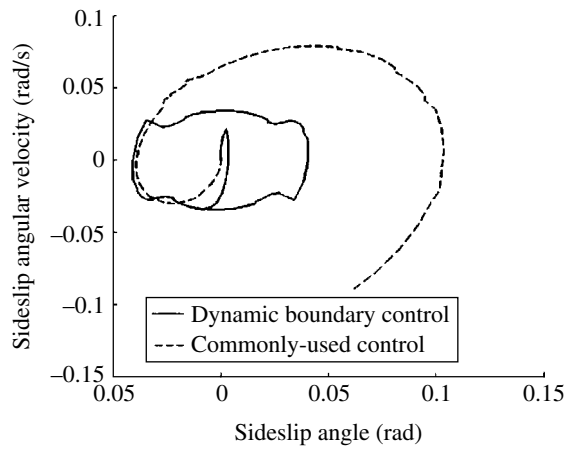

Figure 7.22 Sideslip angle.

Figure 7.23 Phase plane of the sideslip motion.

Table 7.1 Comparison of the simulation results.

Adhesion coefficient	Control objective	Maximum		Improvement
		Controller with static boundary	Controller with dynamic boundary	
0.9	Yaw rate	0.52	0.43	17%
	Sideslip angle	0.095	0.061	36%
0.4	Yaw rate	0.34	0.32	6%
	Sideslip angle	0.079	0.046	42%

of the vehicle is achieved for both the roads with the high adhesion coefficient and low adhesion coefficient. However, the commonly-used controller with the static boundary only performs well on the road with a high adhesion coefficient. As shown in Figure 7.23, the vehicle cannot stay stable on the road with a low adhesion coefficient.

7.2.2   Estimation of the Road Adhesion Coefficient

Estimation of road adhesion coefficient is crucial in developing VSC since it is the basis for implementing the VSC. There are two main reasons: first, an effective control strategy of VSC must consider the effects of the road adhesion coefficients on the stability limits. Second, VSC must be able to precisely adjust the tyre force to execute the control commands. Adjusting the tyre force depends mainly on whether or not the road adhesion coefficient is able to be estimated precisely.

A large number of estimation methods have been developed through the brake driving condition. During the process of braking, the relationship between the road adhesion coefficient and brake efficiency factor is constructed, and thus the road adhesion coefficient is calculated[17, 18]. However, there is no severe braking when the VSC intervenes since the VSC works mainly under the steer driving condition. Therefore, it is necessary to develop methods to estimate the road adhesion coefficient for the VSC under the steer driving condition. As discussed earlier, with the increase of the sideslip angle, the lateral tyre force increases from the linear region to the nonlinear region and is close to or even beyond the saturation point. In addition, the inner boundaries of the sideslip angle are different with respect to the different road adhesion coefficients[19, 20]. Therefore, the method for estimating the road adhesion coefficient is developed through determining precisely the point that the vehicle reaches the nonlinear region, and thus calculating the corresponding sideslip angle.

However, if the lateral tyre force does not have a distinct transformation from the linear region to the nonlinear region when the change of the steering angle is quite small, it is necessary to take this case into account when developing the estimation methods. Figure 7.24 shows the simulation results of the sideslip angles for a road adhesion coefficient of 0.4 and 0.9, respectively, when the same yaw rate illustrated in Figure 7.25 is maintained. The simulation results demonstrate that the sideslip angle for the low road adhesion coefficient is larger than that for the high road adhesion coefficient when the yaw
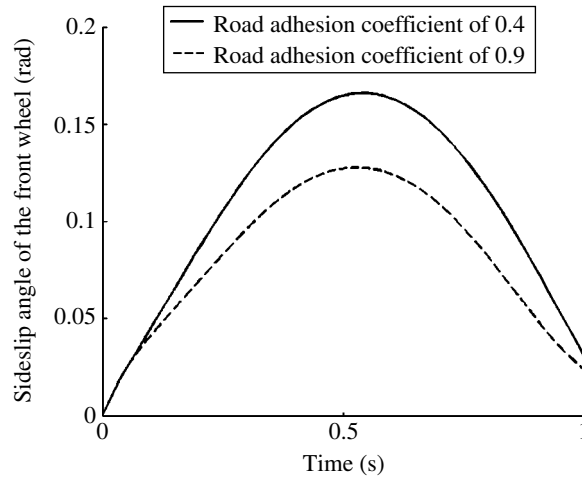
Figure 7.24 Sideslip angle for different road adhesion coefficient.
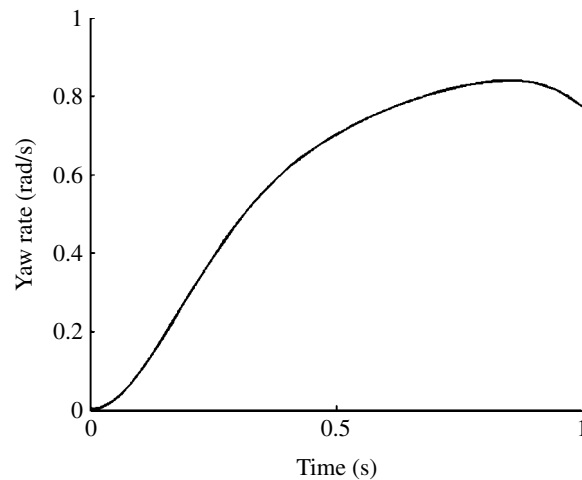
Figure 7.25 Yaw rate.

rate stays the same. The reason is that the sideslip angle must increase for the low road adhesion coefficient in order to provide the same lateral tyre force. Therefore, this characteristic is applied to design the estimation method when the change of the steering angle is quite small.

Moreover, as illustrated in Figure 7.26, it is observed that the vertical load has a great effect on the sideslip angle and the lateral tyre force. In this case, it may not be precise enough to estimate the road adhesion coefficient by using only one sideslip angle out of the four wheels. Therefore, the estimation method is proposed to use the sideslip angles of the two front wheels since the sideslip angles of the two rear wheels are relatively small.
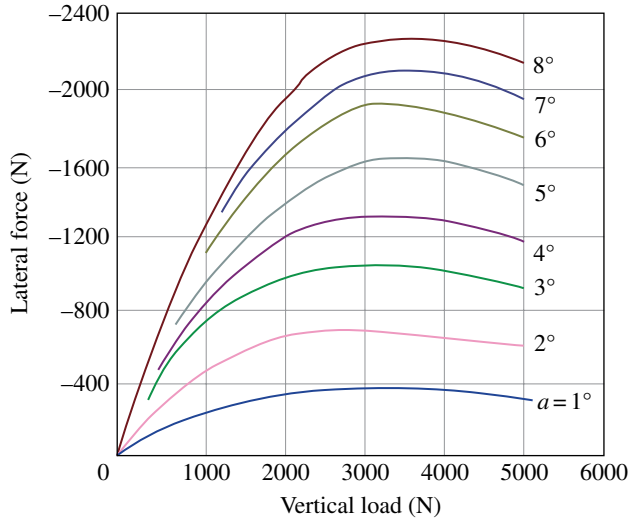
Figure 7.26   Effects of vertical load on the wheel sideslip characteristics.

7.2.2.1   Estimation of the Sideslip Angle

As discussed above, the estimation of the sideslip angle is important for the estimation of the road adhesion coefficient. thus, the accuracy of the estimation of the road adhesion coefficient is mainly determined by the accuracy of the sideslip angle. To achieve this aim, an extended Kalman filter is used to accurately estimate the vehicle velocity v_x and v_y, and then the sideslip angle is calculated according to the wheel model. For the Kalman filter developed in this section, the vehicle velocity, which is calculated from the 2-DOF vehicle dynamic model, is used as the estimated value, while the acceleration calculated from the 7-DOF vehicle model is used for calculating the measured value. Thus, the Kalman filter is derived as:

$$x_{k+1} = A_k x_k + B u_k + \omega \tag{7.36}$$

$$y_k = C x_k + \varepsilon \tag{7.37}$$

where $x_k = \begin{pmatrix} v_{xk} \\ v_{yk} \end{pmatrix}; u_k = \begin{pmatrix} a_{xk} \\ a_{yk} \end{pmatrix}; y_k = \begin{pmatrix} v_{xak} \\ v_{yak} \end{pmatrix}; A_k = \begin{pmatrix} 1 & T\varepsilon_k \\ -T\varepsilon_k & 1 \end{pmatrix}; B = \begin{pmatrix} T & 0 \\ 0 & T \end{pmatrix}; C = \begin{pmatrix} 1 & 0 \\ 0 & 1 \end{pmatrix};$

a_x and a_y are the longitudinal and lateral acceleration, respectively; T is the period of sampling cycle; v_{xa} and v_{ya} are the longitudinal and lateral vehicle velocity calculated from the 2-DOF vehicle dynamic model, respectively; k is the number of iterations; ε and ω are the measured error and prediction error of the system model. It is assumed that they are independent of each other and subject to the Gaussian distribution, and their covariances are denoted as R and Q. Therefore, the expanded Kalman filter proceeds in two steps. In the

first step, the sampling value and error increment between the two samplings are calculated according to equation (7.38) and equation (7,39).

$$\hat{x}_{k|k-1} = A_k x_{k-1|k-1} + Bu_{k-1} \tag{7.38}$$

$$P_{k|k-1} = F_k P_{k-1|k-1} F^T + Q \tag{7.39}$$

where $\hat{x}_{k|k-1}$ is the prediction value; $P_{k|k-1}$ is the covariance of the prediction error; and $F_k = \dfrac{\partial f(x)}{\partial(x)}\Big|_{x=\hat{x}_{k-1|k-1}}$ is the dynamic matrix obtained by the linearized system state equation when calculating $\hat{x}_{k-1|k-1}$. For the second step, the measured value is amended according to the system prediction value and prediction error during the sampling, as expressed in equations (7.40)–(7.42).

$$K_k = P_{k|k-1} H_k^T \left(H_k P_{k|k-1} H_k^T + R \right)^{-1} \tag{7.40}$$

$$\hat{x}_{k|k} = \hat{x}_{k-1|k-1} + K_k \left[y_k - C\hat{x}_{k-1|k-1} \right] \tag{7.41}$$

$$P_{k|k} = P_{k|k-1} - K_k H_k P_{k|k-1} \tag{7.42}$$

where $H_k = \dfrac{\partial f(x)}{\partial(x)}\Big|_{x=\hat{x}_{k|k-1}}$ is the matrix obtained by the linearized system output equation in the prediction process.

7.2.2.2 Proposed Estimation Method of the Road Adhesion Coefficient

The block diagram of the estimation method of the road adhesion coefficient is shown in Figure 7.27. First, the vehicle longitudinal and lateral velocity is calculated by the expanded Kalman filter according to the outputs of the 7-DOF vehicle dynamic model and the 2-DOF vehicle dynamic model. Then, the parameters required for the road estimation method are calculated from the 7-DOF vehicle dynamic model, including the yaw rate gain, front steering angle, and yaw rate. Finally, the adhesion coefficient is estimated by the trained neural network. Obviously, the whole estimation process is an open loop system.

The linear boundary limitation shown in Section 7.2.1 introduces the approach to determine if the vehicle is under a nonlinear state according to the yaw rate gain. However, the yaw rate gain is a fixed value, and hence it is not accurate enough to determine the vehicle state according to the r/δ_f threshold. To overcome this difficulty, the error Back Propagation (BP) neural network[21–25] is adopted since it is effective in handling nonlinear problems because of the learning ability of the neural network algorithm. Moreover, the genetic algorithm optimization method is applied to the BP neural network. Therefore, the accuracy of determination of the vehicle state can be improved significantly through heavy learning on some typical test results.
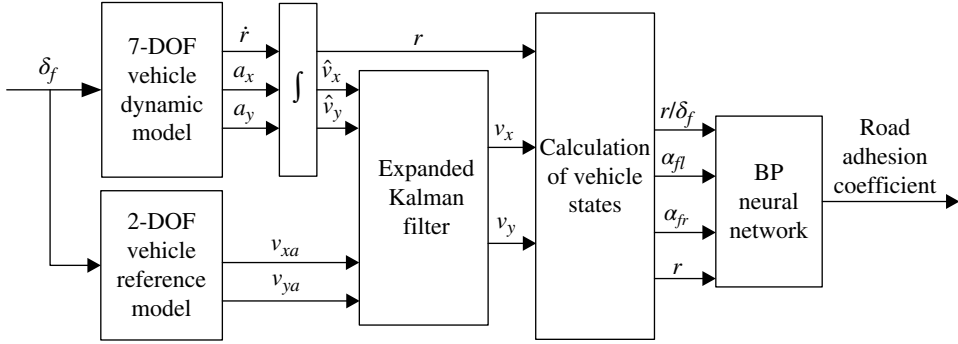
Figure 7.27   Block diagram of the road estimation method.
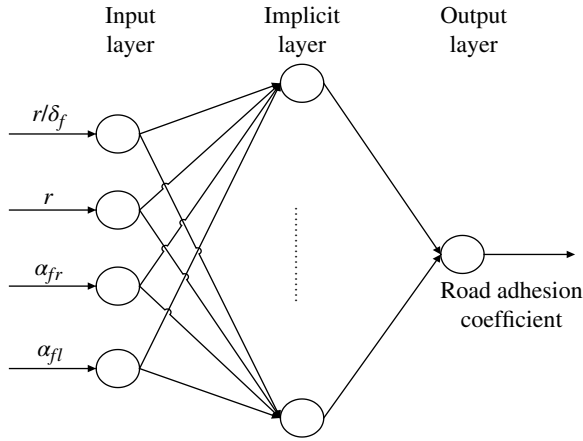
Figure 7.28   Three-layer BP neural network structure.

The BP neural network uses a three-layer feed forward structure as illustrated in Figure 7.28. There are four nodes on the input layer, including the yaw rate gain r/δ_f, side slip angles of the two front wheels α_{fl}, α_{fr}, and yaw rate r; one output node on the output layer, i.e., the road adhesion coefficient; the nodes on implicit layer are determined by the test results during the learning process.

A genetic algorithm is used to optimize the weighting parameters of each node in the neural network. E is defined as the overall training error of the network

$$\min E = f\left\{x_1, x_2, \cdots, x_s\right\} = f\left\{w_1, w_2, \cdots, w_M, \theta_1, \theta_2, \cdots, \theta_K\right\} \tag{7.43}$$

where $x_i\left(i = 1, 2, \cdots, s\right)$ is a set of chromosome; s is the summation of the number of the weighting parameters and the number of the thresholds of all the nodes; w_i is the i-th connection weighting parameter of the network; M is the total number of the connection
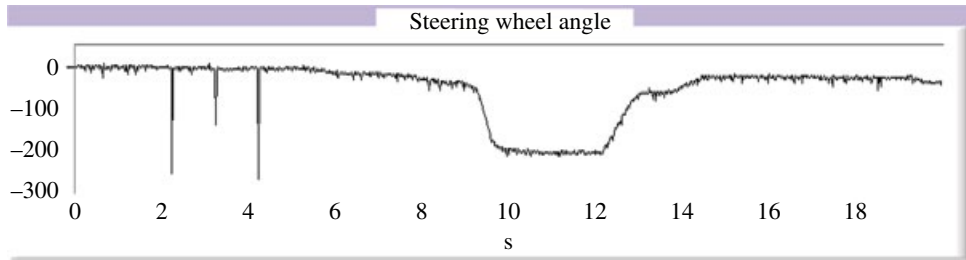
Figure 7.29   Steering angle of the front wheel under the maneuver of step steering.

weighting parameters; θ_K is the threshold of the K-th neuron; and K is the total number of neurons on the implicit and output layers. In addition, the following weighting parameters must be determined in the neural network: the connection weighting parameters w_{ik} between the nodes on the input and implicit layer, and the connection weighting parameters w_{kp} between the nodes on the implicit and output layer; θ_K is the threshold of the neuron on the implicit layer; and θ_p is the threshold of the neuron on the output layer. The following steps of the optimization process are performed:

1. Code the network connection weighting parameters by real numbers.
2. Generate randomly an initial population using the small cluster generation method.
3. Evaluate the performance of the individuals according to a fitness function. The fitness function $f(x)$ is defined as the reciprocal of the error, i.e., $f(x) = 1/E(x)$.
4. Obtain the initial network connection weighting parameters by decoding every individual. Then, the overall error is calculated by inputting the initial network connection weighting parameters and the samples.
5. Select, crossover, and mutate the parent population and produce the next generation of population.
6. Calculate the fitness value of each individual in the current generation and sort them in an ascending order.
7. Obtain the optimal initial weighting parameters of the BP network by decoding the optimal individual. Then calculate the overall error E after adjusting the weighting parameters.
8. If the overall error E is less than the assigned target value, the training is terminated. Otherwise, the weighting parameters obtained from the current optimization process is used as the initial weighting parameter of the next training, and step (5) is repeated.

The training sample of the proposed BP neural network is selected from the VSC test results performed on a test vehicle[15]. The adhesion coefficient of the test road is approximately 0.8. Figures 7.29–7.32 show the measured steering angle at the wheel and the yaw rate under the maneuver of step steering and double lane change. The side slip angles of the two front wheels can be calculated by the test results.
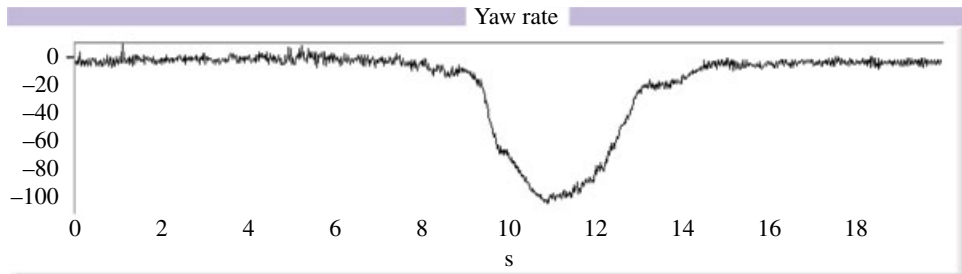
Figure 7.30   Yaw rate under the maneuver of step steering.
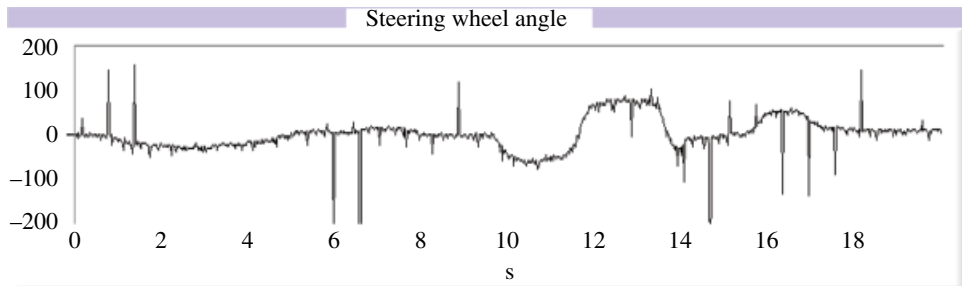
Figure 7.31   Steering angle of the front wheel under the maneuver of double lane change.
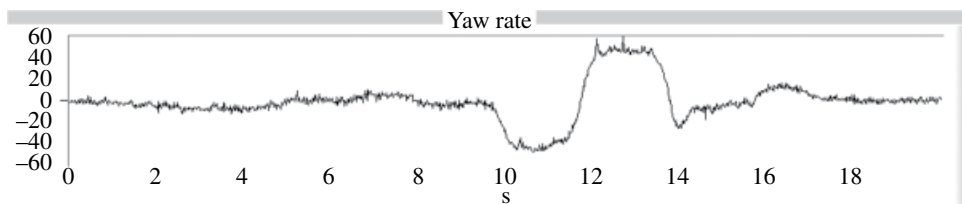
Figure 7.32   Yaw rate under the maneuver of double lane change.

7.2.2.4   Simulation Investigation

To demonstrate the performance of the proposed estimation method of the road adhesion coefficient a simulation investigation is performed by selecting the road adhesion coefficient as 0.9 and 0.4, respectively, and the vehicle speed is set as 60 km/h. A sinusoidal input is given as the steering angle. The simulation model is constructed in Simulink as shown in Figure 7.33, and the simulation results are illustrated in Figures 7.34 and 7.35.

It can be seen from Figures 7.34 and 7.35, and Table 7.2 that the proposed estimation method is able to estimate accurately the road adhesion coefficient for both high and low adhesion coefficients, with an acceptable error. In addition, it can be observed that there are small undulations in the simulation results since the proposed estimation method is open loop; hence, it lacks feedback and self-adjusting mechanisms to compensate for the estimation results.
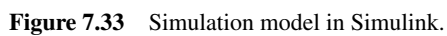
Figure 7.33 Simulation model in Simulink.
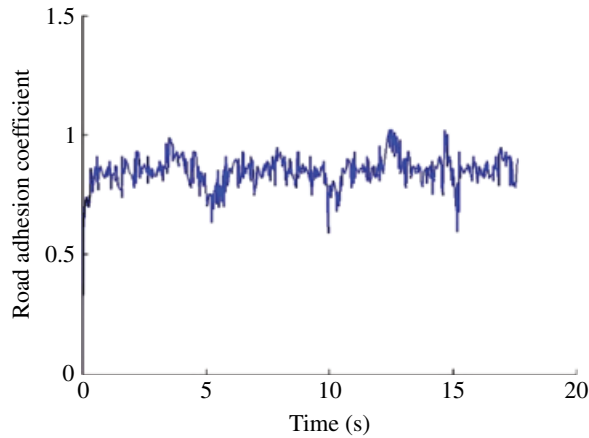
Figure 7.34   Estimation of a high road adhesion coefficient of 0.9.
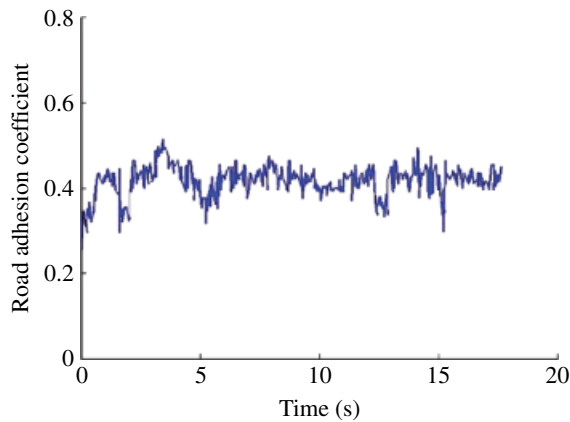
Figure 7.35   Estimation of a low road adhesion coefficient of 0.4.

Table 7.2   Estimation results for high and low adhesion coefficients.

Adhesion coefficient	Mean value	Error
0.9	0.87	3.3%
0.4	0.41	2.5%

7.3   Integrated Control of Active Suspension System (ASS) and Vehicle Stability Control System (VSC) using Decoupling Control Method

Vehicle Stability Control (VSC) system generates a proper yaw moment on the vehicle through the tyre braking or driving forces, and hence improve the vehicle performance in both the lateral and yaw motions. In addition, the active suspension system (ASS) is able
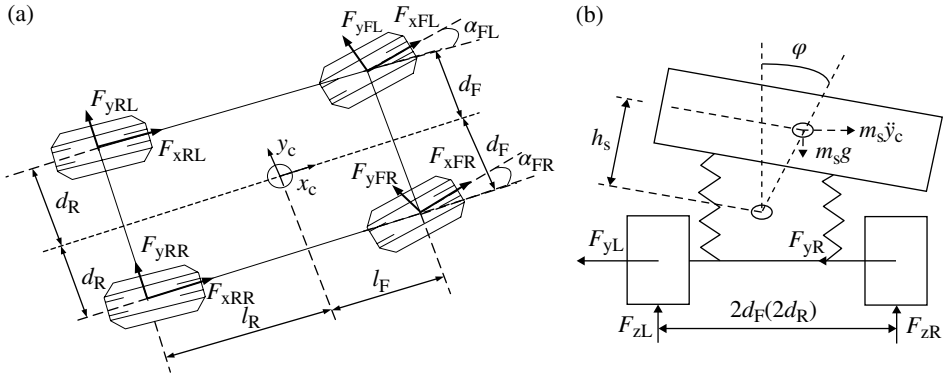
Figure 7.36   7-DOF Vehicle dynamic model. (a) Longitudinal and lateral motion. (b) Pitch motion.

to control the vehicle attitude and regulate the vehicle vertical load transfer during pitch and roll motions by adjusting the suspension stiffness and damping characteristics. Therefore, the main purpose of integrating the VSC with the ASS is to improve the overall vehicle performance, including the lateral stability and ride comfort, through the coordinated control of the VSC and ASS system, especially under critical driving conditions.

7.3.1   Vehicle Dynamic Model

To develop the integrated control of VSC and ASS, the 7-DOF dynamic model is established by considering the interactions between the VSC and ASS, which is analyzed in Chapter 6. The dynamic model shown in Figure 7.36 includes both the VSC and ASS, and the equations of motion can be derived as follows.

Lateral motion

$$m\dot{x}_c\left(\dot{\beta}+r\right)+m_s\left(-\dot{z}_c\dot{\varphi}-h_s\ddot{\varphi}+h_s\dot{\theta}r\right)=2\left(F_{yF}\cos\delta_f+F_{yR}+k_{\alpha F}E_F\varphi+k_{\alpha R}E_R\varphi\right) \quad (7.44)$$

Yaw motion

$$\begin{aligned}I_z\dot{r}-I_{zx}\ddot{\varphi}+I_{zx}\dot{\theta}r+\left(I_{ys}-I_{xs}\right)\dot{\varphi}\dot{\theta}-m_sl_s\dot{z}_s\dot{\varphi}\\=2\left(F_{yF}\cos\delta_f l_F+F_{yR}l_R+l_F k_{\alpha F}E_F\varphi-l_R k_{\alpha R}E_R\varphi\right)+\Delta M\end{aligned} \quad (7.45)$$

Vertical motion

$$m_s\left(\ddot{z}_s-\dot{x}_c\dot{\theta}+\dot{y}_c\dot{\varphi}\right)-m_sh_s\left(\dot{\theta}^2+\dot{\varphi}^2\right)+m_sl_sr\dot{\theta}=-\left(F_{FL}+F_{FR}+F_{RL}+F_{RR}\right) \quad (7.46)$$

where
$$F_{\text{FL}} = -k_{\text{sFL}} \left(z_{\text{sFL}} - z_{\text{uFL}} \right) - c_{\text{sFL}} \left(\dot{z}_{\text{sFL}} - \dot{z}_{\text{uFL}} \right) + f_{\text{FL}}$$
$$F_{\text{FR}} = -k_{\text{sFR}} \left(z_{\text{sFR}} - z_{\text{uFR}} \right) - c_{\text{sFR}} \left(\dot{z}_{\text{sFR}} - \dot{z}_{\text{uFR}} \right) + f_{\text{FR}}$$
$$F_{\text{RL}} = -k_{\text{sRL}} \left(z_{\text{sRL}} - z_{\text{uRL}} \right) - c_{\text{sRL}} \left(\dot{z}_{\text{sRL}} - \dot{z}_{\text{uRL}} \right) + f_{\text{RL}}$$
$$F_{\text{RR}} = -k_{\text{sRR}} \left(z_{\text{sRR}} - z_{\text{uRR}} \right) - c_{\text{sRR}} \left(\dot{z}_{\text{sRR}} - \dot{z}_{\text{uRR}} \right) + f_{\text{RR}}$$

Roll motion

$$
\begin{aligned}
I_{\text{xu}}\ddot{\varphi} - I_{\text{xzu}}\dot{r} - \left(I_{\text{zs}} - I_{\text{ys}} - m_s h_s h \right)\dot{\theta} r - I_{\text{zxs}}\dot{\varphi}\dot{\theta} + m_s h \dot{z}_c \dot{\varphi} - m_s \left(\dot{y}_c + \dot{x}_c r \right) h \\
= \left(F_{\text{FL}} - F_{\text{FR}} \right) d_{\text{F}} + \left(F_{\text{RL}} - F_{\text{RR}} \right) d_{\text{R}}
\end{aligned}
\tag{7.47}
$$

Pitch motion

$$I_{\text{ys}}\ddot{\theta} + \left(I_{\text{xs}} - I_{\text{zs}} \right)\dot{\varphi} r - I_{\text{zxs}} \left(r^2 - \dot{\varphi}^2 \right) - \left(F_{\text{FL}} + F_{\text{FR}} \right) \left(l_{\text{F}} - l_s \right) + \left(F_{\text{RL}} + F_{\text{RR}} \right) \left(l_{\text{F}} + l_s \right) = 0 \tag{7.48}$$

$$m_{\text{ui}}\ddot{z}_{\text{ui}} = F_{\text{i}} \qquad \text{i} = \text{FL, FR, RL, RR} \tag{7.49}$$

where m, m_s, and m_u are the vehicle mass, sprung mass, and unsprung mass, respectively; x_c, y_c, and z_c are the Cartesian coordinates of the vehicle center of gravity; x_s, y_s, and z_s are the Cartesian coordinates of the center of gravity of the sprung mass; u_c is the vehicle longitudinal speed; φ and θ are the pitch and roll angles, respectively ; r is the yaw rate of the vehicle; δ_f is the steering angle of the front wheel; F_{YF} and F_{YR} are the front and rear lateral tyre forces, respectively; E_{F} and E_{R} are the roll camber coefficients of the front and rear wheels, respectively; $k_{\alpha\text{F}}$ and $k_{\alpha\text{R}}$ are the cornering stiffness of the front and rear tyres, respectively; h is the height of the vehicle center of gravity; h_s is the vertical distance between the centers of gravity of both the vehicle and the sprung mass; I_z is the moment of inertia of the vehicle mass about axis z_c; I_{zx} is the product of inertia of the vehicle mass about axis x_c and z_c; I_{xu} is the moment of inertia of the sprung mass about axis x_c; I_{xs}, I_{ys}, and I_{zs} are the moments of inertia of the sprung mass about axis x_s, y_s, z_s, respectively; I_{xzu} is the product of inertia of the sprung mass about axis x_c and z_c; I_{zxs} is the product of inertia of the sprung mass about axis x_s and z_s; ΔM is the vehicle corrective yaw moment generated by VSC; l_s is the longitudinal distance between the centers of gravity of the vehicle mass and sprung mass; l_F and l_R are the longitudinal distances between the vehicle center of gravity and the front and rear axles, respectively; $f_{\text{FL}}, f_{\text{FR}}, f_{\text{RL}},$ and f_{RR} are the front-left, front-right, front-left, and rear-left, and rear-right control forces of the active suspension, respectively; z_{ui} is the vertical displacement of the i-th unsprung mass; c_{si} is the damping coefficient of the i-th damper; k_{si} is the suspension stiffness of the i-th suspension; d_{F} and d_{R} are the half of front and rear wheel track, respectively.

7.3.2   2-DOF Reference Model

The 2-DOF vehicle linear dynamic model is adopted as the vehicle reference model to generate the desired vehicle states in this study since the 2-DOF model reflects the desired relationship between the driver's steering input and the vehicle yaw rate.

The equations of motion are expressed as follows by assuming a small sideslip angle and a constant forward speed.

$$mu_c\left(\dot{\beta}+r\right) = -2k_{\alpha F}\left(\beta+l_F\frac{r}{u_c}-\delta_f\right) - 2k_{\alpha R}\left(\beta-l_R\frac{r}{u_c}\right)$$
(7.50)

$$I_z\dot{r} = -2k_{\alpha F}\left(\beta+l_F\frac{r}{u_c}-\delta_f\right)l_F + 2k_{\alpha R}\left(\beta-l_R\frac{r}{u_c}\right)l_R + \Delta M$$
(7.51)

7.3.3   Lateral Force Model

To simplify the design of the integrated control system, a small sideslip angle is assumed and hence the tyre displacement is linear. Therefore, the front and rear lateral forces are derived by considering the vehicle roll steering effect:

$$F_{yF} = k_{\alpha F}\left(\delta_f-\beta-l_F\frac{r}{u_c}+G_F\varphi\right)$$
(7.52)

$$F_{yR} = k_{\alpha R}\left(-\beta+l_R\frac{r}{u_c}+G_R\varphi\right)$$
(7.53)

where G_F and G_R are the roll steering coefficients of the front and rear axles, respectively.

7.3.4   Integrated System Control Model

The state variables are defined as follows for the integrated VSC and ASS control system, by combining equations (7.44)–(7.49), and equations (7.52) and (7.53).

$$\boldsymbol{x} = \begin{pmatrix} z_{uFL} & z_{uFR} & z_{uRL} & z_{uRR} & \dot{z}_{uFL} & \dot{z}_{uFR} & \dot{z}_{uRL} & \dot{z}_{uRR} & z_c & \dot{z}_c & \varphi & \dot{\varphi} & \theta & \dot{\theta} & r & \beta \end{pmatrix}^{\mathrm{T}}$$
(7.54)

   In addition, the variables of the external disturbance for the integrated control system are defined as:

$$\boldsymbol{w} = \begin{pmatrix} z_{0FL} & z_{0FR} & z_{0RL} & z_{0RR} & \delta_f \end{pmatrix}^{\mathrm{T}}$$
(7.55)

where z_{0i} is the stochastic excitation of each tyre generated by the road unevenness; and δ_f is the steering angle of the front wheel generated by the driver. As mentioned earlier in this chapter, the VSC system generates an additional yaw moment to track the desired vehicle states, and the ASS adjusts the suspension stiffness and damping characteristics to improve the vehicle ride comfort, and also indirectly improves the handling stability through regulating the load transfer. Therefore, the control input variables for the integrated control system are defined as:

$$\boldsymbol{u} = \begin{pmatrix} \Delta M & f_{FL} & f_{FR} & f_{RL} & f_{RR} \end{pmatrix}^{\mathrm{T}}$$
(7.56)

The goal of the integrated VSC and ASS control system is to improve the vehicle handling stability and ride comfort. Therefore, the output variables of the integrated control system include the vehicle yaw rate r, the sideslip angle β, the vertical acceleration at the vehicle center of gravity $\ddot{z}_c$, the suspension deflection f_d, and the vehicle roll angle φ, by considering the measurability of these signals,

$$\boldsymbol{y} = \begin{pmatrix} r & \beta & \ddot{z}_c & f_d & \varphi \end{pmatrix}^{\mathrm{T}} \tag{7.57}$$

The state equation and the output equation are then obtained as:

$$\begin{cases} \dot{\boldsymbol{x}} = \boldsymbol{A}\boldsymbol{x} + \boldsymbol{B}_1\boldsymbol{u} + \boldsymbol{B}_2\boldsymbol{w} + \boldsymbol{f}(\boldsymbol{x},t) \\ \boldsymbol{y} = \boldsymbol{C}\boldsymbol{x} + \boldsymbol{D}\boldsymbol{u} \end{cases} \tag{7.58}$$

where $\boldsymbol{A}, \boldsymbol{C}$ are the 16×16 input matrix and the 5×16 output matrix, respectively; $\boldsymbol{B}_1, \boldsymbol{B}_2$ are the 16×1 input matrices; $\boldsymbol{D}$ is the 16×1 direct transfer matrix; $\boldsymbol{f}(\boldsymbol{x},t)$ is the coupling term of the state variable with size of 16×1.

It is clear that the VSC/ASS integrated control system defined in equation (7.58) is a typical multivariable nonlinear system. Due to the correlations between the tyre longitudinal and vertical forces, and also the interactions among the roll, pitch, and lateral motions, the VSC and ASS are highly coupled. The coupling effects, i.e., a certain control input affecting multiple outputs, are caused by the coupling correlation term included in the state variable. Therefore, it is required to decouple the above-mentioned five control loops and hence achieve that a certain output is controlled solely by one control input in order to improve the overall vehicle performance.

7.3.5   Design of the Decoupling Control System

The decoupling method of nonlinear system is applied to the integrated VSC and ASS system established in equation (7.58) to derive the state feedback control law[26].

7.3.6   Calculation of the Relative Degree

According to the decoupling theory of nonlinear system, the calculation of the relative degree of the original integrated control system is required in order to apply the state feedback control and transform the original nonlinear coupled system into the independent decoupled subsystems. The calculation process is described as follows: first, the derivatives of the control output $\boldsymbol{y}$ are computed with respect to time. Various orders of the derivatives continue to be computed until the input variable $\boldsymbol{u}$ is included explicitly in the output derivative function. Thus, the corresponding derivative order is the system relative degree. In addition, the rank of the Jacobian matrix can be determined through the Interactor algorithm of nonlinear systems[27]. The detailed calculation of the relative degree is demonstrated below.

1. Perform the derivative of the control output variable y_1 with order $R_1 = 1$:

$$y_1 = r$$

$$\dot{y}_1 = \dot{r} = \frac{1}{I_z}\Big[I_{zx}\ddot{\varphi} - I_{zx}\dot{\theta}r - \big(I_{ys} - I_{xs}\big)\dot{\varphi}\dot{\theta} + m_s l_s \dot{z}_c\dot{\varphi} + 2F_{yF}\cos\delta_f l_F$$
$$+ 2F_{yR}l_R + 2l_F k_{\alpha F}E_F\varphi - 2l_R k_{\alpha R}E_R\varphi + \Delta M \Big]$$

Let $Y_1 = \dot{y}_1$, then $\partial Y_1/\partial u^{\mathrm{T}} = \begin{pmatrix} 0 & 0 & 0 & 0 & \dfrac{1}{I_z} \end{pmatrix}$, and $t_1 = \mathrm{rank}\big(\partial Y_1/\partial u^{\mathrm{T}}\big) = 1$.

2. Perform the derivative of the system output variable y_2 with order $R_2 = 1$:

$$y_2 = \beta$$

$$\dot{y}_2 = \dot{\beta} = -r - \frac{1}{mu_c}\Big[m_s\big(-\dot{z}_c\dot{\varphi} - h_s\ddot{\varphi} + h_s\dot{\theta}r\big) + 2\big(F_{yF}\cos\delta_f + F_{yR} + k_{\alpha F}E_F\varphi + k_{\alpha R}E_R\varphi\big)\Big]$$

Since the control input u is not included explicitly in $\dot{y}_2$, the derivative of the system output y_2 with order $R_2 = 2$ is then computed:

$$\dot{y}_2 = \ddot{\beta} = -\frac{1}{mu_c}\Big[m_s\big(-\dot{z}_c\dot{\varphi} - h_s\ddot{\varphi} + h_s\dot{\theta}r\big) + 2\big(F_{yF}\cos\delta_f + F_{yR} + k_{\alpha F}E_F\varphi + k_{\alpha R}E_R\varphi\big)\Big] - \frac{1}{I_z}[I_{zx}\ddot{\varphi}$$
$$- I_{zx}\dot{\theta}r - \big(I_{ys} - I_{xs}\big)\dot{\varphi}\dot{\theta} + m_s l_s \dot{z}_c\dot{\varphi} + 2F_{yF}\cos\delta_f l_F + 2F_{yR}l_R + 2l_F k_{\alpha F}E_F\varphi - 2l_R k_{\alpha R}E_R\varphi + \Delta M]$$

Let $Y_2 = \big(Y_1 \;\; \ddot{y}_2\big)^{\mathrm{T}}$, $\partial Y_2/\partial u^{\mathrm{T}} = \begin{pmatrix} 0 & 0 & 0 & 0 & \dfrac{1}{I_z} \\[2mm] \dfrac{-I_{zx}d_F}{I_z I_x} & \dfrac{I_{zx}d_F}{I_z I_x} & \dfrac{-I_{zx}d_R}{I_z I_x} & \dfrac{I_{zx}d_R}{I_z I_x} & \dfrac{-1}{I_z} \end{pmatrix}$, then

$t_2 = \mathrm{rank}\big(\partial Y_2/\partial u^{\mathrm{T}}\big) = 2$.

3. For the integrated system output variable $y_3 = \ddot{z}_c$, it can be seen that the control input variables $f_{FL}, f_{FR}, f_{RL},$ and f_{RR} are included in y_3, then $R_3 = 0$.

$$y_3 = \ddot{z}_c = -\frac{1}{m_s}\big(F_{FL} + F_{FR} + F_{RL} + F_{RR}\big) + u_c\dot{\theta} - \dot{y}_c\dot{\varphi} + h_s\big(\dot{\theta}^2 + \dot{\varphi}^2\big) - c_s r\dot{\theta}$$

Let $Y_3 = \big(Y_1 \;\; \ddot{y}_2 \;\; y_3\big)^{\mathrm{T}}$, then $\partial Y_2/\partial u^{\mathrm{T}} = \begin{pmatrix} 0 & 0 & 0 & 0 & \dfrac{1}{I_z} \\[2mm] \dfrac{-I_{zx}d_F}{I_z I_x} & \dfrac{I_{zx}d_F}{I_z I_x} & \dfrac{-I_{zx}d_R}{I_z I_x} & \dfrac{I_{zx}d_R}{I_z I_x} & \dfrac{-1}{I_z} \\[2mm] \dfrac{-1}{m_s} & \dfrac{-1}{m_s} & \dfrac{-1}{m_s} & \dfrac{-1}{m_s} & 0 \end{pmatrix}$, and

$t_3 = \mathrm{rank}\big(\partial Y_3/\partial u^{\mathrm{T}}\big) = 3$.

4. Similarly, the derivatives of the system outputs y_4 and y_5 are performed. We obtain $R_4 = 2$ and $R_5 = 3$; and the system Jacobian matrices $\partial Y_4 / \partial u^{\mathrm{T}}$ and $\partial Y_5 / \partial u^{\mathrm{T}}$ are full ranked,i.e., the ranks are 4 and 5, respectively.

Therefore, the relative degree of the original integrated control system is $R = \begin{pmatrix} 1 & 2 & 0 & 2 & 3 \end{pmatrix}^{\mathrm{T}}$ according to the definition of the relative degree.

7.3.7   Design of the Input/Output Decoupling Controller

For the multivariable coupled integrated system, the purpose of the decoupling controller is to make a certain control input u_i $(i = 1,2,3,4,5)$ rely solely on the system state variable x and some other independent reference variables v_i $(i = 1,2,3,4,5)$ through developing the state feedback law. Thus, the system control input satisfies the following relationship:

$$u = \bar{\alpha}(x) + \bar{\beta}(x)v + \bar{r}(x)w \qquad (7.59)$$

When the state feedback law defined in equation (7.59) is applied on the coupled integrated system, the i-th component of the closed loop system output y_i is affected solely by the i-th reference variable v_i, and therefore the decoupling of the control channels of the close loop system is achieved.

According to the nonlinear decoupling control theory, the relative degree $R = \begin{pmatrix} 1 & 2 & 0 & 2 & 3 \end{pmatrix}^{\mathrm{T}}$ of the integrated control system is obtained by computation, and also the system Falb-Wolovich matrix (i.e., decoupling matrix) $E(x)$ at the equilibrium point is given as:

$$E(x) = \begin{pmatrix} L_{g1}L_f^{r_1-1}y_1(x) & L_{g2}L_f^{r_1-1}y_1(x) & L_{g3}L_f^{r_1-1}y_1(x) & L_{g4}L_f^{r_1-1}y_1(x) & L_{g5}L_f^{r_1-1}y_1(x) \\ L_{g1}L_f^{r_2-1}y_2(x) & L_{g2}L_f^{r_2-1}y_2(x) & L_{g3}L_f^{r_2-1}y_2(x) & L_{g4}L_f^{r_2-1}y_2(x) & L_{g5}L_f^{r_2-1}y_2(x) \\ L_{g1}L_f^{r_3-1}y_3(x) & L_{g2}L_f^{r_3-1}y_3(x) & L_{g3}L_f^{r_3-1}y_3(x) & L_{g4}L_f^{r_3-1}y_3(x) & L_{g5}L_f^{r_3-1}y_3(x) \\ L_{g1}L_f^{r_4-1}y_4(x) & L_{g2}L_f^{r_4-1}y_4(x) & L_{g3}L_f^{r_4-1}y_4(x) & L_{g4}L_f^{r_4-1}y_4(x) & L_{g5}L_f^{r_4-1}y_4(x) \\ L_{g1}L_f^{r_5-1}y_5(x) & L_{g2}L_f^{r_5-1}y_5(x) & L_{g3}L_f^{r_5-1}y_5(x) & L_{g4}L_f^{r_5-1}y_5(x) & L_{g5}L_f^{r_5-1}y_5(x) \end{pmatrix}$$

$$(7.60)$$

And the system matrix $b(x)$ is obtained as:

$$b(x) = \begin{pmatrix} L_f^{r_1}y_1(x) & L_f^{r_2}y_2(x) & L_f^{r_3}y_3(x) & L_f^{r_4}y_4(x) & L_f^{r_5}y_5(x) \end{pmatrix}^{\mathrm{T}} \qquad (7.61)$$

Therefore, the state feedback is defined as:

$$\begin{aligned} \bar{\alpha}(x) &= -E^{-1}(x)b(x) \\ \bar{\beta}(x) &= E^{-1}(x) \end{aligned} \qquad (7.62)$$

When the state feedback control law $u_1(x)$ is applied to the coupled integrated control system, the coupled integrated system is transformed into a decoupled system with independent control channels. The state feedback control law is represented as:

$$u_1(x) = \bar{\alpha}(x) + \bar{\beta}(x)v = -E^{-1}(x)b(x) + E^{-1}(x)v \tag{7.63}$$

7.3.8   Design of the Disturbance Decoupling Controller

The purpose of the system disturbance decoupling is to fulfill the independence between the control output y in the close loop system and the external disturbance w through designing an appropriate state feedback law. For the integrated control system, the state feedback control law is constructed as follows by assuming that the system external disturbance is measurable.

$$u_2(x) = -B_1^{-1}B_2 w \tag{7.64}$$

Therefore the state feedback control law of the coupled integrated system is designed by combining the developed input/output decoupling controller given in equation (7.63) and the disturbance decoupling controller given in equation (7.64).

$$u = u_1(x) + u_2(x) = -E^{-1}(x)b(x) + E^{-1}(x)v - B_1^{-1}B_2 w \tag{7.65}$$

7.3.9   Design of the Closed Loop Controller

The decoupled integrated system not only eliminates the coupling effects between the control channels, but reduces the influence of the external disturbance on the system control output variable. However, the independent reference variable v in the proposed state feedback control law is unable to improve the control performance of the integrated system since a corrective action is not applied to the independent reference variable. To overcome the problem, a composite controller is proposed through integrating the close loop controller and the decoupling controller in order to improve the overall quality of the system response. As illustrated in Figure 7.37, the proposed integrated control system is decoupled into five independent single-variable systems, and then the closed loop controller is applied to effectively control the decoupled integrated control system.

7.3.10   Design of the ASS Controller

A PID controller is applied to improve the control performance of the closed loop ASS. By considering the ASS control target, the inputs of the PID controller are selected to include the differences e between the desired and the actual values of the vertical acceleration of the vehicle center of gravity, the suspension deflection, and the roll angle, which are given as:

$$e = \begin{pmatrix} \ddot{z}_{cd} - \ddot{z}_c & f_{dd} - f_d & \varphi_d - \varphi \end{pmatrix}^{\mathrm{T}} \tag{7.66}$$
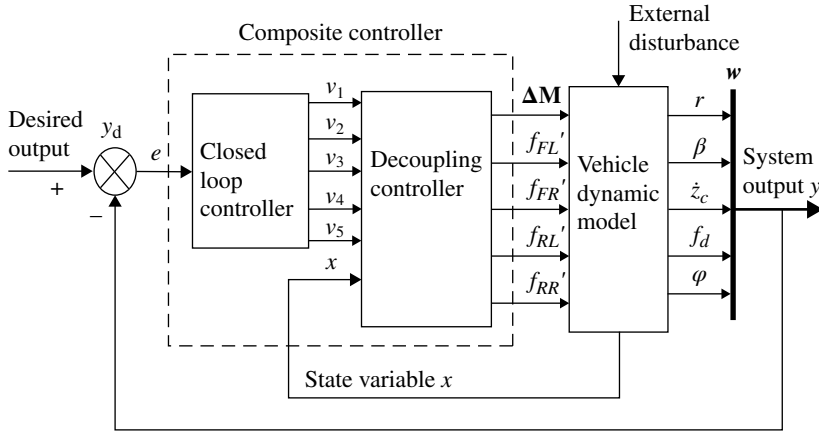
Figure 7.37   Block diagram of the integrated control system.
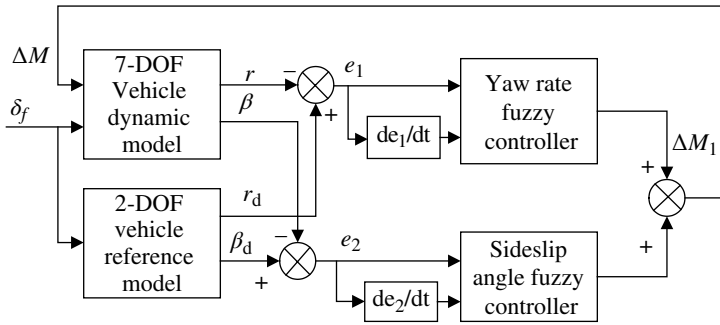
Figure 7.38   Block diagram of the fuzzy control system for the VSC.

Therefore, the PID control law is constructed as:

$$\boldsymbol{v} = \begin{pmatrix} v_2 & v_3 & v_4 & v_5 \end{pmatrix} = \boldsymbol{K}_{\mathrm{P}} \left(\boldsymbol{e}(t) + \frac{1}{\boldsymbol{T_I}} \int_0^t \boldsymbol{e}(t)\, dt + \boldsymbol{T}_{\mathrm{D}} \frac{d\boldsymbol{e}(t)}{dt} \right) \qquad (7.67)$$

7.3.11   Design of the VSC Controller

A fuzzy control strategy is used for the design of the VSC system, and the block diagram of the proposed VSC control system is shown in Figure 7.38. In the VSC fuzzy control system, the yaw rate and the sideslip angle are selected as the control objectives. As shown in the figure, the VSC fuzzy control system has two input variables, the tracking errors e_1 and e_2, and the differences of the errors ec_1 and ec_2 for the yaw rate and the

Table 7.3   Fuzzy rule bases for yaw rate.

ΔM_1		ec_1						
		NB	NM	NS	ZE	PS	PM	PB
e_1	NB	PB	PB	PB	PB	PM	ZE	ZE
	NM	PB	PB	PB	PB	PM	ZE	ZE
	NS	PM	PM	PM	PM	ZE	NS	NS
	ZE	PM	PM	PS	ZE	NS	NM	NM
	PS	PS	PS	ZE	NM	NM	NM	NM
	PM	ZE	ZE	NM	NB	NB	NB	NB
	PB	ZE	ZE	NM	NM	NB	NB	NB

Table. 7.4   Fuzzy rule bases for the sideslip angle.

ΔM_2		ec_2						
		NB	NM	NS	ZE	PS	PM	PB
e_2	NB	PB	PB	PM	PM	PS	ZE	ZE
	NM	PB	PB	PM	PM	PS	ZE	ZE
	NS	PB	PB	PM	PM	PS	ZE	NM
	ZE	PB	PM	PM	ZE	NM	NM	NB
	PS	PM	PM	ZE	NS	NM	NM	NB
	PM	ZE	ZE	NS	NS	NM	NM	NB
	PB	ZE	ZE	NS	NM	NM	NM	NB

sideslip angle, respectively. The output variables are defined as the corrective yaw moments ΔM_1 and ΔM_2. Thus, the overall corrective yaw moment is defined as a linear combination of the two:

$$\Delta M = n\Delta M_1 + (1-n)\Delta M_2 \tag{7.68}$$

where n is the weighting coefficient.

   To determine the fuzzy controller output for the given error and its difference, the decision matrix of the linguistic control rules is designed and presented in Tables 7.3 and 7.4, respectively. In the tables, seven fuzzy sets are used to represent the states of the inputs and outputs, i.e., {PB,PM,PS,ZE,NS,NM,NB}. A trigonometric function is adopted as the basic membership function, and a trapezoidal function is used for the fuzzy boundary. In addition, the dividing density is relatively higher around the zero value (ZE) of the membership function of the fuzzy input, while it is relatively smaller at a distance from the ZE value, in order to improve the control sensitivity. These rules are determined based on expert knowledge and a large number of simulation results performed in the study. Finally, the outputs of the fuzzy controllers ΔM_1 and ΔM_2 are defuzzified by applying the centroid method to the fuzzy output.

7.3.12   *Simulation Investigation*

In order to evaluate the performance of the developed integrated control system, i.e., the centralized control system using decoupling control method, a simulation investigation is performed. The performance and dynamic characteristics of the integrated control system are analyzed using MATLAB/Simulink. The road excitation is set as the filtered white noise expressed in equation (7.58). After tuning the parameter setting for the integrated control system, we select $K_P = \text{diag}\{1.8, 1.8, 1.3\}$, $T_I = \text{diag}\{1.56, 3.75, 0.82\}$, and $T_D = \text{diag}\{0.77, 2.5, 0.4\}$ for the closed loop ASS controller; the weighting coefficient $n = 0.85$ in the VSC system fuzzy controller. The vehicle physical parameters are presented in Table 7.5. The centralized control using decoupling control method control and the decentralized control (i.e., the VSC and ASS subsystem controllers work independently) are compared to demonstrate the performance of the integrated control system. Three driving conditions are performed, including step steering input, single lane change, and double lane change. The following discussions are made by comparing the centralized control system with the decentralized control system on the corresponding performance indices.

Table 7.5   Vehicle physical parameters.

Symbol (unit)	Value
m(kg)	3018
m_s(kg)	2685
m_{ui}(kg)	333/4
r_0(m)	0.4
h(m)	0.938
h_s(m)	0.1
H(m)	0.838
d_F/d_R(m)	0.8/0.9
l_F/l_R(m)	1.84/1.88
l_s(m)	0.15
k_{ti}(i=1,2, 3,4)(N/m)	420000(1,2)/350000(3,4)
k_{si}(i=1, 2, 3,4)(N/m)	44444(1,2)/35000(3,4)
c_{si}(i=1,2,3,4) (N.s/m)	1200(1,2)/900(3,4)
$k_{\infty F}/k_{\infty R}$ (N/rad)	29890/50960
I_z(kg.m²)	10437
I_{zx}(kg.m²)	2030
I_{js}(j=x,y,z) (kg.m²)	1744/3000/9285
I_{xu}(kg.m²)	1996
I_{xzu}(kg.m²)	377.8
G_f/G_r	0.114/0.1
E_f/E_r	0.8/0.6
J_p(kg.m²)	0.06
k_s(N.m/rad)	90
B_p(N.m.s/rad)	0.3
d(m)	0.1
G(dimensionless)	20
G_0(m³/cycle)	5.0×10^{-6}

(1) Step steering input maneuver

The simulation is conducted according to GB/T6323.2-94 controllability and stability test procedure for automobiles – steering transient response test (steering wheel angle step input). The step steering input to the wheel is set as 1.57 rad and the vehicle drives around a circle at a constant speed of 60 km/h. The road adhesion coefficient is selected as 0.6. The simulation results are shown in Figure 7.39.

It is clearly shown in Figure 7.39(a)–(c) that the peak value of the vehicle vertical acceleration for the centralized control is reduced by 30.6% from $2.48\,\mathrm{m.s^{-2}}$ to $1.72\,\mathrm{m.s^{-2}}$, the peak value of the roll angle is reduced by 8.1% from 0.099 rad to 0.091 rad, and the peak value of the suspension deflection is reduced by 14.6% from 0.048 m to 0.041 m, compared with those for the decentralized control. The results indicate that the centralized integrated control system is able to decrease the influence from the external disturbance on the system control output through applying the disturbance decoupling controller since the road excitation has the major effect on the vehicle ride comfort.

It is observed that in Figure 7.39(d) and (e) that the overshoots of the yaw rate and side-slip angle for the centralized control are reduced by 13.1% and 7.2%, respectively, compared with those for the decentralized control. In addition, the settling time of the two performance indices are lessened by 37.5% and 26.4%, respectively. It is evident that the centralized control system using decoupling control method is able to improve effectively the transient characteristics of handling stability, and also suppress significantly the steady state responses of the yaw rate and sideslip angle.

(2) Single lane change maneuver

The simulation is performed according to the GB/T6323.1-94 controllability and stability test procedure for automobiles – Pylon course slalom test. For the maneuver of a single lane change, the amplitude of the front wheel steering angle is set as 0.08 rad and the frequency as 0.3 Hz. The road adhesion coefficient and the vehicle speed are assumed to be 0.6 and 60km/h, respectively.

It is clearly illustrated in Figure 7.40 that the peak value of the yaw rate and the sideslip angle for the centralized control are reduced greatly by 33.3% from 0.24 rad/s to 0.16 rad/s, and by 22.2% from 0.09 rad to 0.07 rad, respectively; and the corresponding settling time by 26.8% from 4.1s to 3s, and by 31.9% from 4.7s to 3.2s, respectively, compared with those for the decentralized control. Similarly, the peak value of the roll angle is decreased by 31.7% from 0.082 rad to 0.056 rad. The results indicate that the centralized control system is able to maintain effectively the vehicle trajectory and hence improve the vehicle handling stability, compared with the decentralized control system.

(3) Double lane change maneuver

In order to investigate the adaptability of the developed centralized control system with respect to the variations of the vehicle physical parameters, three vehicle parameters are manipulated with a variation of ±10% by applying a sinusoidal function, including the vehicle mass, wheel base, and height of the vehicle center of gravity. However, the design and parameter setting of the decoupling controller are kept the same. The simulation is performed according to the GB/T6323.1-94 test. For the double lane change maneuver, the amplitude of the front steering angle is set

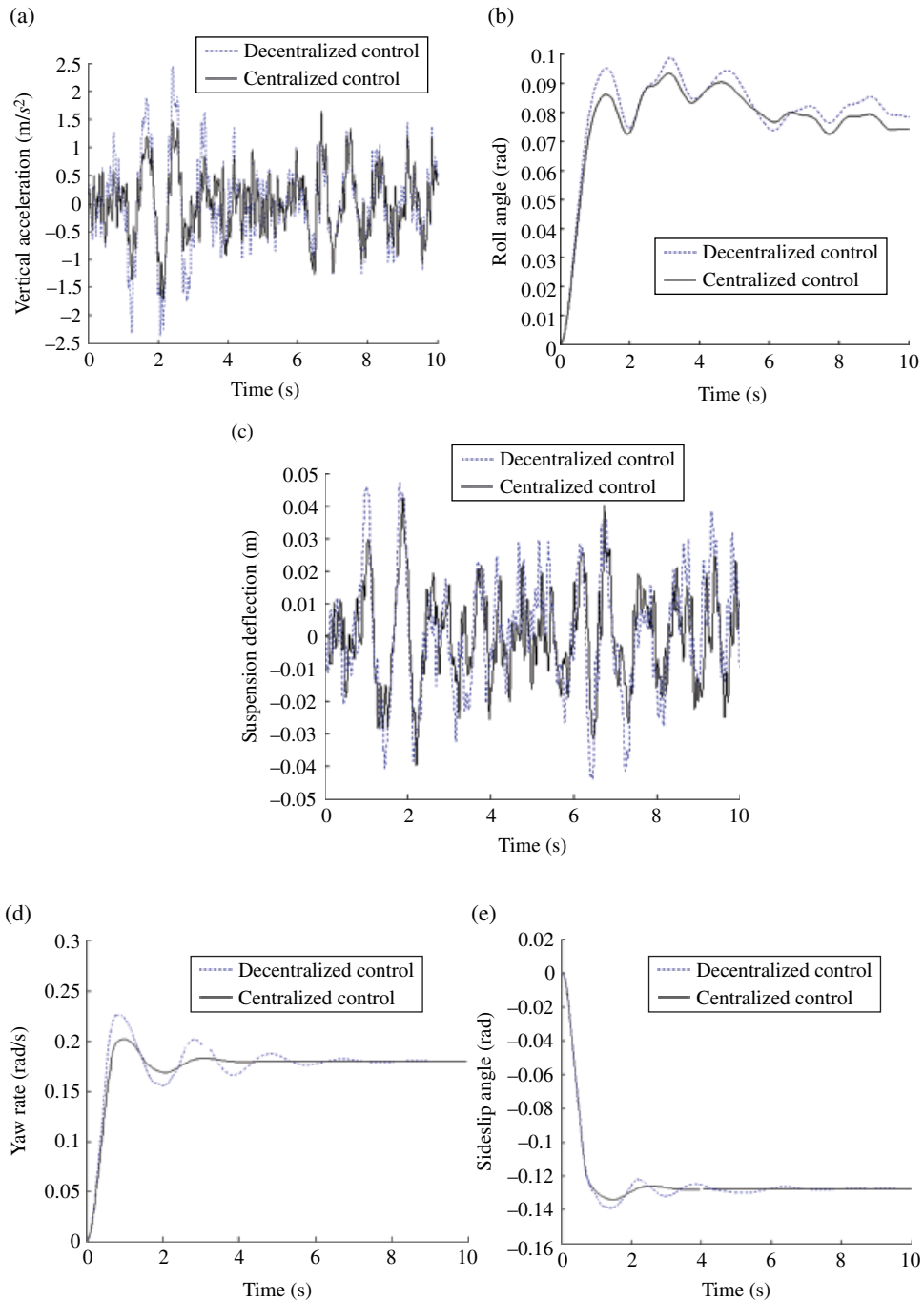(a)

(b)

(c)

(d)

(e)

Figure 7.39 Comparison of the responses for the maneuver of step steering input. (a) Vertical acceleration. (b) Roll angle. (c) Suspension deflection. (d) Yaw rate. (e) Sideslip angle.
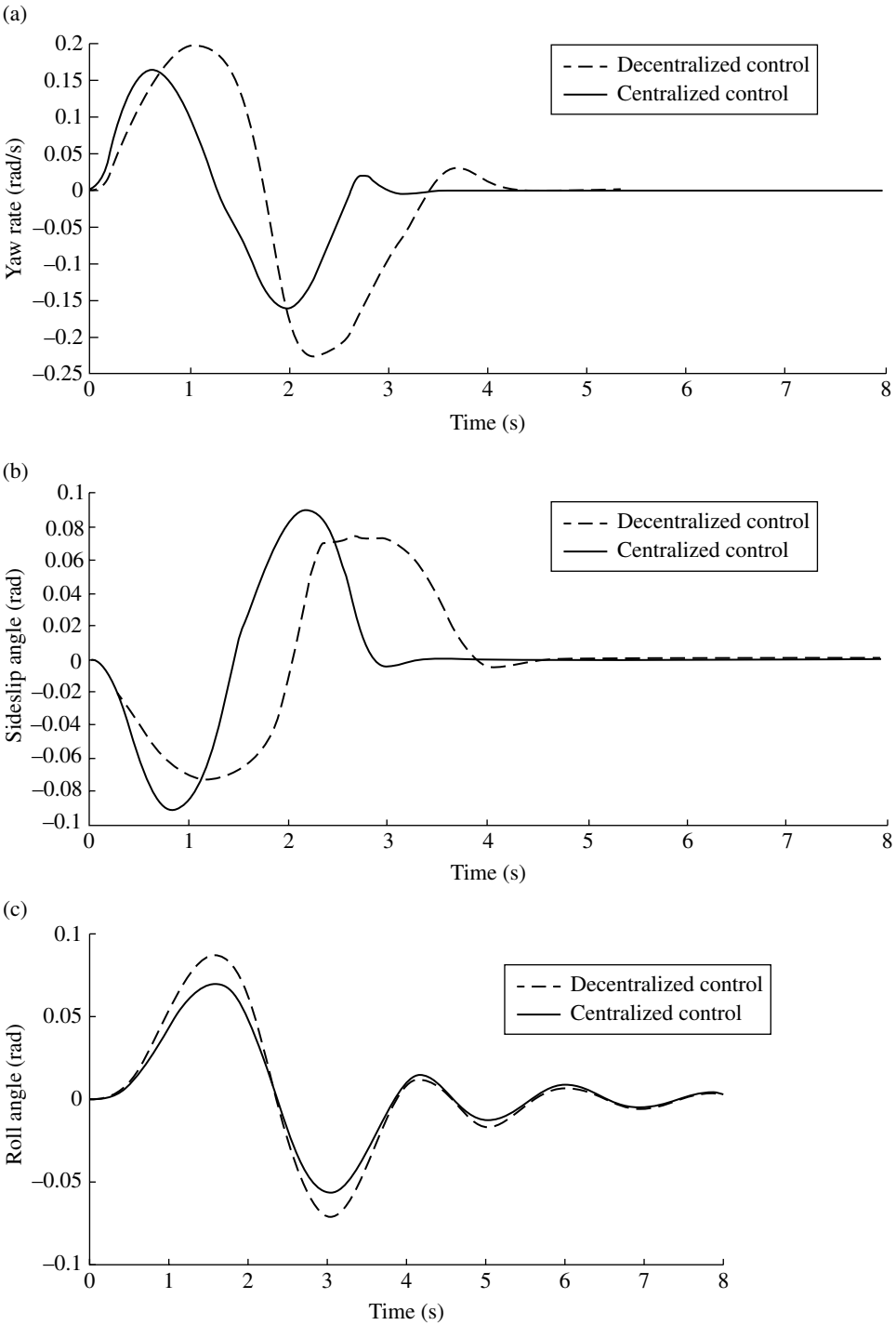
(a)

(b)

(c)

Figure 7.40 Comparison of responses for the single lane change maneuver. (a) Yaw rate. (b) Sideslip angle. (c) Roll angle.

as 0.06 rad, and frequency as 0.5 Hz, the road adhesion coefficient as 0.5, and the initial vehicle speed as 50 km/h.

It is observed in Figure 7.41 that the four performance indices for the centralized control are reduced slightly compared with those for the decentralized control. The results indicate that the adaptability of the centralized control system is insufficient to adapt the variation of the vehicle physical parameters since the accurate mathematical model and specific system physical parameters are required to develop the decoupling controller.

7.3.13   Experimental Study

To validate the effectiveness of the centralized integrated control system, a hardware-in-the-loop (HIL) experimental study is conducted based on LabVIEW PXI. As shown in Figure 7.42, the developed HIL system consists of a host computer, a client computer, an interface system, and the VSC and ASS actuators. The client computer (PXI-8196 manufactured by National Instruments Inc.) collects the signals measured by the sensors, which include the pressure of each brake wheel cylinder, the pressure of the brake master cylinder, and the vertical acceleration of the sprung mass at each suspension. These signals are in turn provided to the host computer (PC) through a LAN (local area network) cable. Based on these input signals, the host computer computes the vehicle states and the desired vehicle motions, such as the desired yaw rate. Thereafter, the host computer generates control commands to the client computer. Through the hardware interface circuits, the client computer in turn sends the control commands to the corresponding actuators.

Two driving conditions are performed, including the step steering input and double lane change, by assuming that the initial vehicle speed is 72 km/h, and the road adhesion coefficient is 0.6. As illustrated in Figure 7.43 for the double lane change maneuver, the centralized control system using decoupling control method is able to track closely the desired yaw rate generated from the 2-DOF reference model with only a 10.3% amplitude difference. In addition, the peak value of the sideslip angle is restrained at a relatively small value of 0.1 rad, although there is a deviation from the desired sideslip angle. The results indicate that the centralized control system is able to maintain effectively the vehicle trajectory and hence improve its handling stability. Moreover, the small peak value of the roll angle represents a good control performance for the vehicle attitude. A similar pattern can be observed for the step steering input maneuver as shown in Figure 7.44.

7.4   Integrated Control of an Active Suspension System (ASS) and Electric Power Steering System (EPS) using $H_\circ$ Control Method

Numerous external disturbances occur when a vehicle is being driven. Typical disturbances include lateral winds and stochastic excitations from the road surface. Both disturbances affect the vehicle lateral and vertical motions, respectively. On the other hand, the two motions interact with each other and have great effects on both vehicle stability and ride comfort. To suppress the disturbances and hence improve the vehicle overall performance,
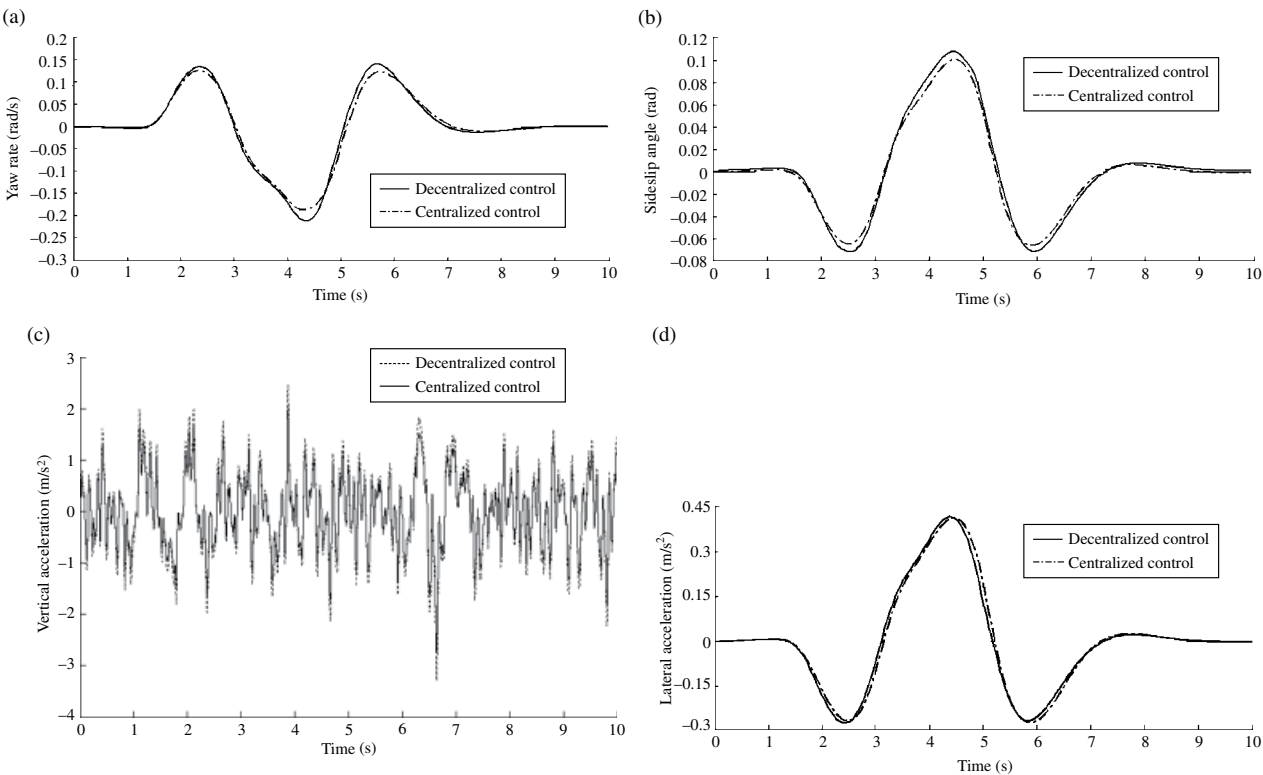
Figure 7.41 Comparison of responses for the double lane change maneuver. (a) Yaw rate. (b) Sideslip angle. (c) Vertical acceleration. (d) Lateral acceleration.
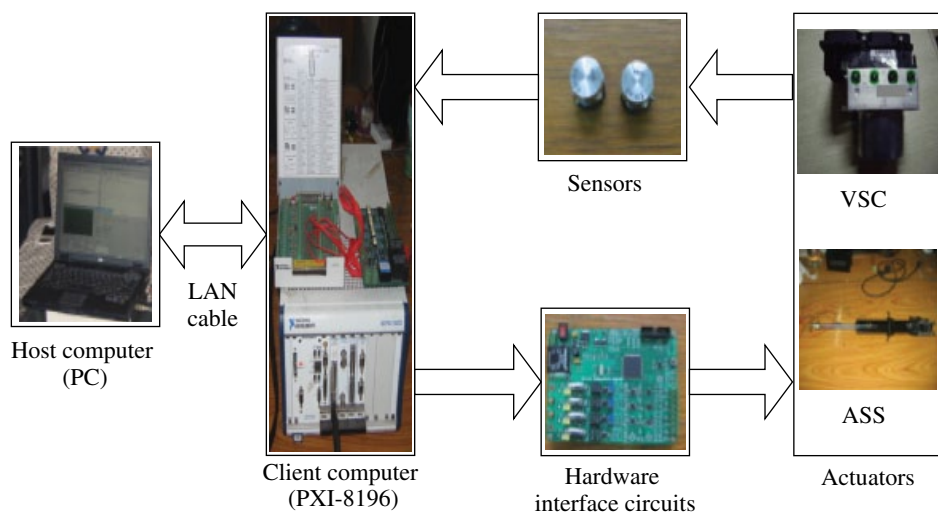
Figure 7.42 Experimental configuration of the developed integrated control system.
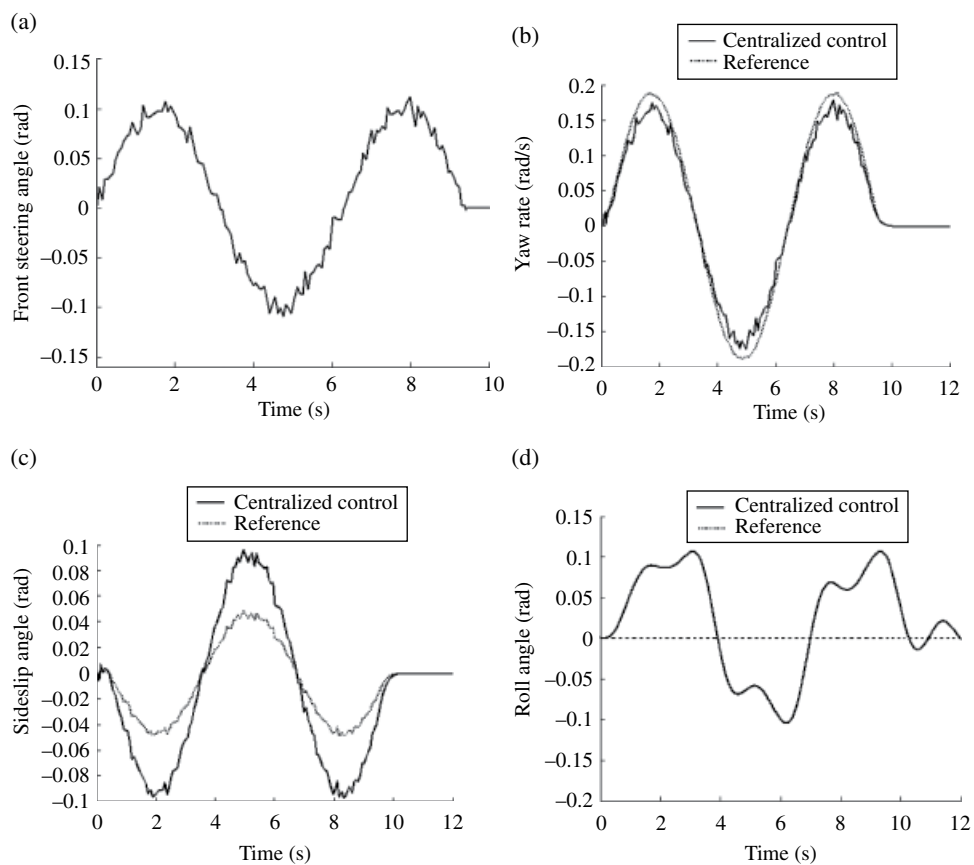
Figure 7.43 Comparison of responses for the double lane change maneuver. (a) Front steering angle. (b) Yaw rate. (c) Sideslip angle. (d) Roll angle.

(a)

(b)

(c)

(d)
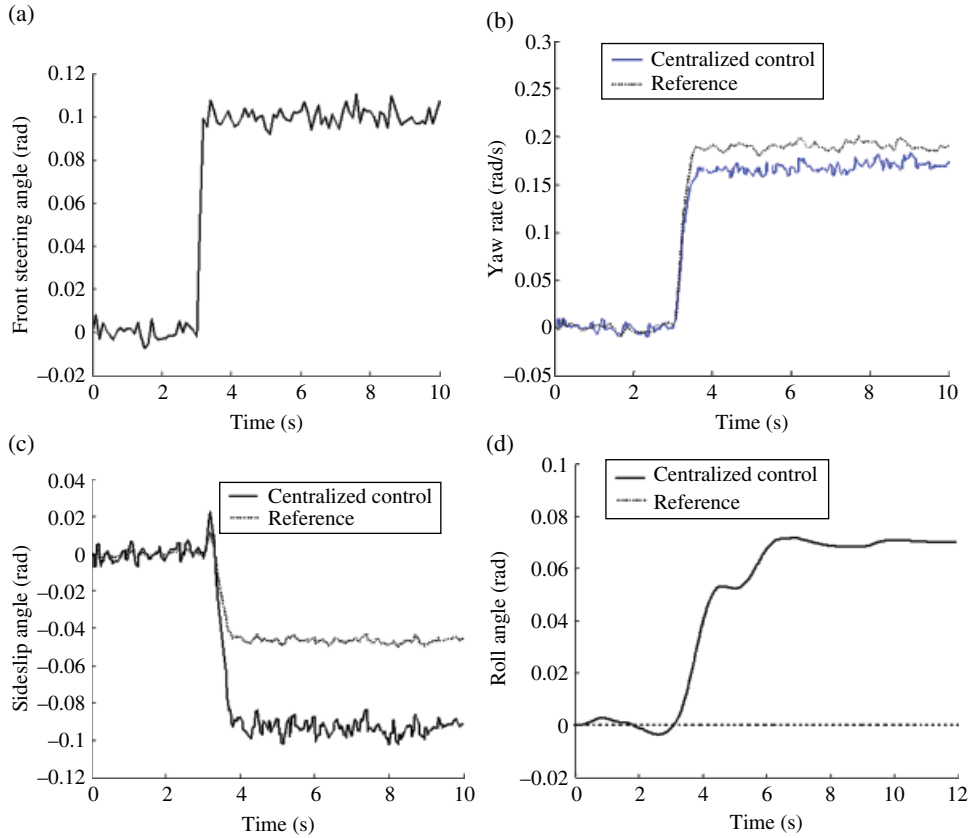
Figure 7.44   Comparison of responses for the step steering input maneuver. (a) Front steering angle. (b) Yaw rate. (c) Sideslip angle. (d) Roll angle.

an integrated control method is applied to achieve the function integration of both the steering and suspension systems through coordinating the interactions between the vehicle lateral and vertical motions[28].

7.4.1   *Vehicle Dynamic Model*

The 7-DOF vehicle dynamic model developed in Section 7.3 is used. The equations of motion are the same as equations (7.44)–(7.49), except that the corrective yaw moment is omitted in equation (7.45).

7.4.2   *EPS Model*

The following governing equations can be obtained by applying a force analysis on the steering gear of the EPS system:

$$T_m + k_n \left(\delta_h - \delta_1 \right) = T_r + J_p \ddot{\delta}_1 + B_p \dot{\delta}_1 \tag{7.69}$$

where T_m is the assist torque applied on the steering column; T_c is the hand torque applied on the steering wheel and $T_c = k_n \left(\delta_h - \delta_1 \right)$; k_n is the torsional stiffness of the torque sensor; δ_h is the rotation angle of the steering wheel; δ_1 is the rotation angle of the pinion, and hence the steering angle of the front wheel δ_f can be calculated as $\delta_f = \delta_1 \big/ G$, and G is the speed reduction ratio of the rack-pinion mechanism; J_p is the equivalent moment of inertia of multiple parts reflected on the pinion axis, including the motor, the gear assist mechanism, and the pinion; B_p is the equivalent damping coefficient reflected on the pinion axis; and T_r is the aligning torque transferred from the tyres to the pinion, $T_r = \dfrac{2}{G} d k_{\alpha F} \left(\dfrac{\delta_1}{G} - \dfrac{l_f}{u_c} r - \beta \right)$, where d is the pneumatic trail of the front tyre. The state variable is defined as:

$$x = \left(z_{uFL} \quad z_{uFR} \quad z_{uRL} \quad z_{uRR} \quad \dot{z}_{uFL} \quad \dot{z}_{uFR} \quad \dot{z}_{uRL} \quad \dot{z}_{uRR} \quad z_c \quad \dot{z}_c \quad \varphi \quad \dot{\varphi} \quad \theta \quad \dot{\theta} \quad r \quad \dot{y}_c \quad \delta_1 \quad \dot{\delta}_1 \right)^T$$

(7.70)

The external disturbances are defined as the stochastic excitation of the road unevenness to each wheel z_{0i}, and the lateral wind disturbance, which is given as:

$$w = \left(z_{0FL} \quad z_{0FR} \quad z_{0RL} \quad z_{0RR} \quad z_w \right)^T$$

(7.71)

The control input U is defined as the four active suspension forces f_i, and the assist torque T_m:

$$U = \left[f_{FL} \quad f_{FR} \quad f_{RL} \quad f_{RR} \quad T_m \right]^T$$

(7.72)

The system state equation is constructed as:

$$\dot{X} = A(X) + B \begin{bmatrix} S_w w \\ U \end{bmatrix}$$

(7.73)

where $A(X)$ is the polynomial column vector of the state variable; $S_w = diag\left(S_{w1}, S_{w2}, S_{w3}, S_{w4}, S_{w5} \right)$ corresponds to the weighting coefficients of the road excitation and lateral wind perturbation, respectively.

The multiple performance indices are selected by considering the vehicle handling stability, ride comfort, and energy consumption of the ASS. They include the yaw rate r, and sideslip angle β, roll angle φ, vehicle vertical acceleration $\ddot{z}_c$, pitch angle θ, assist torque T_m, and control forces f_i of the ASS. Therefore, the system penalty function is proposed as:

$$Z = S_Z \left[r \quad \ddot{z}_c \quad \phi \quad \theta \quad \beta \quad f_{FL} \quad f_{FR} \quad f_{RL} \quad f_{RR} \quad T_m \right]^T$$

(7.74)

where $S_Z = diag\left(S_1, S_2, S_3, S_4, S_5, S_6, S_7, S_8, S_9, S_{10} \right)$ is the weighting coefficient matrix.

The system output is defined as follows by considering the measurability of the signals:

$$Y = \left[\ddot{z}_c \quad r \quad \dot{\phi} \quad \dot{\theta} \quad \dot{y}_c \quad f_d \right]^T$$

(7.75)

Therefore, the state equation and output equation of the nonlinear vehicle dynamic system is obtained as:

$$\begin{cases} \dot{X} = A(X) + B_1 w + B_2 U \\ Z = C_1 X + D_{12} U \\ Y = C_2 X \end{cases} \tag{7.76}$$

where B_1 and B_2 are the input 18×5 matrices; C_1 and C_2 are the output matrices with size of 10×18 and 6×18, respectively; D_{12} is the matrix of size 10×5.

7.4.3 Design of Integrated Control System

As discussed earlier in the chapter, the integrated control of the EPS and ASS is a complex nonlinear control problem since there are uncertainties on the structure and parameters, along with some unmodeled dynamics, etc. In addition, the complexity of the system is further increased by the external disturbances. To overcome the problem, the $H_\circ$ control method is applied to design the complex integrated control system since it has advantages in simultaneously achieving the robust stabilization and performance of the control system. Although $H_\circ$ control is applied to linear systems in general, the same methodology can be used for nonlinear systems. Then, $H_\circ$ control for nonlinear systems becomes a so-called L_2 gain constrained control. Moreover, $H_\circ$ techniques can be used to minimize the closed loop impact of the disturbances. The structure of the proposed integrated control system is shown in Figure 7.45.
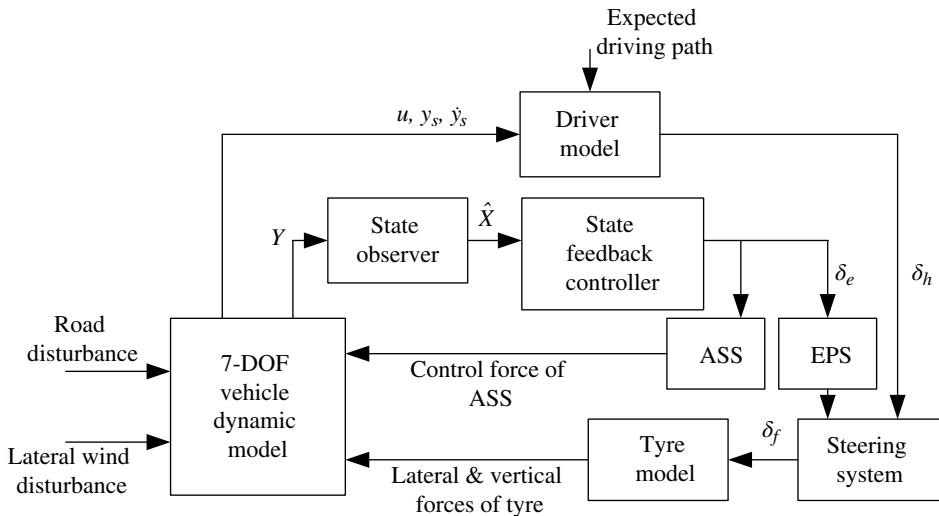

Figure 7.45   Block diagram of the integrated control system of EPS and ASS.

As a matter of fact, not all the signals of the integrated control system can be obtained and, even if they can, the cost of the controller is increased significantly. Therefore, a $H_\circ$ state observer is required to realize the feedback control. The state observer is constructed as follows:

$$\begin{cases} \dot{\hat{X}} = A(\hat{X}) + B_1 w + B_2 U + Q(\hat{X})(Y - \hat{Y}) \\ \hat{Y} = C_2 \hat{X} \end{cases} \tag{7.77}$$

where $\hat{X}$ is the state vector of the observer; $\hat{Y}$ is the observer output; and $Q(\hat{X})$ is the output gain. The aim to solve for the observer is to find the output gain $Q(\hat{X})$ and the detailed solution of the output gain is provided in the reference[15].

7.4.4   Simulation Investigation

To demonstrate the effectiveness of the developed integrated control system, a simulation investigation is performed. The vehicle physical parameters are given in Table 7.5 of Section 7.3.12. After tuning, the matrices of the weighting coefficients are selected as:

$$S_w = \text{diag}(0.03, \ 0.03, 0.03, \ 0.03, 0.002)$$

$$S_Z = \text{diag}(0.5, 0.1, 0.8, 0.8, 0.9, 0.005, 0.005, 0.005, 0.005, 0.01)$$

The vehicle speed is set as $u_c = 25\,m/s$ and the expected input trajectory of the vehicle is illustrated in Figure 7.46. It is observed in the figure that the vehicle travels straight forward first and then around a circle. The stochastic road excitation is applied all the way through, while the lateral wind disturbance is exerted after the vehicle turns and then reaches a steady state condition. In this chapter, it is assumed that the vehicle encounters an abrupt (step) lateral wind disturbance F_w with an amplitude of 1500 N at time $t_2 = 3s$, and disappears at time $t_3 = 4s$. The proposed integrated control system is compared with the two other systems: only with an EPS (named single EPS), only with an ASS (named single ASS). The following observations are made.

As illustrated in Figure 7.47(a, b; see page 248) and Table 7.6, the peak value of the sideslip angle for the integrated control is reduced by 6.06% and 13.89% respectively, compared with that for the single EPS control and single ASS control, after the steering is applied. In addition, the peak value of the sideslip angle for the integrated control is reduced by 28.99% and 14.04% respectively, after the vehicle encounters the lateral wind. The settling time of the sideslip angle for the integrated control is also decreased for both cases. A similar pattern is observed for the yaw rate. The results indicate that the impact of the abrupt lateral wind disturbance on the vehicle is restrained effectively and hence the vehicle handling stability is improved.

It is observed clearly in Figure 7.47(c) and Table 7.7 that the peak value of the steering torque for the integrated control is reduced by 8.78% and 16.18% respectively, compared with that for the single ASS control and single EPS control. In addition, the steady state
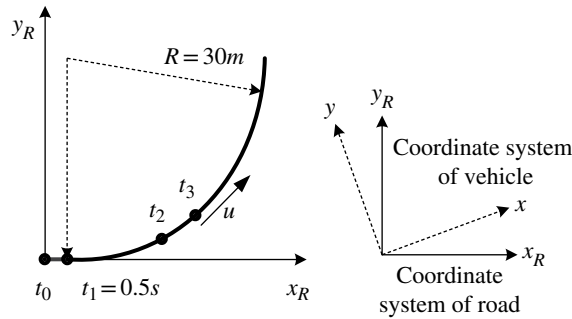
Figure 7.46   Expected vehicle trajectory input.

Table 7.6   Responses for handling stability.

Performance index	Control method	Peak value		Response Time(s)	
		Steering	Lateral Wind	Steering angle	Lateral Wind
Sideslip angle	Single EPS control	–0.033	–0.057	2.022	4.985
β (rad)	Single ASS control	–0.036	–0.069	2.125	5.434
	Integrated system control	–0.031	–0.049	2.018	4.751
Yaw rate r	Single EPS control	0.215	0.342	1.851	4.895
(rad.s^{-1})	Single ASS control	0.238	0.716	1.878	5.284
	Integrated system control	0.212	0.289	1.845	3.826

value of the steering torque for the integrated control is reduced by 13.45% and 14.96% respectively, and the settling time is decreased by 8.22% and 10.32% respectively. The results demonstrate that the integrated control system is able to maintain both steering agility and good road feel, and at the same time effectively restrain the impact of the abrupt lateral wind disturbance on the vehicle.

Figure 7.47(d–h) and Table 7.8 illustrate that these performance indices on ride comfort, including the vehicle vertical acceleration, roll angle, pitch angle and suspension deflection, are reduced for the integrated control, compared with that for the single ASS control and single EPS control. For brevity, the vehicle vertical acceleration is selected to show the improvement of the integrated control system over the other two control systems. As shown in Figure 7.47(d), the PSD (power spectrum density) value of the vehicle vertical acceleration for the integrated control is decreased significantly compared with the single EPS control in the human body-sensitive frequency region of 1–12 Hz. Moreover, it is observed that the PSD value for the integrated control is decreased greatly in the frequency region of 8–12 Hz compared with the single ASS control, although there is no big difference between the two in the frequency region of 1–4 Hz, which is the resonant frequency region of the sprung mass. Therefore, the results indicate that the vehicle ride comfort is improved significantly by the integrated control system compared with both the single EPS and single ASS control systems.

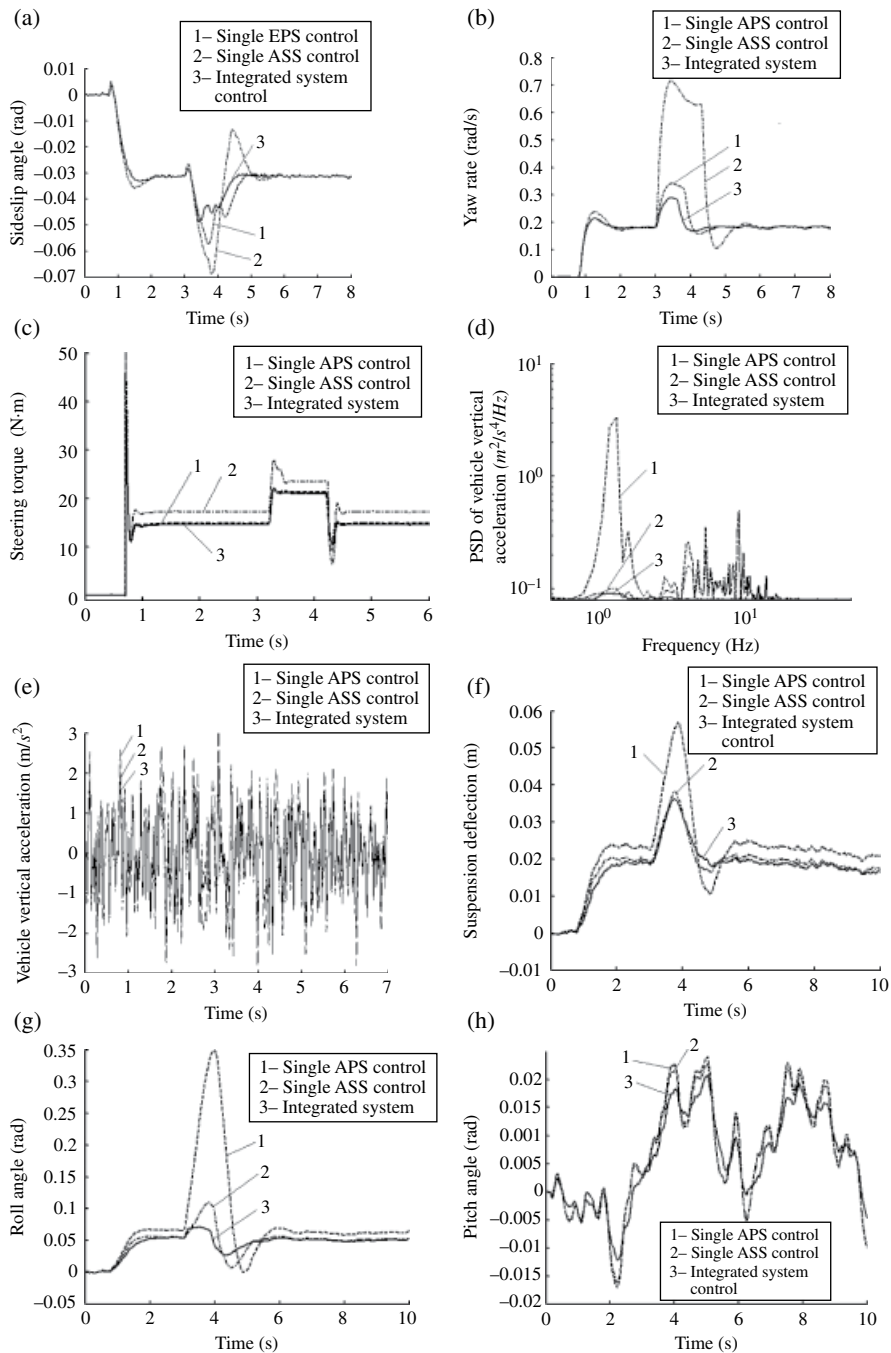**Figure 7.47**   Comparisons of the responses for the three control systems. (a) Sideslip angle. (b) Yaw rate. (c) Steering torque. (d) PSD of vehicle vertical acceleration. (e) Vehicle vertical acceleration. (f) Suspension deflection. (g) Roll angle. (h) Pitch angle.

Table 7.7   Steering torque.

Control Method	Maximum (Nm)		Response Time (s)		Steady State Value (Nm)	
	Steering	Lateral Wind	Steering	Lateral Wind	Steering	Lateral Wind
Single EPS control	45.85	22.17	1.005	3.589	14.93	21.38
Single ASS control	50.26	27.86	1.095	3.455	17.25	23.55
Integrated system control	42.13	21.91	0.982	3.398	14.67	21.11

Table 7.8   Response for ride comfort.

Performance index	Control method	Average	Root mean square
	Single EPS Control	0.0130	0.9115
Acceleration z_c (m.s^{-2})	Single ASS Control	0.0087	0.8273
	Integrated System Control	0.0070	0.7757
	Single EPS Control	0.0923	0.0747
Roll angle ϕ (rad)	Single ASS Control	0.0586	0.0458
	Integrated System Control	0.0521	0.0349
	Single EPS Control	0.0069	0.0097
Pitch angle θ (rad)	Single ASS Control	0.0065	0.0085
	Integrated System Control	0.0061	0.0081
	Single EPS Control	0.0222	0.0115
Suspension deflection f_d (m)	Single ASS Control	0.0189	0.0083
	Integrated System Control	0.0176	0.0076

7.5   Integrated Control of Active Suspension System (ASS) and Electric Power Steering System (EPS) using the Predictive Control Method

Predictive control (or model predictive control (MPC)) theory is an advanced control method developed from an industrial process control used in the 1980s. The principle behind predictive control is to use the past and current system states to predict the future change of the system output. The system's optimal control is achieved by minimizing the error between the controlled variables and the targets by applying an iterative, finite time-horizon optimization approach. The predictive control method is applied to the integrated control of the ASS and EPS systems in this chapter[29] since the predictive control has advantages in dealing with both soft and hard constraints, and uncertainties in a complex multivariable control framework.

7.5.1   Designing a Predictive Control System

As developed in the previous chapter, the same 7-DOF vehicle dynamic model is used. To apply the iterative, finite time-horizon optimization approach, the control system model must be represented by a discrete state equation[29]. The system predictive width is set
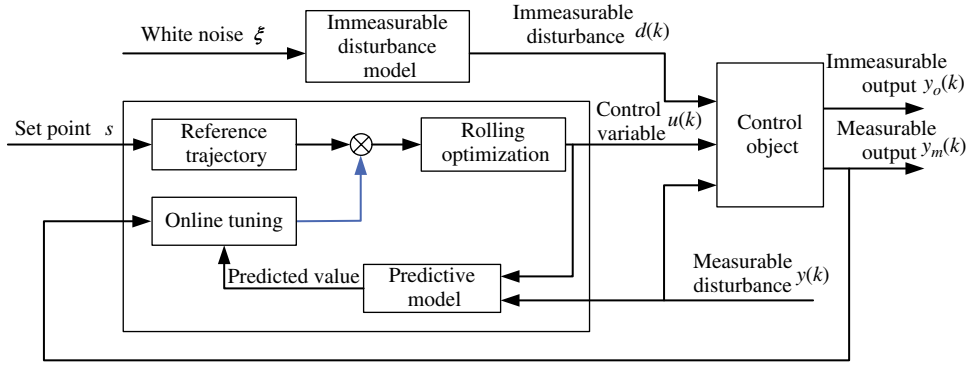
Figure 7.48   Block diagram of the predictive control system.

as P, and the control width C must follow the condition $C'' P$. The optimization objective of the system between the reference trajectory $r(k)$ and the model predictive output $y(k)$ is given in a quadratic form:

$$\min J\left(k\right) = \sum_{i=0}^{p-1}\sum_{j=1}^{n_u}\left\{\left|\boldsymbol{R}_{i,j}^{u}u_j\left(k+i\,|\,k\right)\right|^2 + \left|\boldsymbol{R}_{i,j}^{\Delta u}\Delta u_j\left(k+i\,|\,k\right)\right|^2\right\}$$
$$+ \sum_{i=0}^{P-1}\sum_{j=1}^{n_y}\left|\boldsymbol{Q}_{i+1,j}^{y}\left(y_j\left(k+i+1\big|k\right)-r_j\left(k+i+1\right)\right)\right|^2$$

(7.78)

where R and Q correspond to the weighting matrices of the control variables and output variables, respectively, and $R^u = diag\left(r_{11}, r_{21}, r_{31}, r_{41}, r_{51}\right)$, $R^{\Delta u} = diag\left(r_{12}, r_{22}, \ldots, r_{52}\right)$, $Q = diag\left(q_1, q_2, \ldots, q_{14}\right)$; n_u and n_y are the dimensions of the control variables and output variables; $r_{11}, \ldots, r_{51}$ are the weighting coefficients of the control variables, $r_{12}, \ldots, r_{52}$ are the weighting coefficients of the variation rates of the control variables, $q_1, \supset, q_{14}$ correspond to the weighting coefficients of system outputs; and $y(k+i+1|k)$ are the predicted outputs at time k and step $i+1$.

The predictive control is based on the iterative, finite time-horizon optimization of the system model. At every sample time, the constrained optimization problem defined in equation (7.78) is solved online. Only the first term of the control sequence $u(k)\left(u(k-1)+\Delta u(k)\right)$ is implemented to the control variables, then the system's states are sampled again and the optimization process is repeated starting from the new current states. The prediction horizon keeps being shifted forward, and for this reason MPC is also called receding horizon control. The block diagram of the proposed predictive control system is shown in Figure 7.48[30].

7.5.2   Boundary Conditions

One of the advantages of predictive control is the ability to explicitly handle the boundary conditions of the control variables in a multivariable control framework, and then predict the future output and take the control actions accordingly by applying online the iterative,

finite horizon optimization approach. The major boundary conditions are defined as follows by considering the control requirements of the integrated EPS and ASS control system[31]:

1. The collision between the suspension and the frame/body should be avoided. The dynamic travel of the suspension should be constrained by its mechanical structure:

$$\left| z_{2i} - z_{3i} \right| \le f_{d\max} \quad \left(i = FL, FR, RL, RR \right) \tag{7.79}$$

$z_{2i} - z_{3i}$ is the suspension deflection at each suspension; and $f_{d\max}$ is the maximum dynamic deflection of the suspension. It is usually selected as 7–9 cm for sedans, 5–8 cm for buses, and 6–9 cm for commercial vehicles.

2. Tyre–road contact must be ensured in order to provide enough lateral and longitudinal forces to the vehicle. Hence, the dynamic load of the tyre does not exceed the static load.

$$\left| k_{ti} \left(z_{1i} - z_{2i} \right) \right| \le mg \quad \left(i = FL, FR, RL, RR \right) \tag{7.80}$$

$z_{1i} - z_{2i}$ is the dynamic displacement of each tyre; and k_{ti} is the tyre stiffness.

3. When the vehicle lateral acceleration reaches 0.4 g, the roll angle is selected as 2.5 ~ 4Υ for sedans, and not greater than 6 ~ 7Υ for commercial vehicles.

4. The vehicle lateral acceleration should not exceed 0.6 g, the yaw rate should not exceed 0.6 rad/s, and the pitch rate should not exceed 0.3 rad/s.

5. The active suspension force and the steering torque T_m of the EPS is also constrained:

$$\left| f_i \right| " f_{\max} \tag{7.81}$$

$$\left| T_m \right| " T_{m\max} \tag{7.82}$$

7.5.3 Simulation Investigation

To demonstrate the effectiveness of the developed integrated control system, a simulation investigation is performed. It is assumed that the vehicle speed u_c is 20 m/s; the steering wheel input is a step function with an amplitude of $\pi/2$; the predictive width P selected as 10, and the control width C as 4; and the sampling time is 0.005 s. After tuning, the weighting coefficients are selected as: $q1 = q2 = 10^3$, $q3=100$, $q4=500$, $q5= q6=1$, $q7 = q8 = q9 = q10 = 400$, $q11 = q12 = q13 = q14 = 10^3$, $r11 = r21 = r31 = r41 =10^{-3}$, $r51=10^{-2}$, $r12 = r22 = r32 = r42 = r52=1$. The integrated control is compared with the non-integrated control (i.e., the EPS and ASS subsystem controllers work independently), and the passive system to demonstrate the performance of the integrated control system.

It is observed in Figure 7.49(a–e) that the vehicle multiple performance indices for the integrated controlare reduced to various extents compared with the non-integrated control. The results indicate that the integrated control system based on the proposed predictive control is able to improve the overall vehicle performance, including handling stability and ride comfort, by coordinating the interactions between the ASS and EPS.

In addition, a sensitive study is performed to investigate the influence of the predictive width and control width. Figure 7.50 illustrates that control stability and robustness are
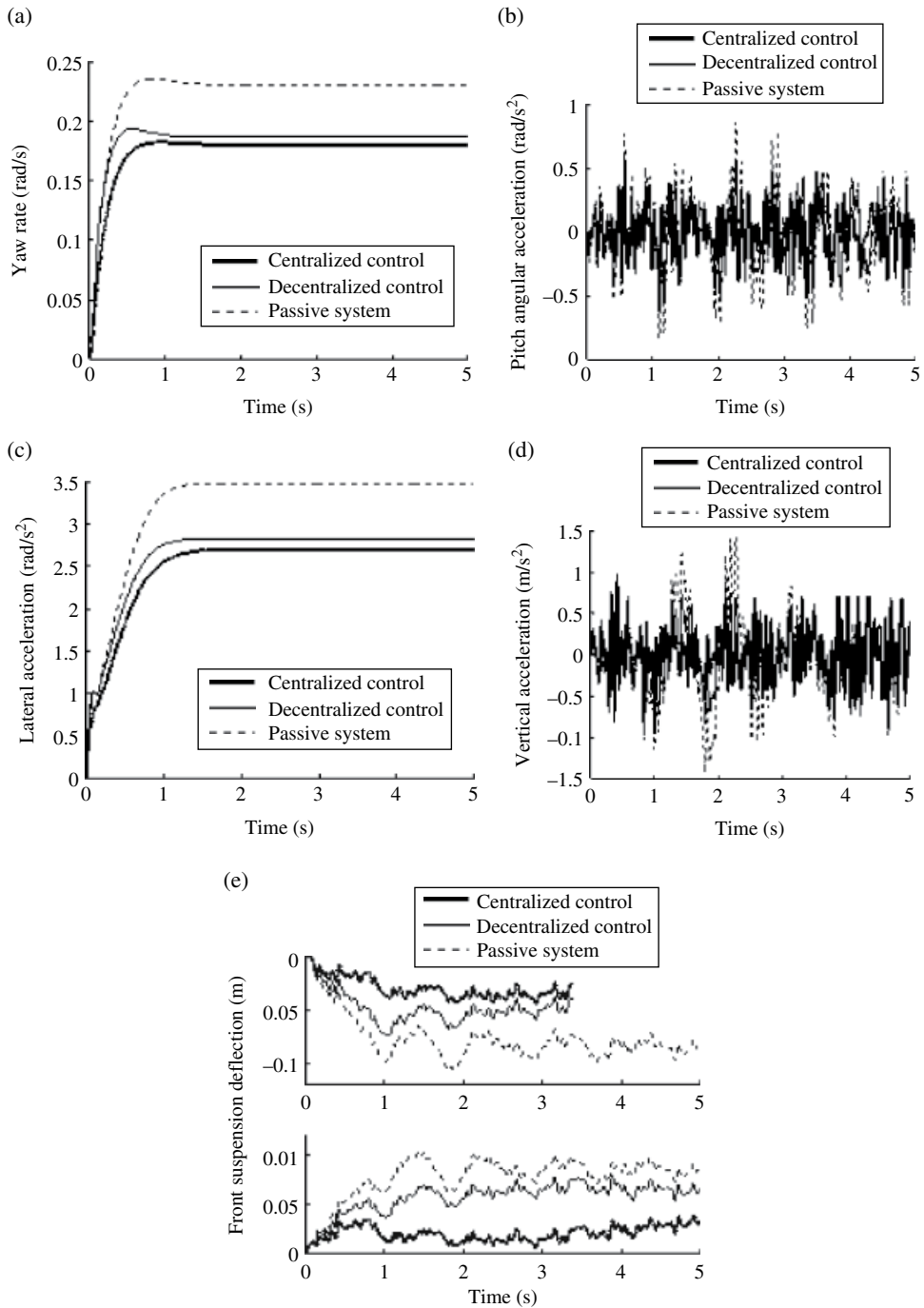
(a)

(b)

(c)

(d)

(e)

Figure 7.49 Comparisons of the responses for the three systems. (a) Yaw rate. (b) Pitch angular acceleration. (c) Lateral acceleration. (d) Vertical acceleration. (e) Dynamic deflection of the front suspension (left and right).
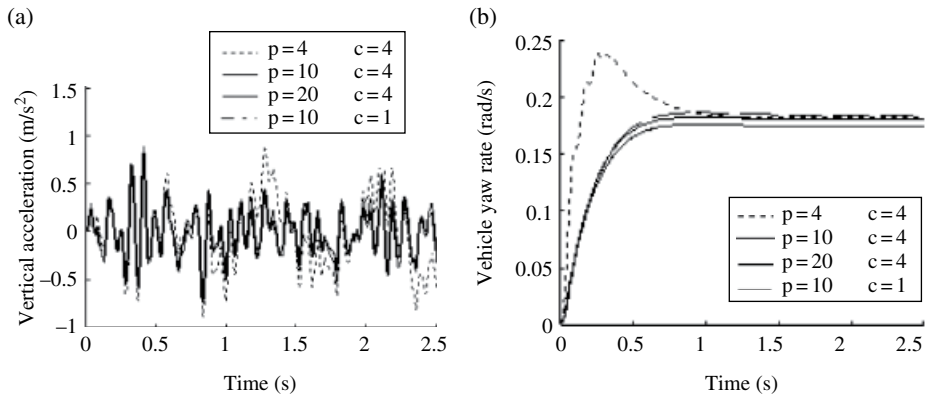
Figure 7.50 Influence of the predictive width and control width. (a) Predictive width variation. (b) Control width variation.

increased as the predictive width P increases, but the dynamic response is slow. Moreover, as the control width C increases, the dynamic response becomes faster, and the control sensitivity is improved correspondingly, but the system stability is reduced.

7.6 Integrated Control of the Active Suspension System (ASS) and Electric Power Steering System (EPS) using a Self-adaptive Control Method

In practice, numerous uncertainties exist in vehicle dynamics models, including stochastic excitations from the road surface, time-varying physical parameters of the vehicle, disturbances of the lateral wind, and measurement noises of on-vehicle sensors. In recent years, self-adaptive control has been identified as an attractive and effective control method to control systems with uncertainties. Self-adaptive control, which has a long history in the field of control engineering, is an advanced control method where the controller is able to adapt to a controlled system with uncertainties. The SISO self-tuning regulator was first proposed in 1973, and then the self-tuning regulator and controller were extended to MIMO in the 1980s. As a result, a number of multivariable self-tuning control methods were developed by combining the recursive parameter estimation method and minimum variance regulation law, generalized minimum variance regulation law, pole placement control law, feed forward control law, and so on. In this chapter, self-adaptive control is applied to the integrated EPS and ASS control by combining the recursive least square estimation method and the generalized minimum variance control law[32,33]. The block diagram of the self-adaptive integrated control system is illustrated in Figure 7.51.

7.6.1 Parameter Estimation of a Multivariable System

The foundation of the self-adaptive control method is parameter estimation. The parameter estimation of the multivariable integrated control system is performed according to the following steps. First, the integrated control system is simplified as a linear multivariable
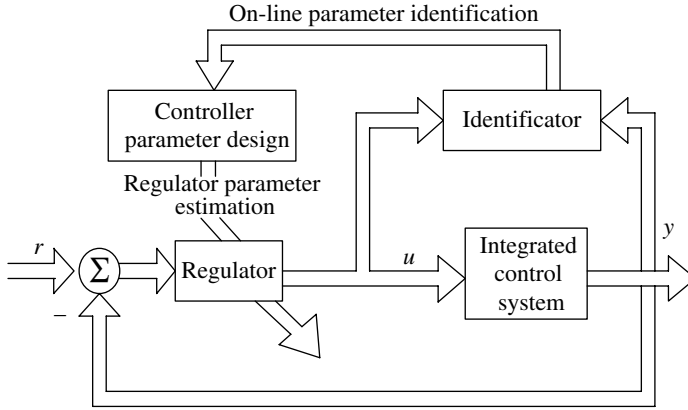
Figure 7.51 Block diagram of the self-adaptive control system for the integrated EPS and ASS control.

system, and the outputs of the two ASS and EPS subsystems are relatively independent. The outputs of the two subsystems have effects on vehicle performance including vertical acceleration, roll angle, yaw rate, etc. Therefore, if the system noise $\xi(t)$ given in equation (7.83) is an irrelevant measured noise with a mean of zero and variance of σ^2, the multivariable integrated control system is considered as a system consisting of m independent SIMO (single input multiple outputs) subsystems[21]. Thereafter, the parameter estimation equation of the multivariable system is decomposed into a set of parameter estimation equations, each of them corresponding to a SIMO subsystem. Finally, the recursive modified least square method is applied to the parameter estimation equations for the multiple SIMO subsystems, and hence the model parameters are obtained.

7.6.2   Design of the Multivariable Generalized Least Square Controller

The ARMAX model of the deterministic linear multivariable system is given as:

$$A\left(z^{-1}\right)\boldsymbol{y}\left(t\right) = B\left(z^{-1}\right)\boldsymbol{u}\left(t\right) + \boldsymbol{d}_a + C\left(z^{-1}\right)\xi\left(t\right) \tag{7.83}$$

where $A\left(z^{-1}\right), B\left(z^{-1}\right)$ and $C\left(z^{-1}\right)$ are the polynomial matrices of the unit backward shift operator z^{-1}; u(t) and y(t) are the input and output vectors with dimension of n; $\boldsymbol{d}_a$ is the steady state error vector with dimension of n; and $\xi(t)$ is the system noise. The generalized output vector is defined as:

$$\varphi\left(t+k\right) = P\left(z^{-1}\right)T\left(z\right)\boldsymbol{y}\left(t\right)$$

And the generalized ideal output vector is defined as:

$$\boldsymbol{y}^*\left(t+k\right) = R\left(z^{-1}\right)p\left(t\right) - Q\left(z^{-1}\right)\boldsymbol{u}\left(t\right) \tag{7.84}$$

where $P\left(z^{-1}\right), Q\left(z^{-1}\right)$, and $R\left(z^{-1}\right)$ are the weighted polynomial matrices of z^{-1}; $T(z)$ is the lower triangle matrix of z; and p(t) is the n-dimensional reference input vector with known boundary.

If the optimal prediction of the generalized output vector $\varphi^*\left(t+k\,|\,t\right)$ equals the generalized ideal output $y^*\left(t+k\right)$, the generalized minimum variance control law is obtained as:

$$\varphi^*\left(t+k\,|\,t\right)=R\left(z^{-1}\right)p\left(t\right)-Q\left(z^{-1}\right)u\left(t\right) \tag{7.85}$$

And the system performance factor J reaches the minimum:

$$J_{\min}=E\left[\left\|e\left(t+k\right)\right\|^2/F_t\right]=E\left[\left\|F\left(z^{-1}\right)\xi\left(t+k\right)\right\|^2/F_t\right]=\gamma^2 \tag{7.86}$$

where F_t denotes the non-descending σ-algebraic group; and $F\left(z^{-1}\right)$ is the polynomial matrix of z^{-1}.

7.6.3 Design of the Multivariable Self-adaptive Integrated Controller

The multivariable self-adaptive integrated controller is designed according to the following steps[34]:

1. Measure the real output y(t) and external input p(t) at time t;
2. Compute $\hat{y}\left(t+k-1\right)$;
3. Construct the vectors $\hat{\phi}\left(t\right)$ and $\hat{\phi}\left(t-k\right)$;
4. Calculate the estimate parameter matrix $\hat{\Theta}\left(t\right)$;
5. Compute the new control input u(t);
6. Go back to step (1), add one to the time counter and repeat the steps above.

7.6.4 Simulation Investigation

To demonstrate the effectiveness of the developed integrated control system, a simulation investigation is performed. The vehicle physical parameters are the same as those defined in Section 7.3.12. The maneuver of step steering input is applied and the vehicle speed u_c is assumed to be 10 m/s and 20 m/s, respectively. The generalized ideal output of the system can be obtained as follows: The roll angle ϕ is expected to be as small as possible, and the yaw rate r is expected to reach an expected steady state value r_d. The self-adaptive integrated control is compared with the single EPS control and the single ASS control to demonstrate the performance of the integrated control system.

It is observed in Tables 7.9 and 7.10 that the self-adaptive integrated control system performs the best among the three control systems on the performance indices of the peak value and settling time of both the vehicle yaw rate and roll angle. The results indicate that both the handling stability and ride comfort are improved through applying the self-adaptive control method to the integrated EPS and ASS control. In addition, the results show that the application of the self-adaptive control method is able to reduce effectively

Table 7.9   Comparison of the peak value of responses.

Performance index	EPS control	ASS control $u_c = 10\,\text{m/s}$	Integrated control	EPS control	ASS control $u_c = 20\,\text{m/s}$	Integrated control
Yaw rate/r (rad·s^{-1})	0.17	0.15	0.12	0.22	0.20	0.18
Roll angle/ϕ (rad)	0.41	0.032	0.029	0.11	0.068	0.016

Table 7.10   Comparison of settling time responses.

Settling time of performance index	EPS control	ASS control $u_c = 10\,\text{m/s}$	Integrated control	EPS control	ASS control $u_c = 20\,\text{m/s}$	Integrated control
Yaw rate (s)	0.43	0.37	0.20	0.9	0.58	0.30
Roll angle (s)	1.7	1.2	1.0	1.6	1.2	1.0

the effects of both the model uncertainties and stochastic disturbances on the system. Moreover, comparisons between the single EPS and ASS demonstrate that the single ASS is able to maintain the vehicle attitude more effectively than the single EPS control under the maneuver of step steering input.

7.7   Integrated Control of an Active Suspension System (ASS) and Electric Power Steering System (EPS) using a Centralized Control Method

This section studies the integrated control of electric power steering system (EPS) and active suspension system (ASS) to achieve the goal of function integration of the control systems[35]. The nonlinear centralized control theory is applied to design a centralized controller in order to solve the system couplings between the ASS and EPS, and eliminate the disturbances from the road excitations. Moreover, a centralized PD controller is designed based on the centralized vehicle dynamic system in order to improve the dynamic responses of steering conditions.

7.7.1   *Centralized Controller Design*

7.7.1.1   **Centralization of System Inertial Term**

This study uses the same models as those developed in Section 7.4, including the nonlinear vehicle dynamic model, EPS system model, and ASS model.

The nonlinear dynamic model is transformed into the affine nonlinear form described in reference[36] through order reduction of the differential equation and centralized of the inertial terms. The state equation of the system is given as:

$$\dot{x} = Ax + Bu + \Delta f(x,t) + Pw \tag{7.87}$$

where $\mathbf{A}_{n \times n}$ $(n = 19)$ is the coefficient matrix; $\mathbf{B}_{n \times m} = [\mathbf{B}_1, \mathbf{B}_2, \mathbf{B}_3, \mathbf{B}_4, \mathbf{B}_5]$ $(m = 5)$ is the input matrix; $\Delta \mathbf{f}(\mathbf{x}, t)$ is the affine nonlinear term of the state variables; and $\mathbf{P}$ is the disturbance coefficient matrix. The output equation is given as

$$y = Cx \tag{7.88}$$

where $C = [C_1, C_2, C_3, C_4, C_5]^T$ is the output coefficient matrix. The control variables include the control forces of the active suspension f_i $(i = 1, 2, 3, 4)$, and the assist torque provided by the motor of the EPS. Therefore, the control input vector is defined as:

$$u = [f_1, f_2, f_3, f_4, T_m]^T \tag{7.89}$$

The multiple vehicle performance indices are considered to evaluate both the vehicle handling stability and ride comfort. These performance indices can be measured by the following physical terms: the vertical acceleration of the sprung mass $\ddot{Z}_c$; the roll angle Φ; the suspension dynamic deflection f_d; the yaw rate r; and the sideslip angle β. Therefore, the output vector is defined as:

$$y = \left[\ddot{Z}_c, \Phi, f_d, r, \beta \right]^T \tag{7.90}$$

For the above system with the same number of input variables and output variables, the static state feedback decouple method is used. For brevity, the detailed derivations of the matrices $A_{19 \times 19}$, $B_{19 \times 5}$, $P_{19 \times 5}$, $C_{5 \times 19}$, $D_{5 \times 5}$, x and the affine nonlinear term $\Delta f(x, t)$ are not presented here.

7.7.1.2 Centralized System

Let $\phi_j^i(x) = L_f^{j-1} h_i(x)$. It can be proven that the other $19 - \sum r_i = 6$ transformations can be found to construct the following mapping:

$$\Phi = col\left(\varphi_1^1, \ldots, \varphi_{r_5}^3, \varphi_{14}, \ldots, \varphi_{19} \right)$$

where r_i $(i = 1, 2, 3, 4, 5)$ is the relative degree of the system; $L_f \lambda(x)$ is a scalar function; $f(x)$ and $\lambda(x)$ are the functions of x. Please refer to Section 7.3 or reference[36] for the definitions of these functions. Thus, the transformation of the local coordinates at $x = 0$ is constructed as:

$$z(x) = \left[z_1(x) \ z_2(x) \ \cdots \ z_{11}(x) \right]^T$$

The defined system output is the last row of the first five sub-matrix. It is given as:

$$\dot{z}_i(x) = \begin{bmatrix} 0 & 1 & \cdots & 0 & 0 \\ 0 & 0 & 1 & \cdots & 0 \\ & & & 1 & \\ & & & & 1 \\ 0 & 0 & \cdots & & 0 \end{bmatrix}_{r_i} z_i(x) + \begin{bmatrix} 0 \\ 0 \\ 0 \\ 0 \\ b_i(x) \end{bmatrix} + \begin{bmatrix} 0 \\ 0 \\ 0 \\ 0 \\ E_i(x)\mathbf{u} \end{bmatrix} + \begin{bmatrix} 0 \\ 0 \\ 0 \\ 0 \\ P_i\mathbf{w} \end{bmatrix}$$

$$z_i(x) = \begin{bmatrix} z_{i1}(x) & \cdots & z_{ir_i}(x) \end{bmatrix}^T \tag{7.91}$$

Combining this with the feedback control law u, the subsystem is given as:

$$\begin{aligned} \dot{z}_{ij} &= z_{i(j+1)}, i \le 5, j \le r_i - 1 \\ \dot{z}_{ir_i} &= b_i(x) + E_i(x)u + p(x)w \end{aligned} \tag{7.92}$$

Therefore, the matrix constructed by $\dot{Z}_{ir_i}$ is expressed as:

$$\begin{aligned} \begin{bmatrix} \dot{z}_{1r_1} & \dot{z}_{2r_2} & \dot{z}_{3r_3} & \dot{z}_{4r_4} & \dot{z}_{5r_5} \end{bmatrix}^T &= b(\mathbf{x}) + E(\mathbf{x})u + p(\mathbf{x})w \\ &= b(\mathbf{x}) + E(\mathbf{x})\begin{bmatrix} E^{-1}(\mathbf{x})b(\mathbf{x}) + E^{-1}(\mathbf{x})v \end{bmatrix} + p(\mathbf{x})w = v + p(\mathbf{x})w \end{aligned}$$

i.e.

$$\dot{z}_{ir_i} = v_i + \sum_{j=1}^{4} p_{ij} w_j \tag{7.93}$$

and the system output $y_i = z_{i1}$. Therefore, the centralized of the control channels is fulfilled since every control signal v_i only controls the system output $y_i (i \le 5)$ through a series of integrators with an order of r_i. However, it should be noted that the system output y_i is not only affected by v_i, but also by the road excitations. In fact, the control signal v_i does not have any physical meaning, in contrast to the feedback control law u as defined in equation (7.89).

Based on the centralized control theory, the system should be separated into the subsystems with independent control channels to derive the feedback control law. Therefore, the relative degree of the affine nonlinear system is needed. Then, the system can be transformed into a serial structure that consists of a number of subsystems with the degree of $r_i - 1$ and the integrators. Refer to Section 7.3 or reference[35] for the detailed derivation of the relative degree, the design of the input–output centralized controller, and the design of the disturbance centralized controller.

7.7.1.3   Centralized PD Controller Design

The control channels become independent and the disturbance from the road excitations are subdued after the system is centralized. However, the response quality of system is not improved significantly since the control signal v_i is not tuned. The response quality of the system includes the settling time, overshoot, and response error. To further improve the response quality of the system, a PD control law is introduced, and the control signal v_i becomes:

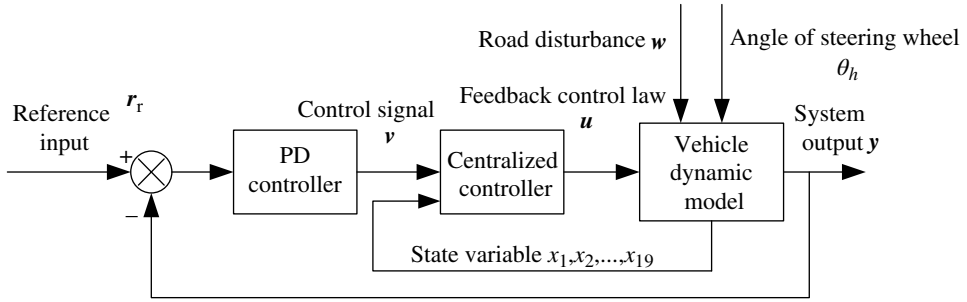$$v = K_p diag(e) + K_d diag(de) \tag{7.94}$$

Figure 7.52 Block diagram of the centralized PD control system.

where e and de are the error of the output signal and the difference of the error, respectively; K_p and K_d are the vector of the proportional coefficient and differential coefficient, respectively.

Finally, the block diagram of the centralized PD control system is shown in Figure 7.52. In the figure, the reference input for the system is defined as:

$$r_r = \{0, 0.071, 0.0302, 0.1135, -0.0222\}$$

The above steady-state parameters are calculated by using equation (7.90) when the step steering is selected as the steering wheel input.

7.7.2 Simulation Investigation

A simulation investigation is performed to demonstrate the performance of the proposed centralized PD control system. We assume that the vehicle travels at a constant speed $u_c = 20\,\text{m/s}$, and the step steering input $\theta_h = 90°$. A filtered white noise signal[37] is selected as the road excitation to the vehicle. The vector of proportional coefficient and differential coefficient is selected as $K_p = [1.8, 1.3, 1.8, 1.7, 1.5]$ and $K_d = [1.3, 2.5, 0.4, 4, 3]$. For comparison, two simulation studies are performed. The first is to compare to the system using the PD control and centralized control, and the other is to compare to the non-integrated systems, i.e., the ASS-only system and EPS-only system. The following discussions are made from the simulation results shown in Figures 7.53–7.59 and Table 7.11:

1. It is clearly observed from Figure 7.53 and Figure 7.54 that both the vertical acceleration of the sprung mass and the dynamic deflection of the front-right suspension for the proposed centralized PD control system are greatly reduced compared to that for both the PD control system and the centralized control system. It can be obtained through a quantitative analysis on the simulation results that the percentage decrease of the vertical acceleration of the spring mass is 65.1 and 27.6, and of the dynamic deflection is 44.2 and 30.8. It should be noted that the dynamic deflection of the front-right suspension is taken as an example since similar patterns can be observed for the other three
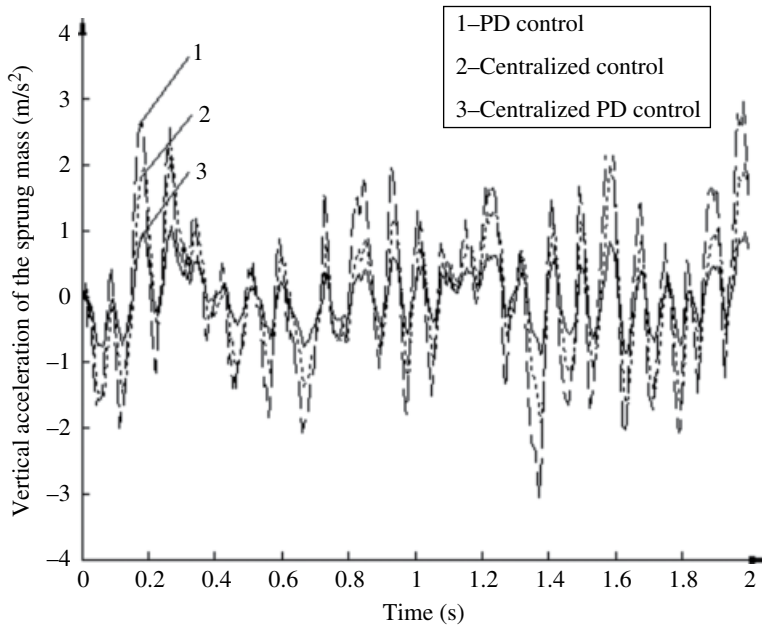
Figure 7.53   Vertical acceleration of the sprung mass (Front-right suspension).
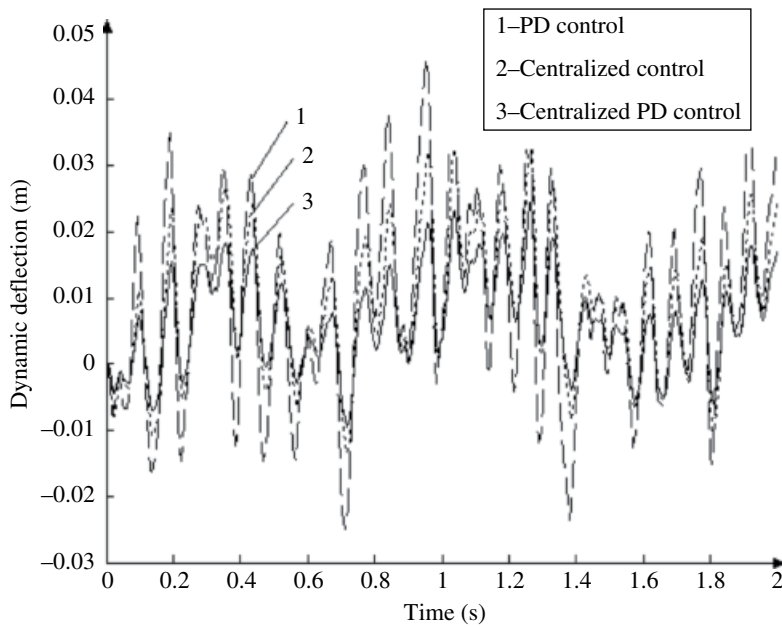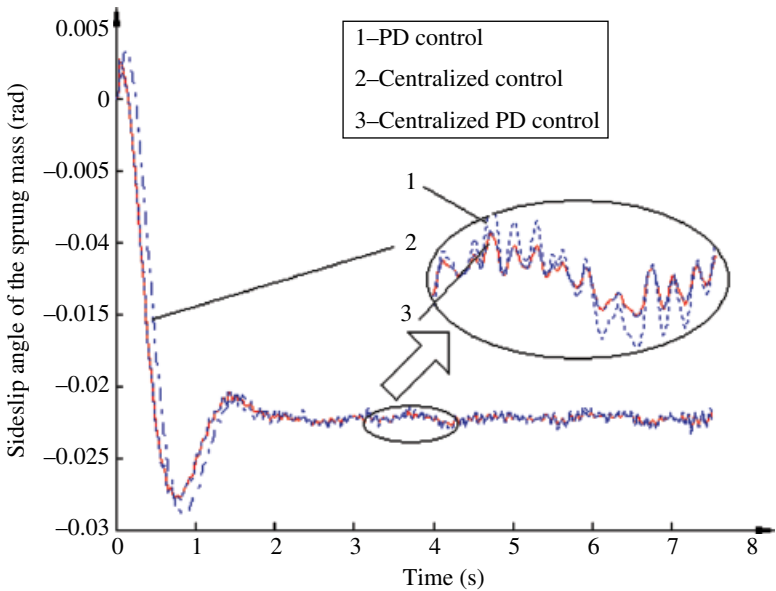

Figure 7.54   Dynamic deflection.

Figure 7.55 Sideslip angle of the sprung mass.
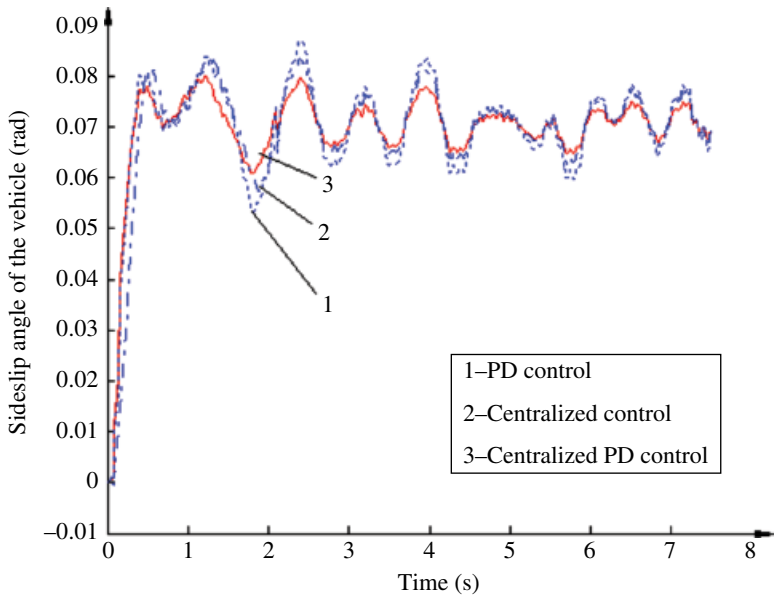
Figure 7.56 Sideslip angle of the vehicle.
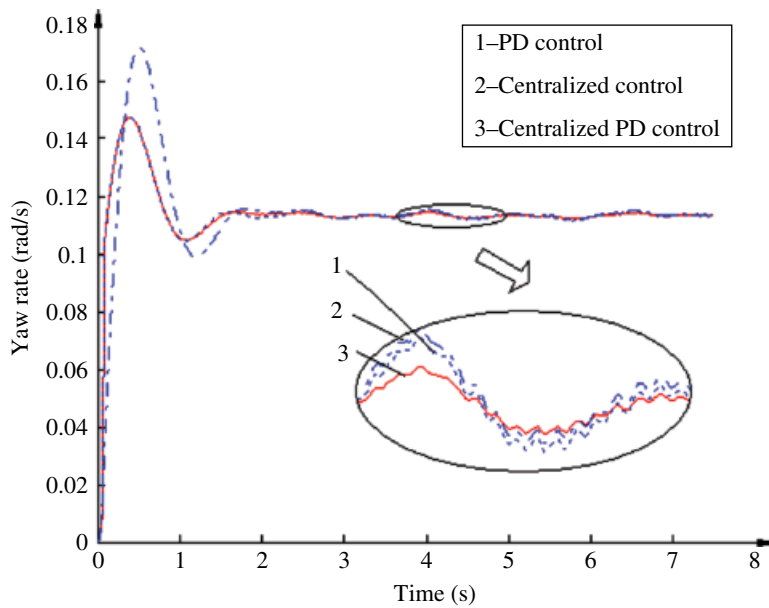
Figure 7.57   Yaw rate.
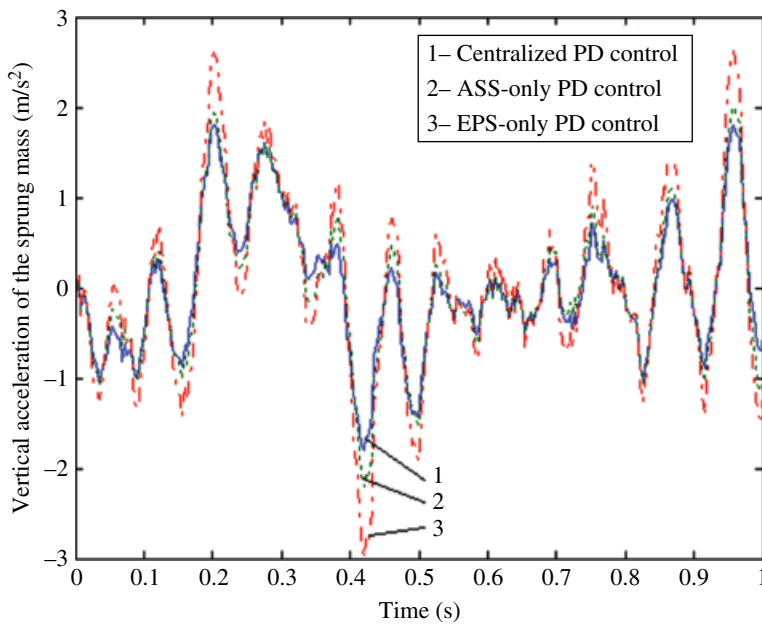
Figure 7.58   Vertical acceleration of the sprung mass.
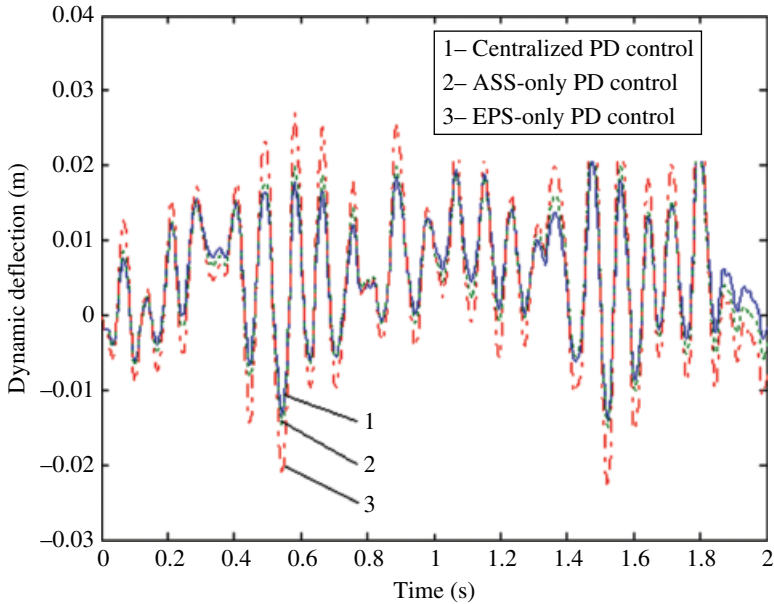
Figure 7.59 Dynamic deflection.

Table 7.11 Simulation results.

Control method		Peak value of response	Overshoot %	Response time (s)
Sideslip angle of vehicle	PD control	0.1446	27.36	0.783
	Centralized control	0.1484	30.76	0.834
	Centralized PD control	0.1421	25.18	0.745
Sideslip angle of sprung mass	PD control	0.0800	12.68	0.436
	Centralized control	0.0082	15.49	0.482
	Centralized PD control	0.0078	9.86	0.412
Yaw rate	PD control	−0.0286	28.63	0.423
	Centralized control	−0.0338	52.42	0.482
	Centralized PD control	−0.0282	26.87	0.423

suspensions. The results indicate that vehicle ride comfort is improved significantly by the proposed centralized PD control system in comparison with the other two control systems since the proposed control system integrates the advantages of the PD control and centralized control to eliminate effectively the disturbance from the road excitation.

2. The performance indices on lateral stability are also shown in Figures 7.55–7.57 and Table 7.11. Compared to both the PD control system and the centralized control system, the sideslip angle of the sprung mass, the sideslip angle of the vehicle, and the yaw rate

are reduced by the proposed centralized PD control system. The results indicate that lateral stability is improved by the proposed centralized PD control system.

3. It is observed clearly from Figure 7.58 and Figure 7.59 that both the vertical acceleration of the sprung mass and the dynamic deflection of the suspension for the proposed centralized PD control system are reduced significantly compared to that for both the ASS-only PD control system and the EPS-only PD control system. The results indicate that vehicle ride comfort is improved by the proposed centralized PD control system since the proposed control system is able to coordinate the EPS and ASS to achieve integration between the two systems.

7.8   Integrated Control of the Electric Power Steering System (EPS) and Vehicle Stability Control (VSC) System

This section studies the integrated control of the electric power steering system (EPS) and the vehicle stability control (VSC) system to achieve the goal of integrating the two control systems. The aim of the study is to design a new control strategy to compensate the return torque of the EPS system by considering the interactions of the VSC system under critical driving conditions.

7.8.1   Interactions Between EPS and VSC

The interactions between the EPS and VSC arise from the lateral forces of the tyres provided by the road surface. When we design the EPS separately, i.e., without taking into account the interactions of the VSC, the assist torque is determined mainly through calculating the return torque of the two front tyres. However, when the vehicle is under critical driving conditions, the lateral forces between the tyres and the road reach saturation, and the VSC intervenes to change the longitudinal forces of the tyres and thus change the lateral forces of the tyres. This results in the change of the return torque from the tyres. Therefore, it is necessary to design a new control strategy to compensate for the return torque by considering the intervention of the VSC.

7.8.2   Control System Design

The block diagram of the integrated control system is shown in Figure 7.60. The work principle of the proposed integrated control system is described as follows: in the VSC control unit, the reference inputs for the vehicle dynamic system, including the expected longitudinal speed of the vehicle u_d, expected lateral speed v_d, and expected yaw rate r_d, are calculated from the vehicle 2-DOF reference model. Then, a nonlinear sliding mode controller is used to calculate the expected control force F_{ud} in order to track the desired vehicle motions. The expected control force $F_{ud} = \begin{pmatrix} F_{xd} & F_{yd} & M_{zd} \end{pmatrix}^T$ is defined as a vector of the expected forces for vehicle stability control, where F_{xd}, F_{yd}, M_{zd} is the expected longitudinal force, expected lateral force, and expected yaw moment,
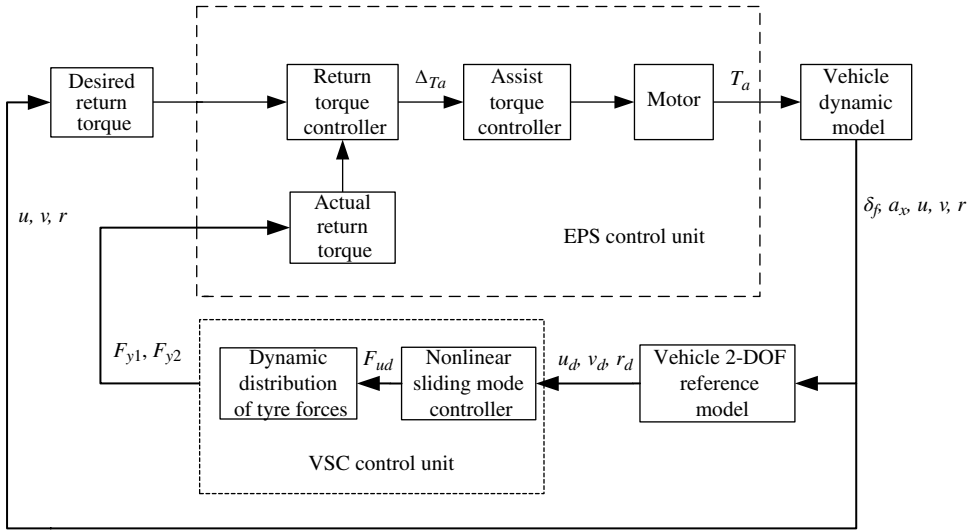
Figure 7.60 Block diagram of the integrated control system.

respectively. Thereafter, the expected control force F_{ud} is distributed optimally to the four wheels. The actual return torque is then generated based on the lateral forces of the two front wheels. In the EPS control unit, the compensated assist torque is obtained by comparing the desired return torque with the actual return torque in the return torque controller. The assist torque T_a is finally calculated by the assist torque controller. Therefore, the lateral stability of the vehicle is improved by compensating the return torque and considering the intervention of the VSC under critical driving conditions.

7.8.3 Dynamic Distribution of Tyre Forces

As mentioned above, the expected control force F_{ud} must be distributed optimally to the four wheels. The distribution of the tyre forces is a multivariable constrained optimization problem, subjected to the distribution accuracy among the four wheels and the control energy. A dynamic distribution method is applied to the distribution of the tyre forces according to the error between the actual value and the expected value of the yaw moment[38].

The compositions of the longitudinal and lateral forces and the yaw moment should have certain limits since the tyre–road friction forces cannot exceed the adhesion limits. Moreover, the feasible regions for the composition of forces and yaw moment are not rectangles since the longitudinal and lateral forces are coupled. When the composition of the longitudinal forces is determined, the yaw moment varies with the different distributions of the longitudinal forces of the four wheels. If all the possible distributions of the longitudinal forces are defined as a set, the yaw moment can be defined as a function of the set. The values of such a function can be constructed into a set with certain limits. When the

composition of the longitudinal forces is determined, the upper limit of the functional set can be obtained. Therefore, a curve can be determined to describe the relation that the upper limits of the functional set vary with the different compositions of the longitudinal forces. The curve is defined as the feasible region of the composition of the longitudinal forces and the yaw moment. When the vehicle drives at high speeds, the steering angles of the front wheels are small and hence can be ignored. Thus, the compositions of forces and yaw moment are obtained as follows:

$$\begin{cases} F_x = F_{x1} + F_{x2} + F_{x3} + F_{x4} \\ F_y = F_{y1} + F_{y2} + F_{y3} + F_{y4} \\ M_z = d_F \left(F_{x2} - F_{x1} \right) + d_R \left(F_{x4} - F_{x3} \right) + a \left(F_{y1} + F_{y2} \right) - b \left(F_{y3} + F_{y4} \right) \end{cases} \tag{7.95}$$

where the subscripts 1 through 4 represent the left-front, right-front, left-rear, and left-front wheels, respectively; d_F, d_R represent half of the front and rear wheel track, respectively; a, b represent the distance of the front axle and rear axle between the C.G., respectively; F_x, F_y, and M_z represent the compositions of the longitudinal and lateral forces, and the yaw moment, respectively.

The distributions of the compositions of forces and the yaw moment are given as follows. First, the composition of the longitudinal forces is distributed. The error of the yaw moment is defined as:

$$e_M = M_{zd} - M_z = M_{zd} - I_z \dot{r} \tag{7.96}$$

The additional yaw moment resulting from the longitudinal forces is obtained from equation (7.95),

$$M_x = d_F \left(F_{x2} - F_{x1} \right) + d_R \left(F_{x4} - F_{x3} \right) \tag{7.97}$$

Let the additional yaw moment be:

$$M_x = k_1 e_M \tag{7.98}$$

Therefore, the error of the yaw moment e_M can be compensated by the additional yaw moment by selecting a suitable coefficient k_1. A constrained quadratic programming problem is defined as follows:

$$\begin{cases} \min_{F_{xi}} \quad J = \dfrac{F_{x1}^{\,2}}{a_{x1}^{\,2}} + \dfrac{F_{x2}^{\,2}}{a_{x2}^{\,2}} + \dfrac{F_{x3}^{\,2}}{a_{x3}^{\,2}} + \dfrac{F_{x4}^{\,2}}{a_{x4}^{\,2}} \\ s.t. \quad M_x = k_1 e_M \\ \qquad F_x = k_2 F_{x1} + k_3 F_{x2} + k_4 F_{x3} + k_5 F_{x4} \\ \qquad\quad k_2 + k_3 + k_4 + k_5 = 1 \end{cases} \tag{7.99}$$

where $a_{xi}(i=1,2,3,4)$ are the maximum tyre road friction forces; $a_{xi} = \mu F_{zi}$, where F_{zi} is the vertical load of the tyre; and k_2, k_3, k_4, k_5 are the function distribution coefficients for the longitudinal forces. However, the above equation cannot compensate accurately for the error of the yaw moment since the longitudinal and lateral forces of the front wheels are coupled. Hence, it is necessary to adjust the lateral forces of the front wheels to further improve the track error of the yaw moment.

It can be observed that the additional yaw moment resulting from the lateral forces of the two front wheels is actually related to the composition of the two forces. Therefore, let the composition of the two forces be $F_{yF} = F_{y1} + F_{y2}$, and F_{yF} at the k-th sampling time is given as:

$$F_{yF}(k) = F_{yF}(k-1) + k_6 e_M \qquad (7.100)$$

where k_6 is a constant. Finally, the lateral force of each front tyre is determined according to its proportion of the vertical load:

$$F_{yi} = \frac{F_{zi}}{F_{z1} + F_{z2}} F_{yF} \quad i = 1,2 \qquad (7.101)$$

7.8.4 Design of a Self-aligning Torque Controller

In order to design a self-aligning torque controller, an analysis of the relationship between the vehicle self-aligning torque and sideslip angle is performed. Figure 7.61 shows the relationship for the 7-DOF vehicle dynamic model by assuming that the vehicle speed is a constant of 72 km/h and the road adhesion coefficient is 0.3. It is observed in Figure 7.61 that the self-aligning torque is approximately proportional to the sideslip angle when the sideslip angle is small, and it reaches the maximum when the sideslip angle is around 4°–6°. As the sideslip angle keeps increasing, the self-aligning torque is decreased instead.
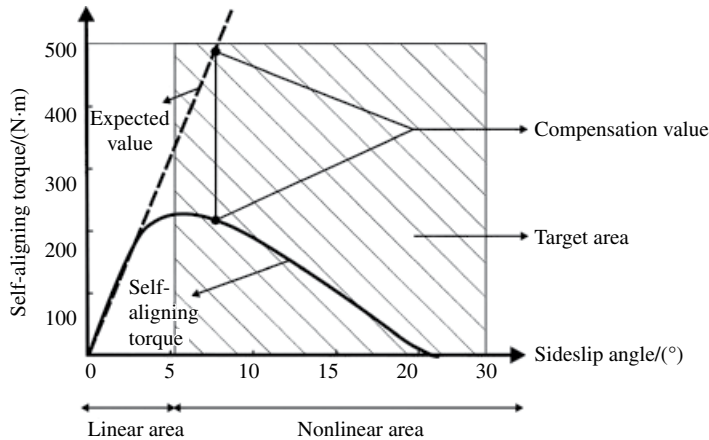

Figure 7.61 Relationship between self-aligning torque and sideslip angle.
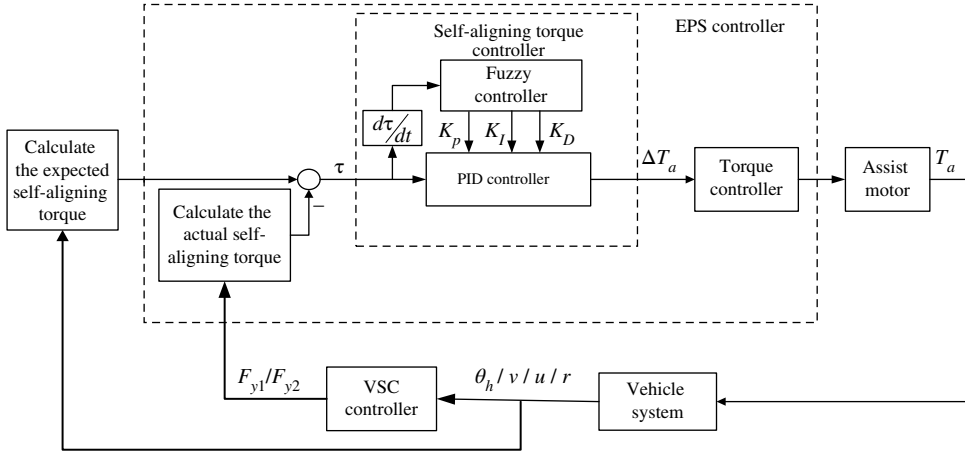
Figure 7.62   Control system chart of the self-aligning torque.

Under this circumstance, the hand torque required by the vehicle driver is increased, and also the road feel is lost. Therefore, the compensation of the self-aligning torque is required through adjusting the EPS based on the vehicle states obtained from VSC system.

The compensation value of the self-aligning torque for the EPS varies with the lateral force. The reason is that the self-aligning torque varies with respect to the sideslip angle. Moreover, the lateral forces also change when the VSC intervenes. Therefore, the PID fuzzy control is used to regulate the compensation value of the self-aligning torque in real time to track the expected value in order to design an appropriate self-aligning torque controller. As shown in Figure 7.62, the fuzzy controller has two input variables: the tracking error of the self-aligning torque τ, and the difference of the error $\dot{\tau}$. The three tuning parameters K_P, K_I, and K_D are selected as the outputs of the fuzzy controller, and they are the inputs of the PID controller. The application of the PID controller is to guarantee that the actual self-aligning torque tracks the expected one in real time.

The actual self-aligning torque is calculated as:

$$M = M_1 + M_2 = F_{y1}e_1 + F_{y2}e_2 \tag{7.102}$$

where M_1, M_2 are the self-aligning torques of the vehicle front-left and front-right wheels, respectively; and e_1, e_2 are the pneumatic trails of the two front tyres, respectively. The expected self-aligning torque is derived as:

$$M_c = \left(\frac{\partial M_z}{\partial \alpha} \right) \times \alpha_i \tag{7.103}$$

where M_c is the expected self-aligning torque; $\dfrac{\partial M_z}{\partial \alpha}$ is the slope rate of the self-aligning torque with respect to the sideslip angle when the linear relationship between them holds; and α_i is the actual sideslip angle of the two front wheels. The rule bases of the fuzzy

controller are developed for the three output variables K_P, K_I, and K_D with respect to the input variable τ and its difference $\dot{\tau}$ as follows:

1. For a relatively large τ, a relatively larger K_P is selected to eliminate deviations and increase the response speed as soon as possible. In the meantime, K_I is set as zero to avoid large overshoots.
2. For a relatively small τ, K_P must be reduced and K_I should be a relatively small value to continue to reduce the deviations and also to prevent large overshoots and oscillations.
3. For an extremely small τ, K_P should keep decreasing and K_I should remain constant or increase a little to eliminate steady errors, and overcome the overshoots and stabilize the system as soon as possible.
4. When the signs of τ and $\dot{\tau}$ are the same, it means that the controlled variables vary away from the target values. Therefore, when the controlled variables approach the target values, the proportional parameter with the opposite sign counteracts the effects of the integral parameter to avoid the overshoots and the subsequent oscillations resulted from the integral parameter. While the control variables are far from the target values and vary towards them, the control process slows down due to the opposite signs of τ and $\dot{\tau}$. Therefore, when τ is relatively large and the signs of $\dot{\tau}$ and τ are opposite, K_I is selected to be zero or negative to accelerate the control process.
5. The value of $\dot{\tau}$ shows the change rate of the tracking error. As $\dot{\tau}$ becomes larger, K_P should become smaller and K_I larger, and vice versa. At the same time, the value of τ should also be taken into consideration.
6. The differential parameter K_D is used to improve the system dynamic characteristics and prevent the variation of τ. The differential parameter K_D is beneficial to reduce overshoots, eliminate oscillations, and shorten the settling time. Therefore, K_D should be increased to reduce the system steady state error and hence improve the control accuracy. When τ is relatively large, K_D is selected to be zero, and the controller becomes a PI controller; when τ is relatively small, K_D is selected to be medium, resulting in a PID control.

To design the fuzzy controller, τ and $\dot{\tau}$ are selected as the input language variables, the fuzzy subset of each variable is set as {Negative Big, Negative Medium, Negative Small, Zero, Positive Small, Positive Medium, Positive Large}, which is denoted as{NB,NM,NS,ZO,PS,PM,PB}. The discourse domains of both τ and $\dot{\tau}$ are defined as $\{-3,-2,-1,0,1,2,3\}$. The triangular full overlap function is adopted as the membership function, and the Sum-Product rule is used for fuzzy inference. The membership function of each rule is denoted as $w_j(\tau, \dot{\tau})(j = 1, 2, \ldots, 7)$. Therefore, the three output variables are obtained by the weighted mean method:

$$K_P = \frac{\sum_{j=1}^{7} w_j\left[(\tau, \dot{\tau}) \times K_{Pj}\right]}{\sum_{j=1}^{7} w_j(\tau, \dot{\tau})} \qquad K_I = \frac{\sum_{j=1}^{7} w_j\left[(\tau, \dot{\tau}) \times K_{Ij}\right]}{\sum_{j=1}^{7} w_j(\tau, \dot{\tau})} \qquad K_D = \frac{\sum_{j=1}^{7} w_j\left[(\tau, \dot{\tau}) \times K_{Dj}\right]}{\sum_{j=1}^{7} w_j(\tau, \dot{\tau})}$$

$$(7.104)$$

where K_{Pj}, K_{Ij}, and K_{Dj} are the weighed parameters of K_P, K_I, and K_D under different conditions. Therefore, the output of the fuzzy PID controller, i.e., the compensation of the self-aligning torque, is obtained as:

$$\Delta T_a = K_p \left(M - M_c \right) + K_I \int (M - M_c) dt + K_D \left(\dot{M} - \dot{M}_c \right) \tag{7.105}$$

7.8.5 Simulation Investigation

To validate the effectiveness of the compensation strategy of the self-aligning torque, a simulation is performed by comparing the integrated control of the VSC and EPS with the non-VSC control, and VSC control. The vehicle initial speed is set as 72 km/h, and a low road adhesion coefficient of 0.3 is selected. Two driving conditions are performed, including the step steering input and single lane change.

It is observed in Figures 7.63 and 7.64 that the integrated control system of VSC and EPS performed the best amongst the three systems considered on both the yaw rate and the
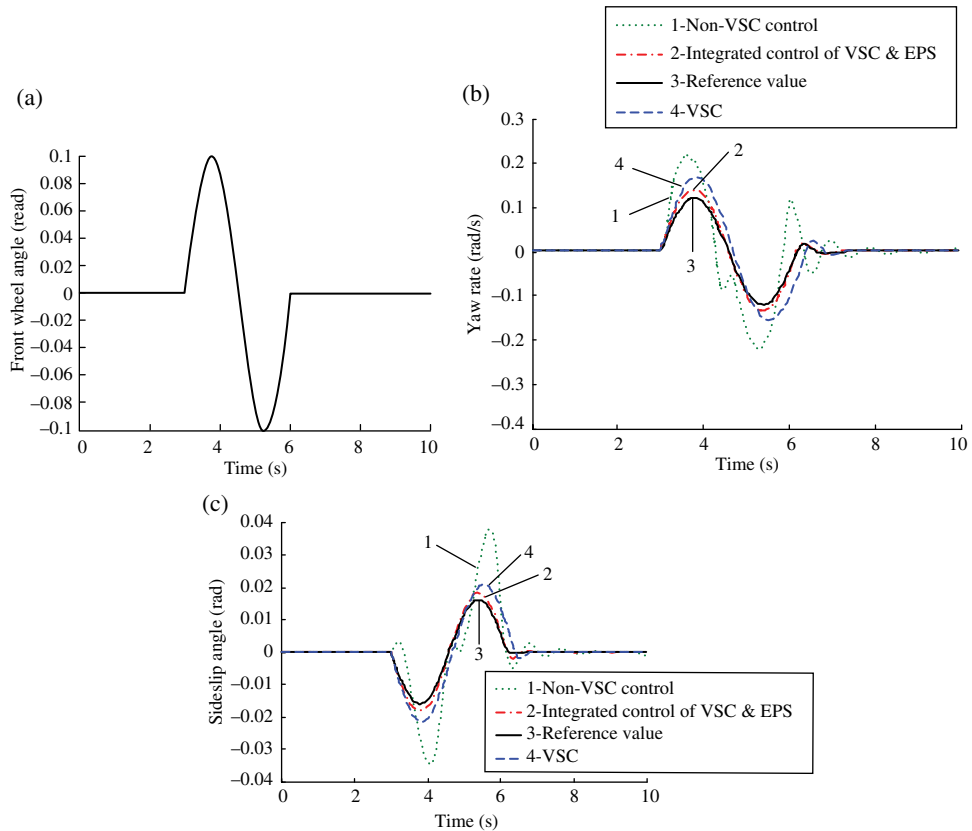

Figure 7.63 Comparison of responses for the maneuver of a single lane change. (a) Single lane change steering input to the front wheel. (b) Yaw rate. (c) Sideslip angle.
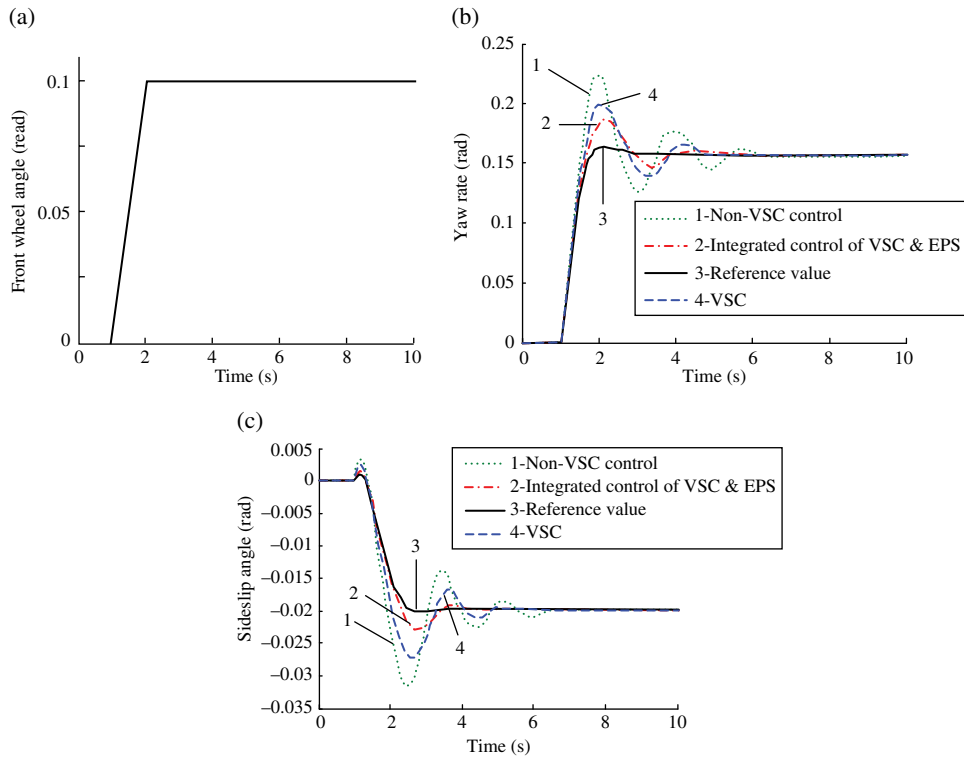
Figure 7.64 Comparison of responses for the maneuver of a step steering input. (a) Step steering input to the front wheel. (b) Yaw rate. (c) Sideslip angle.

sideslip angle. In addition, the application of the compensation strategy of the self-aligning torque is able to track the reference value faster and, hence, the settling time is shorter compared with the VSC control. Therefore, vehicle handling stability is improved by the integrated control of VSC and EPS.

7.9 Centralized Control of Integrated Chassis Control Systems using the Artificial Neural Networks (ANN) Inverse System Method

In recent years, intelligent control methods have been applied widely to the centralized control of multivariable systems to deal with nondeterministic and complex control problems. This study takes advantage of both the neural network and the centralized linearization of the inverse system. As a result, the neural network inverse system method is applied to the integrated control of vehicle Active Front Steering (AFS), Direct Yaw moment Control (DYC), and Active Suspension System (ASS)[26,39].

Figure 7.65   Vehicle dynamic model.

7.9.1   Vehicle Dynamic Model

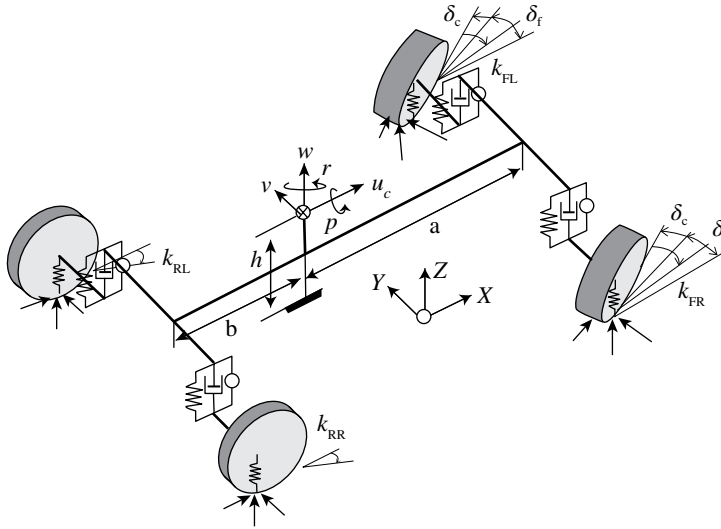As described above in Section 7.3, the nonlinear centralized method was applied to the integrated control of VSC and ASS. The overall vehicle performance, including handling stability and comfort, was improved by regulating the vertical load distribution and adjusting the brake forces. In this section, the AFS system is designed to serve as a steering correction system by applying an additional steer angle to the driver's steering input in the linear handling region. In this way, the AFS system is able to improve steerability by assisting the driver in handling the vehicle and preventing extreme handling situations. In this study, the integrated control VSC and ASS system is integrated further with the AFS system, and the neural network inverse system method is used to design the integrated centralized control of the AFS, DYC and ASS. As shown in Figure 7.65, the 7-DOF vehicle dynamic model is used, and the lateral, yaw, and roll motions are considered. In Figure 7.65, u_c, β, r, and ϕ are the vehicle longitudinal speed, sideslip angle, yaw rate, and roll angle, respectively; m, m_s, m_f, and m_r are the vehicle mass, sprung mass, unsprung mass of the front axle, unsprung mass of the rear axle, respectively; a and b are the distances between the center of gravity of the vehicle to the front and rear axles, respectively; I_z, I_x, I_{xz} are the yaw moment of inertia, roll moment of inertia, and product of inertia of the sprung mass about the roll and yaw axes, respectively ; $k_F \left(= K_{FL} + K_{FR} \right)$ and $k_R \left(= K_{RL} + K_{RR} \right)$ are the lateral stiffnesses of the front and rear tyres, respectively; δ_F, δ_c, T_z, and T_ϕ are the steering angle of the front wheel provided by the driver, additional steering angle to the front wheel provided by the AFS, corrective yaw moment, and suspension roll moment; K_ϕ and D_ϕ are the roll stiffness coefficient and damping coefficient of the suspension.

The state variable is defined as $x = \begin{pmatrix} \beta & r & \phi & \dot{\phi} \end{pmatrix}^{\mathrm{T}}$, and the control input variable $u = \begin{pmatrix} \delta_c & T_z & T_\phi \end{pmatrix}^{\mathrm{T}}$, the system output variable $y = \begin{pmatrix} \beta & r & \phi \end{pmatrix}^{\mathrm{T}}$, then the state equation of the integrated system is derived as:

$$\begin{cases} M\dot{x} = Kx + Nu + Q\delta_{\mathrm{F}} \\ y = Cx \end{cases} \tag{7.106}$$

where,

$$M = \begin{pmatrix} mu_c & am_f - bm_r & 0 & m_s h \\ (am_f - bm_r)u_c & I_z & 0 & I_{xz} \\ 0 & 0 & 1 & 0 \\ m_s h u_c & I_{xz} & 0 & I_x \end{pmatrix}$$

$$K = \begin{pmatrix} -2(k_{\mathrm{F}} + k_{\mathrm{R}}) & -mu_c + \dfrac{2(bk_{\mathrm{R}} - ak_{\mathrm{F}})}{u_c} & 0 & 0 \\ 2(bk_{\mathrm{R}} - ak_{\mathrm{F}}) & (bm_r - am_f)u_c - 2\dfrac{a^2 k_{\mathrm{F}} + b^2 k_{\mathrm{R}}}{u_c} & 0 & 0 \\ 0 & 0 & 0 & 1 \\ 0 & m_s h u_c & m_s gh - K_\phi & -D_\phi \end{pmatrix}$$

$$N = \begin{pmatrix} 2k_{\mathrm{F}} & 0 & 0 \\ 2k_{\mathrm{F}} & 1 & 0 \\ 0 & 0 & 0 \\ 0 & 0 & 1 \end{pmatrix}, Q = \begin{pmatrix} 2k_{\mathrm{F}} \\ 2ak_{\mathrm{F}} \\ 0 \\ 0 \end{pmatrix}, C = \begin{pmatrix} 1 & 0 & 0 & 0 \\ 0 & 1 & 0 & 0 \\ 0 & 0 & 1 & 0 \end{pmatrix}$$

It is obvious that equation (7.106) is a typical multivariable system with three inputs and three outputs. Due to the interactions among the tyre's longitudinal, lateral, and vertical forces, as well as the conflicts among the vehicle translational and rotational motions, the integrated control system of AFS, DYC, and ASS systems is highly coupled. Therefore, it is required to decouple the vehicle multivariable system into three independent SISO control systems in order to design the controller of the integrated system.

7.9.2 Design of the Centralized Control System

7.9.2.1 Analysis of System Invertibility

As described in Section 7.3.6, the Interactor algorithm is used to calculate the relative degree of the integrated control system given in equation (7.106). The detailed calculation of the relative degree is demonstrated as follows.

$$\dot{y}_1 = \dot{\beta} = -2(k_{\mathrm{F}} + k_{\mathrm{R}})\beta / mu_c + 2r(bk_{\mathrm{R}} - ak_{\mathrm{F}}) / mu_c^2$$
$$- m_s h \ddot{\phi} / mu_c - (am_f - bm_r)\dot{r} / mu_c - r + 2k_{\mathrm{F}}(\delta_{\mathrm{F}} + \delta_c) / mu_c \tag{7.107}$$

Let $Y_1 = \dot{y}_1$, the rank of the corresponding Jacobian matrix with respect to input $\boldsymbol{u}$ is:

$$t_1 = rank\left[\frac{\partial Y_1}{\partial u^{\mathrm{T}}}\right] = rank\left[\frac{\partial \dot{y}_1}{\partial \delta_{\mathrm{c}}} \quad \frac{\partial \dot{y}_1}{\partial T_z} \quad \frac{\partial \dot{y}_1}{\partial T_\phi}\right] = 1 \tag{7.108}$$

$$\begin{aligned}
\dot{y}_2 &= \dot{r} = 2\left(bk_{\mathrm{R}} - ak_{\mathrm{F}}\right)\beta/I_z - 2\left(a^2 k_{\mathrm{F}} + b^2 k_{\mathrm{R}}\right)r/I_z u_{\mathrm{c}} \\
&\quad -I_{xz}\ddot{\phi}/I_z - \left(am_{\mathrm{f}} - bm_{\mathrm{r}}\right)\left(\dot{\beta} + r\right)u_{\mathrm{c}}/I_z + T_z/I_z + 2ak_{\mathrm{F}}\left(\delta_{\mathrm{F}} + \delta_{\mathrm{c}}\right)/I_z
\end{aligned} \tag{7.109}$$

Let $Y_2 = \begin{bmatrix} \dot{y}_1 & \dot{y}_2 \end{bmatrix}^{\mathrm{T}}$, the rank of the corresponding Jacobian matrix with respect to $\boldsymbol{u}$ is:

$$t_2 = rank\left[\frac{\partial Y_2}{\partial u^{\mathrm{T}}}\right] = rank\begin{bmatrix} \dfrac{\partial \dot{y}_1}{\partial \delta_{\mathrm{c}}} & \dfrac{\partial \dot{y}_1}{\partial T_z} & \dfrac{\partial \dot{y}_1}{\partial T_\phi} \\[2ex] \dfrac{\partial \dot{y}_2}{\partial \delta_{\mathrm{c}}} & \dfrac{\partial \dot{y}_2}{\partial T_z} & \dfrac{\partial \dot{y}_2}{\partial T_\phi} \end{bmatrix} = 2 \tag{7.110}$$

$$\begin{aligned}
\dot{y}_3 &= \dot{\phi} \\
\ddot{y}_3 &= \ddot{\phi} = -D_\phi \dot{\phi}/I_x - \left(K_\phi - m_{\mathrm{s}}gh\right)\phi/I_x - I_{xz}\dot{r}/I_x - m_{\mathrm{s}}h\left(\dot{\beta} + r\right)u_{\mathrm{c}}/I_x + T_\phi/I_x
\end{aligned} \tag{7.111}$$

Let $Y_3 = \begin{bmatrix} \dot{y}_1 & \dot{y}_2 & \ddot{y}_3 \end{bmatrix}^{\mathrm{T}}$, the rank of the corresponding Jacobian matrix with respect to $\boldsymbol{u}$ is:

$$t_3 = rank\left[\frac{\partial Y_3}{\partial u^{\mathrm{T}}}\right] = rank\begin{bmatrix} \dfrac{\partial \dot{y}_1}{\partial \delta_{\mathrm{c}}} & \dfrac{\partial \dot{y}_1}{\partial T_z} & \dfrac{\partial \dot{y}_1}{\partial T_\phi} \\[2ex] \dfrac{\partial \dot{y}_2}{\partial \delta_{\mathrm{c}}} & \dfrac{\partial \dot{y}_2}{\partial T_z} & \dfrac{\partial \dot{y}_2}{\partial T_\phi} \\[2ex] \dfrac{\partial \ddot{y}_3}{\partial \delta_{\mathrm{c}}} & \dfrac{\partial \ddot{y}_3}{\partial T_z} & \dfrac{\partial \ddot{y}_3}{\partial T_\phi} \end{bmatrix} = 3 \tag{7.112}$$

Therefore the relative degree of the system is $\boldsymbol{r} = \begin{bmatrix} r_1 & r_2 & r_3 \end{bmatrix}^{\mathrm{T}} = \begin{bmatrix} 1 & 1 & 2 \end{bmatrix}^{\mathrm{T}}$, and $\sum_{i=1}^{3} r_i = n = 4$ (n is the system order). According to the implicit function theorem, it is known that the inverse system of the original integrated control system exists, and the output of the inverse system $\boldsymbol{u}$ (i.e., the input of the original system) is given as:

$$\boldsymbol{u} = \varphi\left(\boldsymbol{x}, \dot{y}_1, \dot{y}_2, \ddot{y}_3\right) = \varphi\left(\boldsymbol{x}, \boldsymbol{v}\right) \tag{7.113}$$

where $\boldsymbol{v} = \begin{bmatrix} v_1 & v_2 & v_3 \end{bmatrix}^{\mathrm{T}} = \begin{bmatrix} \dot{y}_1 & \dot{y}_2 & \ddot{y}_3 \end{bmatrix}^{\mathrm{T}}$, $\varphi(\cdot)$ is the nonlinear relationship between the input and output of the inverse system. Let $z_1 = y_1$, $z_2 = y_2$, $z_{31} = y_3$, $z_{32} = \dot{z}_{31} = \dot{y}_3$, $v_1 = \dot{y}_1$,
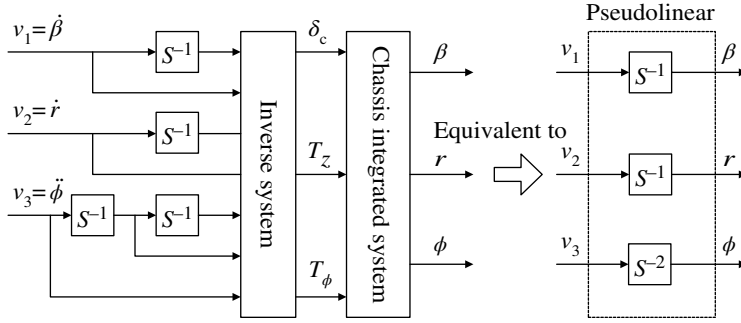
Figure 7.66   Structure of the pseudo-linear system.

$v_2 = \dot{y}_2$, $v_3 = \ddot{y}_3$ be the inputs to the inverse system, the standard form of the inverse system is given as:

$$\begin{cases} \dot{z}_1 = v_1 \\ \dot{z}_2 = v_2 \\ \dot{z}_{31} = z_{32} \\ \dot{z}_{32} = v_3 \\ \boldsymbol{u} = \overline{\varphi}\left(z_1 \quad z_2 \quad z_{31} \quad z_{32} \quad v_1 \quad v_2 \quad v_3 \right) \end{cases} \tag{7.114}$$

As shown in equation (7.114), a pseudolinear system is constructed by connecting the inverse system ahead of the original one in series, which is equivalent to two first-order integral linear subsystems and one second-order integral linear subsystem. The structure of the pseudo-linear system is illustrated in Figure 7.66.

7.9.2.2   Design of a Neural Network Inverse System

The analytical expression of the inverse system given in equation (7.114) is based on the accurate mathematical model. Therefore, the centralized characteristics of the pseudolinear system are realized only if the original system parameters are known, accurate, and time-invariant. To improve the self-adaptability to the parameter variations and the robustness with respect to external disturbances, the static neural network and the integrator is applied to construct the inverse system[25].

It is known from equation (7.114) that the input layer includes β, r, ϕ, $\dot{\phi}$, $\dot{\beta}$, $\dot{r}$, and $\ddot{\phi}$; and the output layer includes δ_c, T_z, and T_ϕ. Therefore, the number of neurons on the input layer is set to be seven, and three for the output layer. The number of neurons on the implicit layer is determined to be 15 by the trial-and-error method. The nonlinear mapping of the inverse system is approached by using the static neural network. Four integrators are used to represent the dynamic characteristics of the inverse system. The structure of the developed neural network inverse system is 7-15-3, which is shown in Figure 7.67.
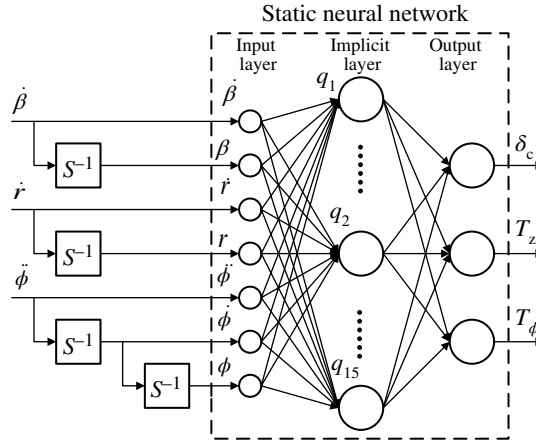
Figure 7.67   Structure of the BP neural network inverse system.

In the structure, the function *tansig* is used as the transfer function for the input layer and the implicit layer of the BP network, and the function *purelin* for the output layer.

It is assumed that the vehicle travels at a speed of 100 km/h, and the driver's steering input to the front wheels is a sinusoidal curve with a varying amplitude. As shown in Figure 7.68, the stimulating input signals used to train the neural network include the additional angle to the front wheel δ_c, corrective yaw moment T_z, and roll moment of the suspension T_ϕ. The dynamic responses of the yaw rate r, sideslip angle β, and roll angle ϕ are sampled with a period of 5 ms. Then $\dot{r}$, $\dot{\beta}$, $\dot{\phi}$ and $\ddot{\phi}$ are calculated according to the five-point numerical differential method. Two hundred sets of training data sets $[\beta, \dot{\beta}, r, \dot{r}, \phi, \dot{\phi}, \ddot{\phi}]$ and $[\delta_c, T_z, T_\phi]$ are obtained by combining the above-obtained data. The *premnmx* function in the neural network toolbox in MATLAB is used to normalize the network input and output data. In the network simulation test, the new data are preprocessed by the function *tramnmx* in the same way, and finally normalized by the function *postmnmx*. The BP neural network is established by the function *newff*, and the function *trainlm* of the Levenberg-Marquardt algorithm is selected as the training function. The established BP network has been trained by the selected training function for 500 times with a learning efficiency of 0.05, and a network target error of 10^{-3}. The required training accuracy is achieved after 72 sessions training in the simulation.

7.9.2.3   Design of the PD Controller

By performing the centralized process, the original integrated system is transformed into the three independent SISO systems, including the first-order AFS subsystem, the first-order DYC subsystem, and the second-order ASS subsystem. In order to improve the response quality of the integrated system, a compound controller shown in Figure 7.69 is designed by combining the PD controller and the neural network reverse system.
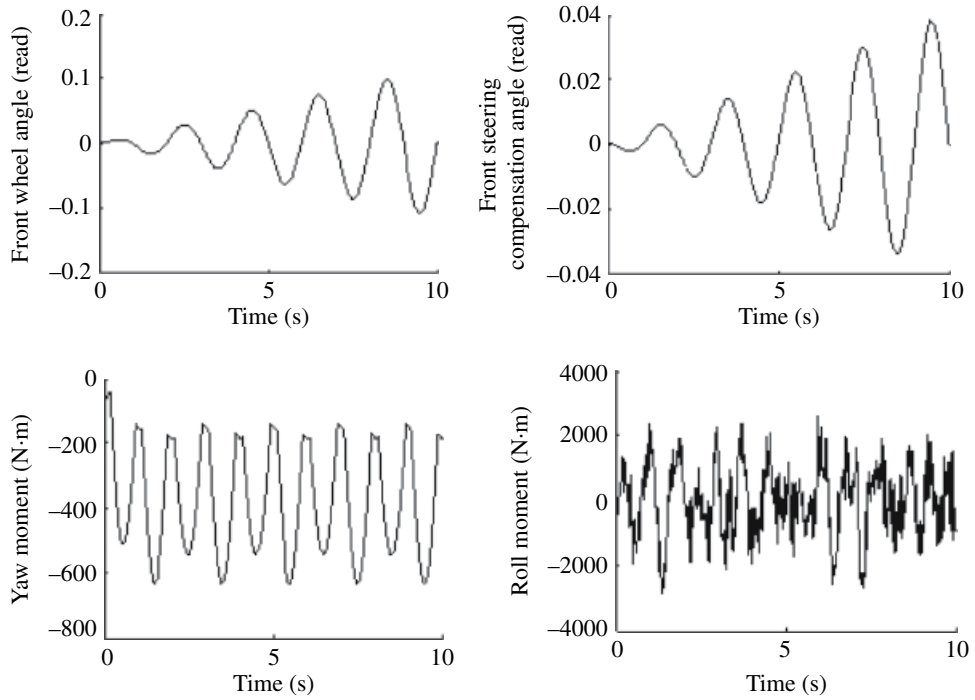
Figure 7.68   Stimulating input signals of neural network inverse system.
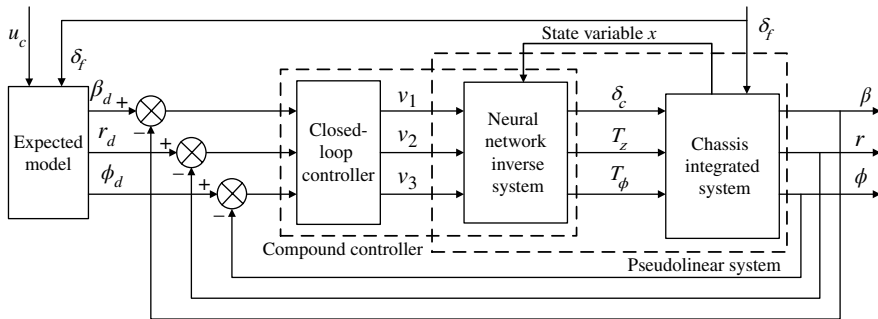

Figure 7.69   Block diagram of the centralized integrated control system.

As the input and output of the centralized pseudolinear system has a one-to-one linear relationship, a number of control methods for single variable linear systems can be applied to the design of the controller, including PID control, pole placement, and quadratic optimal. Here, the PD closed loop controller is designed as follows:

$$v = K_{\mathrm{P}}\mathrm{diag}\{e\} + K_{\mathrm{d}}\mathrm{diag}\{de\} \tag{7.115}$$

where *e* and *de* are the tracking error of the system output signals, and its difference, respectively; K_p and K_d are the proportional and differential coefficient, respectively. The vehicle reference model included in Figure 7.69, generates the expected dynamic response according to the driver's input, and the expected sideslip angle and yaw rate are obtained as:

$$
\begin{cases}
\beta_d = \dfrac{\dfrac{2k_F\left(2a^2k_F + 2b^2k_R\right)}{2ak_F - 2bk_R + mu_c^2} - 2bk_F}{\dfrac{\left(2k_F + 2k_R\right)\left(2a^2k_F + 2b^2k_R\right)}{2ak_F - 2bk_R + mu_c^2} + 2bk_R - 2ak_F} \delta_f \\[4mm]
r_d = \min\left\{ \left\| \dfrac{u_c\delta_F}{(a+b)(1+Ku_c^2)} \right\|, \left| \dfrac{\mu g}{u_c} \right| \mathrm{sgn}\left(\delta_f\right) \right\}
\end{cases}
\qquad (7.116)
$$

where μ is the road adhesion coefficient, and K is the understeer coefficient.

7.9.3   Simulation Investigation

To demonstrate the effectiveness of the developed integrated control system, a simulation investigation is performed by comparing the developed integrated control system with the integrated control system with PD control, and the system with the decentralized control (i.e., the three stand-alone controllers of AFS, ASS and DYC). The vehicle initial speed is set as $u_c = 80\,\mathrm{km/h}$, the road adhesion coefficient of $\mu = 0.85$ is selected. Two driving conditions are performed, including single lane change and step steering input. The vehicle physical parameters in Table 7.5 are used. After tuning, the PD coefficients of the closed loop controller are set as $K_p = \mathrm{diag}\{18\,52\,5000\}$ and $K_d = \mathrm{diag}\{4.5\,3\,10\}$. The roll stiffness coefficient of the suspension is $K_\phi = 65590\,\mathrm{N \cdot m/rad}$, and the suspension roll damping coefficient is $D_\phi = 2100\,\mathrm{N \cdot m \cdot s/rad}$.

(1)   Single lane change maneuver
The simulation is performed according to the GB/T6323.1-94 controllability and stability test procedure for automobiles – pylon course slalom test. For the maneuver of a single lane change, the amplitude of the front wheel steering angle is set as 0.08 rad and the frequency as 0.5 Hz. It is illustrated clearly in Figure 7.70 and Table 7.12 that the peak value of the yaw rate for the developed integrated control is reduced greatly by 12% and 29% respectively, compared with the integrated control system with PD control, and the system with the decentralized control. A similar pattern can be observed for the sideslip angle and roll angle. The results indicate that the application of the centralized PD control is able to track effectively the expected vehicle states and hence improve its handling stability.

(2)   Step steering input manoeuvre
The simulation is conducted according to the GB/T6323.2-94 controllability and stability test procedure for automobiles – steering transient response test (steering wheel angle
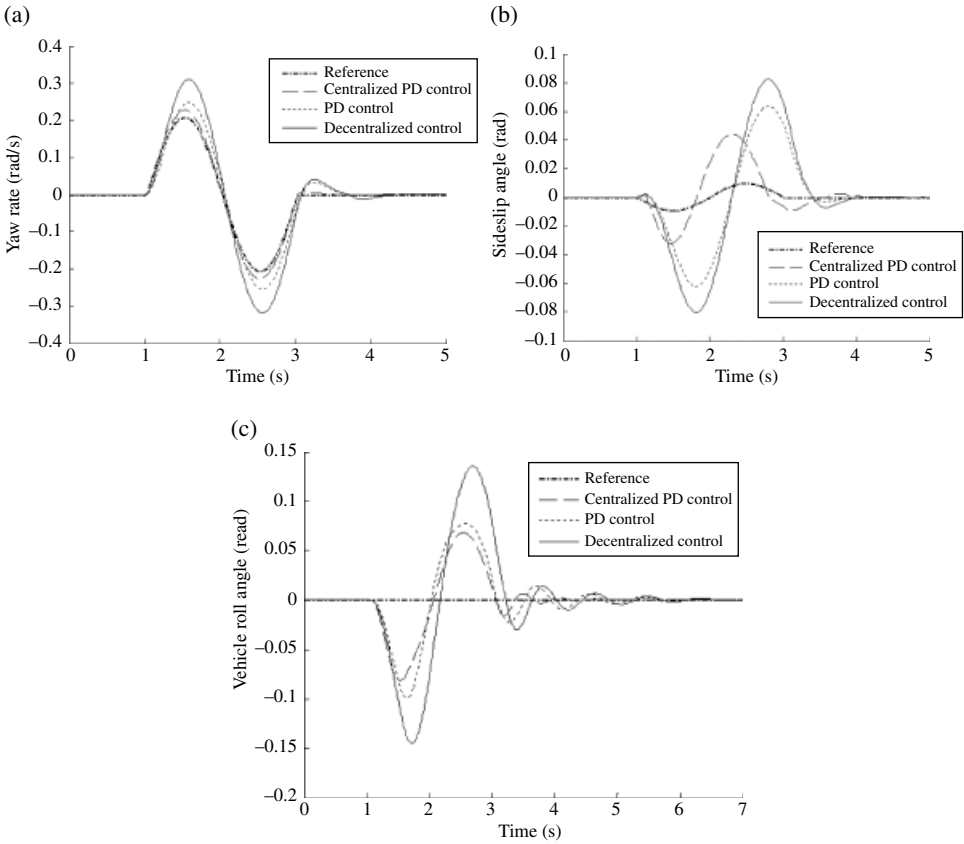
(a)

(b)

(c)

Figure 7.70 Comparison of responses for the single lane change maneuver. (a) Yaw rate. (b) Sideslip angle. (c) Roll angle.

Table 7.12 Comparison of the peak value of the single line change simulation results.

Control Method	Yaw rate r/rad. s^{-1}	Sideslip angle β/rad	Roll angle ϕ/rad
Expectation	0.2	0.01	0
Centralized PD control	0.22	0.041	0.075
PD control	0.25	0.062	0.096
Decentralized control	0.31	0.081	0.147

step input). The step steering input to the wheel is set at 1.57 rad. It is illustrated clearly in Figure 7.71 and Table 7.13 that the peak value of the yaw rate for the developed integrated control is reduced significantly by 19.1% and 26.4% respectively, compared with the integrated control system with PD control, and the system with the decentralized control. A similar pattern can be observed for the sideslip angle and roll angle. The results
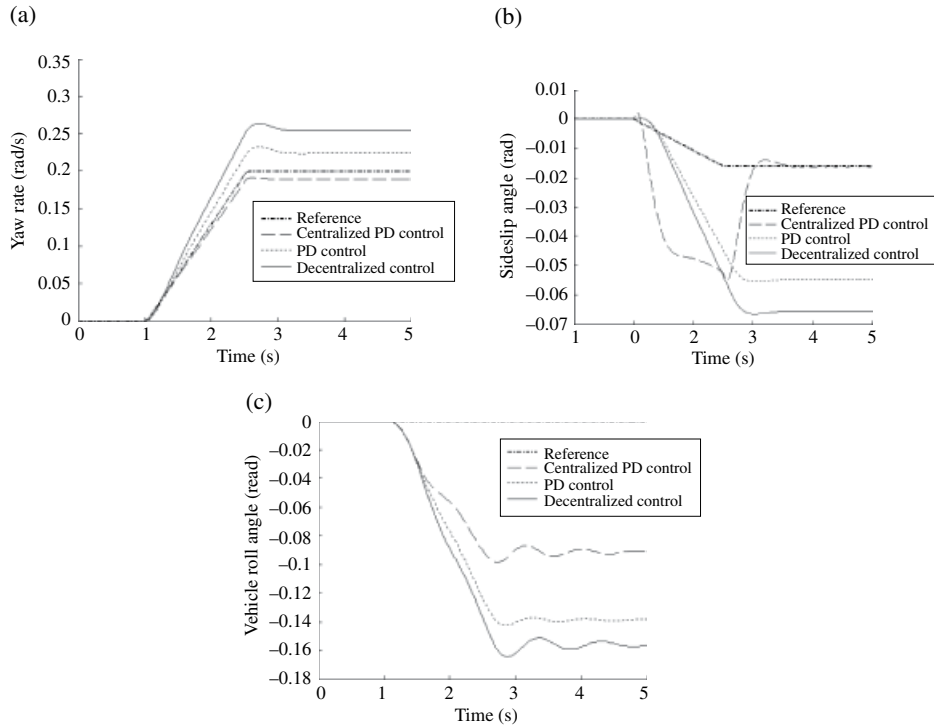
(a)

(b)

(c)

Figure 7.71 Comparison of responses for the maneuver of step steering input. (a) Yaw rate. (b) Sideslip angle. (c) Roll angle.

Table 7.13 Comparison of step steering simulation result peak values.

Control method	Yaw rate r (rad/s)	Sideslip angle β (rad)	Roll angle ϕ (rad)
Reference	0.2	0.017	0
Centralized PD Control	0.195	0.055	0.096
PD Control	0.241	0.056	0.142
Decentralized Control	0.265	0.066	0.164

indicate that the application of the centralized PD control is able to track effectively the expected vehicle states and hence improve the vehicle handling stability. In addition, the amplitudes of these performance indices for the combined control system are relatively larger since the conflicts among the three subsystems are unable to coordinate. Finally, these three performance indices for the integrated control system with PD control are deviated from the expected states since the PD controller fails to deal with the coupling effects of the control loop and, hence, it is inevitable that they negatively influence each other.

References

[1] Fruechte R D, Karmel A M, Rillings J H, Schilke N A., Boustany N M, Repa B S. Integrated vehicle control. Proceedings of the 39th IEEE Vehicular Technology Conference, May 1–3, 1989, San Francisco, CA, Vol. 2, 868–877.

[2] Gordon T J, Howell M, Brandao F. Integrated control methodologies for road vehicles. Vehicle System Dynamics, 2003, 40(1–3), 157–190.

[3] Yu F, Li D F, Crolla D A. Integrated vehicle dynamic control – State-of-the art review. Proceedings of IEEE Vehicle Power and Propulsion Conference (VPPC), September 3–5, 2008, Harbin, China, 1–6.

[4] Falcone P, Borrelli F, Asgari J, Tseng H E, Hrovat D. Predictive active steering control for autonomous vehicle systems. IEEE Transactions on Control Systems Technology, 2007, 15(3), 566–580.

[5] Chen W W, Xiao H S, Liu L Q, Zu J W. Integrated control of automotive electrical power steering and active suspension systems based on random sub-optimal control. International Journal of Vehicle Design, 2006, 42(3/4), 370–391.

[6] Hirano Y, Harada H, Ono E, Takanami K. Development of an Integrated System of 4WS and 4WD by H Infinity Control. SAE Technical Paper 930267, 1993, 79–86.

[7] Li D F, Du S Q, Yu F. Integrated vehicle chassis control based on direct yaw moment, active steering, and active stabiliser. Vehicle System Dynamics, 2008, 46(1), 341–351.

[8] Nwagboso C O, Ouyang X, Morgan C. Development of neural network control of steer-by-wire system for intelligent vehicles. International Journal of Heavy Vehicle Systems, 2002, 9(1), 1–26.

[9] Trächtler A. Integrated vehicle dynamics control using active brake, steering, and suspension systems. International Journal of Vehicle Design, 2004, 36(1), 1–12.

[10] Gordon T J. An integrated strategy for the control of a full vehicle active suspension system. Vehicle System Dynamics, 1996, 25, 229–242.

[11] Rodic A D, Vukobratovie M K. Design of an integrated active control system for road vehicles operating with automated highway systems. International Journal Computer Application Technology, 2000, 13, 78–92.

[12] Karbalaei R, Ghaffari A, Kazemi R, Tabatabaei S H. A new intelligent strategy to integrated control of AFS/DYC based on fuzzy logic. International Journal of Mathematical, Physical and Engineering Sciences, 2007, 1(1), 47–52.

[13] Chang S, Gordon T J. Model-based predictive control of vehicle dynamics. International Journal of Vehicle Autonomous Systems, 2007, 5(1–2), 3–27.

[14] Koehn P, Eckrich M, Smakman H, Schaffert A. Integrated Chassis Management: Introduction into BMW's Approach to ICM. SAE Technical Paper 2006-01-1219, 2006.

[15] Liu X Y. Research on direct yaw moment control for vehicle stablity control. Ph.D. Thesis, Hefei University of Technology, Hefei, China, 2010.

[16] Chen W W, Liu X Y, et al. Dynamic boundary control of sideslip angle for vehicle stablity control through considering the effects of road surface friction. Journal of Mechanical Engineering, 2012, 48(14), 112–118 (in Chinese).

[17] van der Steen R. Tyre/road Friction Modeling. Literature Survey, Department of Mechanical Engineering, Eindhoven University of Technology, 2007.

[18] Rabhi A, Amiens C R E A, et al. Estimation of contact forces and wheel road friction. Proceedings of the 15th Mediterranean Conference on Control and Automation, Athens, June 27–29, 2007, 1–6.

[19] Grip H, Imsland L, Johansen T A, et al. Nonlinear vehicle velocity observer with road-wheel friction adaptation. Proceedings of the 45th IEEE Conference on Decision and Control, San Diego, USA, December, 2007, 1080–1085.

[20] Yu F, Lin Y. Vehicle System Dynamics. China Machine Press, Beijing, 2008 (in Chinese).

[21] Zhao J, Lin H. Simulation of target attribute recognition based on BP neural network model. Journal of System Simulation, 2007, 19(11), 2571–2573 (in Chinese).

[22] Li M Y, Du Y L. Composite neural networks adaptive control of temperature based on genetic algorithm learning. Control Theory & Applications, 2004, 21(2), 242–246 (in Chinese).

[23] Dai W Z, Lou H C, Yang A P. An overview of neural network predictive control for nonlinear systems. Control Theory & Applications, 2009, 26(5), 521–528 (in Chinese).

[24] Zhou H Y, Zhang J, You L K, et al. Nonlinear predictive function control based on hybrid neural network. Control Theory & Applications, 2005, 22(1), 110–113 (in Chinese).

[25] Wang B W, Shen Y J, He T Z. Multi-layer feedforward neural network based on multi-output neural model and its applications. Control Theory & Applications, 2004, 21(4), 611–613 (in Chinese).

[26] Zhu M F. Research on centralized control for integrated chassis control system and time delay control for chassis key subsystems. Ph.D. Thesis, Hefei University of Technology, Hefei, China, 2011.

[27] Dai X Z. The Inverse Neural Network Control Method for Multivariable Nonlinear Systems. Beijing: Science Press, 2005 (in Chinese).

[28] Chen W W, Sun Q Q, et al. Integrated control of steering and suspension systems based on disturbance suppression. Journal of Mechanical Engineering, 2007, 43(11), 98–104 (in Chinese).

[29] Wang Q D, Wu B F, Chen W W. Integrated control of active suspension and electrical power steering based on predictive control. Transactions of the Chinese Society for Agricultural Machinery, 2007, 38(1), 1–5 (in Chinese).

[30] Zhu J. Intelligent Predictive Control and its Applications. Hangzhou: Zhejiang University Press, 2002 (in Chinese).

[31] Sun P Y, Chen H, Kang J, Guo K H, et al. Constrained predictive control of vehicle active suspension. Journal of Jilin University, 2002, 20(2), 47–52 (in Chinese).

[32] Chen W W, Wang Y W, Wang Q D. Integrated control of electrical power steering and active suspension using multivariable adaptive control. Journal of Vibration Engineering, 2005, 18(3), 360–365 (in Chinese).

[33] Chen W W, Xiao H S, Liu L Q, Zu J W. Integrated control of automotive electrical power steering and active suspension systems based on random sub-optimal control. International Journal of Vehicle Design, 2006, 42(3/4), 370–391.

[34] Cai T Y. Multivariable Adaptive Centralized Control and its Applications. Beijing: Science Press, 2001 (in Chinese).

[35] Chen W W, Xu J, Hu F. Input-output centralized and centralized PD control of vehicle nonlinear systems. Chinese Journal of Mechanical Engineering, 2007, 43(2), 64–70 (in Chinese).

[36] Xia X H, Gao W B. Nonlinear System Control and Decouple. Beijing: Science Press, 1993 (in Chinese).

[37] Yu F, Corolla D A. An optimal self-tuning controller for an active suspension. Vehicle System Dynamics, 1998, 29, 51–65.

[38] Liu Y, Fang M, Wang H B. Research on calculation and distribution of composition of forces for vehicle stability control. Proceedings of the 31st Chinese Control Conference, July 25–27, 2012, Hefei, China, 4652–4657 (in Chinese).

[39] Zhu M F, Chen W W, Xia G. Vehicle chassis centralized control based on neural network inverse method. Transactions of the Chinese Society for Agricultural Machinery, 2011, 42(12), 13–17 (in Chinese).